Exploring the Boundary Condition of Polymeric Liquids

– Experiments and MD Simulations –

Dissertation

zur Erlangung des Grades
des Doktors der Naturwissenschaften
der Naturwissenschaftlich-Technischen Fakultät
der Universität des Saarlandes

von

Mischa Klos

Saarbrücken

2016

Tag des Kolloquiums:	15.12.2016
Dekan:	Univ.-Prof. Dr. Guido Kickelbick
Mitglieder des Prüfungsausschusses:	Univ.-Prof. Dr. rer. nat. Ludger Santen
	Univ.-Prof. Dr. rer. nat. Karin Jacobs
	Univ.-Prof. Dr. rer. nat. Martin Müser
	Dr. Jean-Baptiste Fleury

Abstract

In the classic case of a liquid running trough a pipe, the flow velocity is usually the fastest in the center and decreases towards the walls. In this macroscopic picture, the very last 'fluid layer' at the solid/liquid interface is at rest. On small scales, the importance of this interface grows, since the ratio between surface and volume increases. In fact, on a micro-scale and under certain conditions, a liquid can reach a velocity at the interface. This phenomenon is known as 'slippage'. Understanding slippage is a key to control the flow of fluids in micro-devices. The present thesis studies slippage of thin polymer films on two differently ordered types of self-assembled silane monolayers (SAM), as well as on an amorphous PTFE surface. Based on existing work on polystyrene [Gut2013, Bäu2012a], the influence of the liquid's and substrate's structure on slippage is examined in dewetting experiments of polymers with various side groups (PVP, PMMA, PS). It turns out that PS on a SAM of relatively low degree of order shows a significantly higher slip length than any other combination of polymer and surface tested in the context of this thesis. The specific kind of order plays a major role. Insights on the structure are gained with the help of X-ray reflectometry and molecular dynamic simulations. MD simulations were able to mimic experimentally observed structural and dynamical data.

Kurzzusammenfassung

Klassisch betrachtet fließt eine Flüssigkeit in einem Rohr in der Mitte am schnellsten und zum Rand hin langsamer. Die Flüssigkeitslage direkt an der Fest/flüssig-Grenzfläche ist makroskopisch gesehen in Ruhe. Auf kleinen Skalen nimmt die Bedeutung dieser Grenzfläche zu, da das Oberfläche-zu-Volumen-Verhältnis steigt. Unter bestimmten Umständen kann eine Flüssigkeit eine mikroskopische Geschwindigkeit an der Grenzfläche besitzen. Dieses Phänomen nennt man 'slippage' (Rutschen). Um den Fluss in Mikro-Bauelementen zu kontrollieren, ist es wichtig dieses Rutschen zu verstehen. Die vorliegende Arbeit beschäftigt sich mit dem Rutschverhalten von dünnen Polymerfilmen auf zwei verschieden geordneten Silanmonolagen (SAM), sowie einer armophen PTFE Oberfläche. Ausgehend von früheren Arbeiten zu Polystyrol [Gut2013, Bäu2012a] wird der Einfluss des Aufbaus von Substrat und Flüssigkeit auf das Rutschen, anhand von Entnetzungsexperimenten mit Polymeren die unterschiedliche Seitengruppen aufweisen (PVP, PMMA, PS), untersucht. Es zeigt sich, dass PS auf SAMs relativ geringer Ordnung sehr viel besser rutscht, als irgendeine andere der untersuchten Substrat-Polymer-Kombinationen. Dabei spielt die Art der Ordnung eine wichtige Rolle. Mit Hilfe von Röntgenreflektometrie und Molekulardynamik-Simulationen konnten Einblicke in die Struktur gewonnen werden. Dabei war es möglich die experimentell beobachteten strukturellen und dynamischen Eigenschaften in MD-Simulationen nachzuahmen.

Contents

List of Figures

List of Tables

1 Introduction

Common images of flowing liquids are usually associated with water or oil, but the imagination of a flowing plastic is unusual. Yet, molten plastics are an important aspect in industry. Every piece of plastic was once liquid before it gets its final shape. Also, coatings are applied when liquid. Despite being often nanometer thin, they should cover the substrate completely. So understanding the flow and wetting conditions of polymeric substances in their liquid state is crucial. Especially when it comes to small scales, where macroscopic laws are not able to describe the processes precisely, with respect to a dramatic increase of the surface to volume ratio.

A polymer melt is a complex matter consisting of long molecules, that are able to entangle, coil, arrange or to order. Even for the single components, a polymer is build of, arrangements along the chain are possible. Therefore the flow of a polymer melt depends heavily on the physical properties of the individual chains. This is quite obvious for the length: longer molecules take more room, are more likely to entangle, and therefore shear properties are not as simple as for instance in case of water. However, the influence of some other characteristics, like the design of the individual monomer, especially its side group(s), on the flow conditions is not that obvious. Also the effect of possible structure formation along the chain, is not per se predictable.

Moreover, conformations of the bulk liquid can heavily differ from those at the interface towards other materials. Especially on small scales, like in thin films, interface and confinement effects can be very dominant. This work deals with the flow conditions of thin polymer films with thicknesses of about 100 nm. In contact with certain nano-structured hydrophobic surfaces, some polymers can reach a finite flow velocity right at the interface, which is not covered through classic hydrodynamics. The phenomenon of a liquid's velocity that is not zero at the boundaries is known as slippage. Although, the concept of slippage was already introduced by Navier in the early 19th century and has been long studied in science, it is not fully understood.

Thin liquid polystyrene films on top of a self-assembled monolayer (SAM) of silanes can exhibit readings of slippage, that imply an almost constant flow profile all the way towards the interface. If the film consists of polystyrene molecules long enough to be able to entangle, this can be explained by a reduction of entanglements at the interface [Bäu2009a].

There is no appropriate molecular image available that describes slippage in the case of non-entangled polystyrene prepared on a structured surface, like a silane SAM.

The present work is dedicated to test if the structure of a polymer influences the slip boundary condition and if this structure aligns depending on the underlying substrate. What could be the molecular mechanism, and which conditions enable pronounced slippage? This thesis compares known results for slippage of polystyrene on silanes and on amorphous PTFE AF (Teflon®) to two other polymers that feature different molecular structures. Besides determining the strength of slippage, conformations at the solid/liquid interface are studied with the help of scattering techniques and MD simulations.

The following Chapter 2 starts with a brief introduction into the basic principles of flow on small scales and the concept of slip and how it can be measured. The chapter also presents important and latest scientific achievements that are crucial in the context of this thesis.

To study the influence of the substrate on the polymer, a detailed knowledge of the polymer's and the substrate's composition is essential. Chapter 4 introduces the used materials, like polymers, coatings and substrates and their basic properties.

A detailed analysis of the surface characteristics and the structural composition of the prepared silane SAMs and PTFE AF coatings is given in Chapter 5. The molecular picture of the SAMs is experimentally analyzed by AFM and scattering methods, and completed by MD simulations. The techniques and the equipment used during this work is introduced before, in Chapter 3.

A first series of slippage experiments is presented in Chapter 6. This study focuses on different slip boundary conditions arising from the substrate of the SAM: the slippage of polystyrene on silanes SAMs grown on silicon wafers as compared to quartz wafers.

Recently, as a result of their scattering experiments, Gutfreund et al. [Gut2013] suggested that the side groups of polystyrene arrange differently at the interface, depending on the structure of the SAM they are prepared on. Chapter 7 presents the comparison of three different polymers with different side group compositions – polystyrene (PS), poly(2-vinyl) pyridine (PVP), and poly(methyl) metacrylate (PMMA) – with regard to their flow behavior on silane SAMs and PTFE AF.

Chapter 8 gives an introduction into an ongoing project on all-atom MD simulations of polystyrene on silane SAMs. Results concerning structure and arrangement of the molecules inside the substrate and the polymer film are given, together with a basic analysis of the polymer's mobility.

Usually experiments were performed with polymers whose side groups are randomly distributed along the chain (atactic). Chapter 9 shows first data of a special kind of polystyrene, whose side groups point exclusively to one direction (isotactic).

Chapter 10 summarizes and links the results, before finally an outlook is given on what will and could be done in future work.

2 Context & State of the Art

This chapter gives a brief overview of the state of the art in literature and the physical context of the present thesis. The introduction into the basic principles of the motion of liquids follows the description in the textbook of Landau and Lifschitz [Lan1991]. The physics of thin films, their wetting properties and the models developed in the last years to describe and to measure their slip boundary condition are abstracted from the review of Bäumchen et al. [Bäu2010c].

2.1 Flow in Confined Systems

A thin polymer film with height h represents a complex liquid in a confined system. Thus the flow conditions are not comparable to the bulk situation. Nevertheless, the basic principle of mass conservation during flow is granted. Together with the assumption of an incompressible liquid whose density ρ is constant with time and space, and the conservation of momentum, the **Navier-Stokes equation** can be devised:

$$\rho(\partial_t + \vec{u} \cdot \nabla)\vec{u} = -\nabla p + \eta \Delta \vec{u} + \vec{f}. \tag{2.1}$$

It describes the flow of both, a simple and a complex liquid with viscosity η and velocity field $\vec{u} = (u_x, u_y, u_z)$. The pressure gradient ∇p and the volume force $\vec{f}$ of external fields drive the liquid's flow process. For small Reynolds numbers

$$Re = \frac{\rho u h}{\eta} \ll 1, \tag{2.2}$$

the left part of Equation 2.1 can be neglected as compared to the right part, simplifying the equation to the **Stokes equation**

$$0 = -\nabla p + \eta \Delta \vec{u} + \vec{f}. \tag{2.3}$$

In the situation of a thin film, variations of the film height h are much smaller than the film height itself, considered on the lateral scale (see Fig. 2.1). Along with the assumption that the liquid's velocity perpendicular to the substrate is smaller than in lateral direction, it is possible to develop a thin film approximation based on the Navier-Stokes equation [Oro1997]. In this sense, a film is considered as 'thin', as long as its height is smaller than the capillary length l_c, that is typically in the order of 1 mm. With the help of the thin film approximation it is possible to describe the liquid's velocity profile in three dimensions and the mobility at the interface towards the substrate.

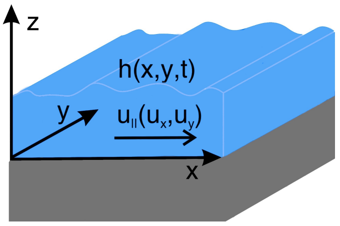

Figure 2.1: Schematic of a thin film with flow field $u_{||}$ and height h.

2.2 Slip/no-slip Boundary Condition

Conditions at the interfaces in confined systems have a crucial impact on the liquids flow behavior. These conditions depend mainly on the characteristics of the materials that build the surroundings of the film. In classic hydrodynamics, the velocity parallel to the substrate is assumed to be zero right at the interface (**no-slip** boundary condition, see Figure 2.2 far left). This is suitable to describe macroscopic processes like the flow of water through a pipe, but not for microscopic and confined systems. To cover the flow on this scale, it is often necessary to assume a velocity at the interface. This phenomenon is called **slippage**.

Figure 2.2 depicts four possible flow conditions at the interface between liquid and substrate: Firstly, the already introduced no-slip condition, where there is only viscous flow inside the liquid and no friction at the walls towards the substrate. Secondly, the situation where every liquid molecule features the same velocity, meaning that the whole liquid slips over the surface like a solid. In this full-slip case, energy is only dissipated at the interface, since there is no viscous flow but friction. It should be mentioned that at the free interface a full-slip boundary condition is ever-present. Thirdly, a superposition of both border cases leads to **partial slip**. The liquid's flow profile descends towards the wall, but reaches zero only at a virtual point inside the substrate. The extrapolation length measured from the interface down to this point is identified as the **slip length** b. In the case of partial slip, b takes finite values, whereas in the full-slip case, $b = \infty$ and for no-slip $b = 0$. In the fourth place, the effect of apparent slip has to be mentioned. It describes a scenario, where the flow profile resembles the partial slip case except for a layer next to the substrate, which has in fact a lower, or even no velocity. Measuring the 'macroscopic' flow profile leads to a slip length that does not exist at the interface, also known as 'effective slip length' [Boc2007, Cot2004, Pri2005, Lun2012]. Apparent slip can be observed for example in inhomogeneous liquids or where a shear thinning at the boundary is possible. Recent studies reported apparent slip in a system of confined polymer solutions, where a reduction of polymer chains takes place at the interface [Cue2013], similar to what happens in a polymer melt of long entangled chains at the interface to an amorphous hydrophobic substrate [Bäu2012a].

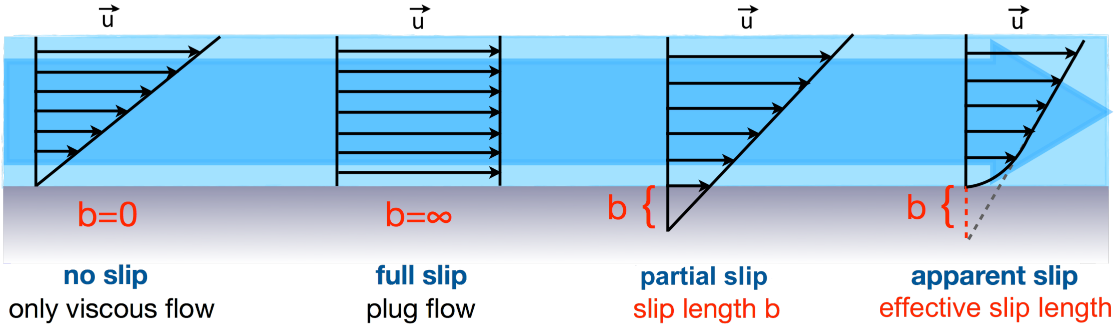

Figure 2.2: Flow profiles of a thin film flowing over a surface. From left to right: **1.** Border case no slip, the flow is fastest at the free interface and drops to zero at the solid/liquid interface (slip length $b = 0$). **2.** Border case full slip, every liquid layer has the same velocity, the liquid moves like a solid over the surface ($b = \infty$). **3.** Superposition of case 1 and 2, the liquid reaches a finite velocity at the interface. The slip length b is defined as the extrapolation length of the flow profile where the velocity drops to zero again (b = finite number). **4.** Apparent slip, the last liquid layer at the interface has no velocity, but the overall flow profile leaves the impression of a slip length, as in case 3.

Already in 1823, Navier [Nav1823] described slippage using a linear boundary condition, where the liquid's tangential velocity $u_{\|}$ is proportional to the normal component of the strain rate tensor $\dot{\gamma}$. He named the proportional constant slip length b:

$$\vec{u_{\|}} = b \cdot \vec{n} \cdot \dot{\gamma}. \tag{2.4}$$

Assuming a one-dimensional flow in x-direction (the interface expands in xy-direction), the slip length can be written as the ratio between viscosity η and friction coefficient κ:

$$b = \left.\frac{u_x}{\partial_z u_x}\right|_{z=0} = \frac{\eta}{\kappa}. \tag{2.5}$$

This description implies a constant viscosity within the liquid, which is not always appropriate, as for example in the above mentioned case of apparent slip.

2.2.1 Important Parameters

The slip length of a simple liquid on a smooth surface depends strongly on its contact angle [Cot2002, Lég2003]. The reason for that are molecular interactions between the liquid and the solid. In general, slippage is stronger in a non-wetting system than in a wetting system [Bar1999]. For water, a quasi-universal relationship between contact angle and slip length was found: With increasing contact angle, the slip length increases [Hua2008].

Additionally, the roughness of a surface is supposed to have an influence on the slip length as well [Cot2004, Jos2006, Ybe2007, Sch2006, Kun2007, Lun2012, Che2012]. Depending on the scale of the roughness, slippage can be enhanced [Pit2000, Zhu2002], or reduced [Pri2006, Cot2003, Nia2008].

Schmatko et al. found larger slip lengths for elongated linear molecules than for branched [Sch2005]. Ordering effects of the molecules were reported [Pri2005], as well as layering effects [Hei2007] of the liquid forming an interface area with different characteristics than the bulk.

Other reported factors are thin gas layers between the solid and the liquid [deGen2002]. This was of special interest in the last years for water on hydrophobic surfaces. A phenomenon often called 'hydrophobic gap' was subject of experimental XRR studies [Mez2006, Mac2007, Ste2003, Dos2005] and simulations [Hua2008, Mez2010, Chi2010]. The influence of tiny gas bubbles, known as 'nanobubbles' and 'microbubbles' has not yet been fully clarified [Ste2003, Dos2005, Mez2006, Ste2007, Maa2013, Pan2014]. If the liquid has electric properties, the dipole moment can also influence slippage [Cho2004].

Polymer melts are rather complex liquids where properties of the individual chain influence the characteristics of the whole liquid. For polymer melts consisting of chains, that are long enough to entangle, a reduction of entanglement at the hydrophobic solid/liquid interface is known to influence slip [Bäu2009a]. However, if polymer chains are able to adsorb at the solid wall, they can inhibit slip, because of entanglements, until large shear rates are applied that disentangle adsorbed chains and the melt, and the slip length increases [Mig1993, Bro1992, Gay1999, Tch2005, Zha2011].

Recently, our group and co-workers showed that especially well-entangled polymer melts are sensitive to their preparation history: '(...) the dewetting dynamics and rim morphology of the dewetting hole of annealed polymer films on hydrophobized substrates depend on whether the polymer has been previously in contact with air or mica, and whether the film has been pre-annealed' [Sab2015].

2.3 Wetting & Dewetting

If two infinite phases i and j meet, the molecules at the interface are not equilibrated. The formation of this interface costs energy. This free energy per area is named surface energy, respectively surface tension γ_{ij}. If a thin liquid film is in contact with a substrate, mainly two scenarios can be observed: either the film spreads uniformly over the surface (wetting), or it forms holes and starts to retract from the surface until only droplets are left (dewetting). In this scenario, three surface tensions are present: solid-liquid (sl), solid-vapor (sv), and liquid-vapor (see also Chapter 3.2). They can be combined to the spreading parameter

$$S = \gamma_{\mathrm{sv}} - (\gamma_{\mathrm{sl}} + \gamma_{\mathrm{lv}}), \tag{2.6}$$

that is a measure for the surface's wettability. For values of S between $-2\gamma_{\mathrm{lv}}$ and 0 Equation 5.2 (Young's contact angle) is valid. For values below $-2\gamma_{\mathrm{lv}}$, a gas layer moves

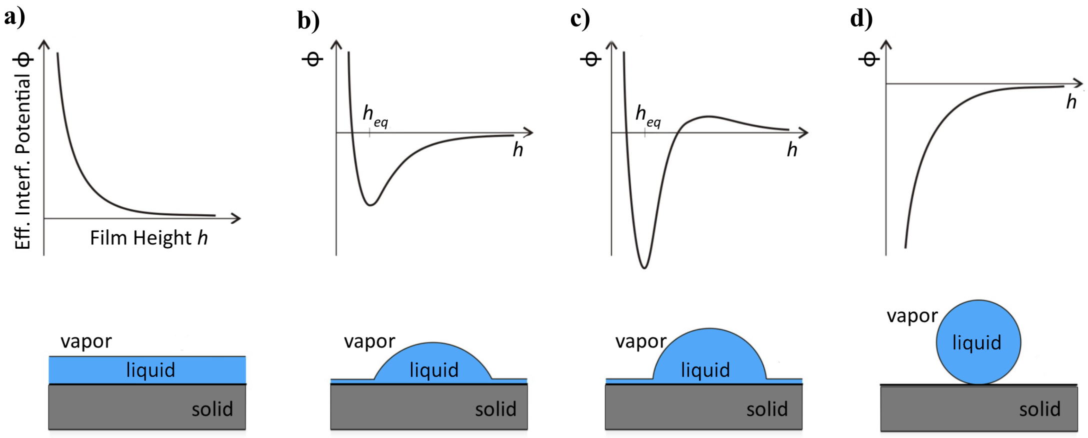

Figure 2.3: Possible shapes of the effective interface potential and the resulting wetting behavior of a film on a solid. From left to right: **a)** Stable film, the surface is completely wetted, with equilibrium film thickness $h_{\mathrm{eq}} = \infty$. **b)** and **c)** Metastable film, the surface is partially wetted. **d)** Unstable film, the surface non-wetting ($h_{\mathrm{eq}} = 0$). Sketch according to R. Fetzer [Fet2006a].

between liquid and solid, which results in the formation of droplets. In the border case of $S = -2\gamma_{\mathrm{lv}}$, they reach a minimal contact to the substrate.

To precisely describe the interface and the contact line of a thin film with thickness h, the presented description is not sufficient, since the film can not be considered as an infinite phase. Therefore, the effective interface potential $\phi(h)$ is defined as the energy per surface area that is needed to bring two infinitely separated interfaces to the distance h [Die1988]. It combines all relevant molecular forces, such as repulsive short-range interactions or attractive long-range van der Waals forces. The effective interface potential for a layered system – as a thin film on a stratified substrate – can be calculated through the sum of the individual contributions [Isr1997, Jac2008].

The shape of $\phi(h)$ determines the wetting behavior of the film on the respective substrate (see Fig. 2.3). If $\phi(h)$ has its minimum for $h \to \infty$, the film is stable and wets the substrate completely. If $\phi(h)$ has a defined minimum, the film is in a metastable state and retracts partially from the substrate until the equilibrium film thickness h_{eq} is reached, which is defined by the position of the minimum. In this case

$$\phi(h_{\mathrm{eq}}) = \gamma_{\mathrm{lv}}(\cos\theta_{\mathrm{Y}} - 1) = S \tag{2.7}$$

describes the connection between the depth of the effective interface potential and Young's contact angle θ_{Y} [You1805]. Lastly, if $\phi(h)$ has its minimum at $h = 0$ the liquid does not wet the substrate and the surface stays dry. For more information on how the wetting properties of polymers can be controlled, see [McG2015].

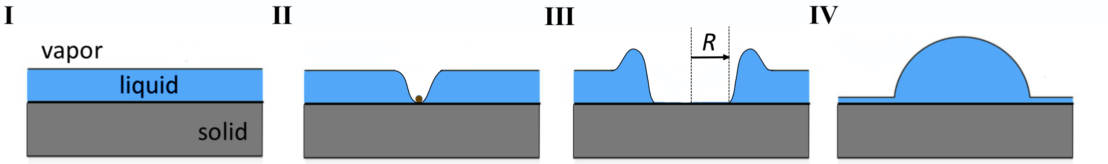

Figure 2.4: Schematic of a film rupture by heterogeneous nucleation and the development of a hole in a polymer film. **I** Glassy film as prepared on the substrate. **II** Rupture of the liquid film at a nucleation core. **III** Dewetting hole with radius R, measured from the center of the hole to three phase contact line. **IV** Late stage of the dewetting process: single droplet(s).

2.4 Methods to Determine The Slip Length

Slippage is determined in science by many different methods: In drainage experiments where a force is applied/measured, the use of a surface force apparatus [Zhu2002, Bou2008] or a colloidal probe AFM [Sun2002, Vin2011] is quite common. Tracer particles [Wan2009, Wan2011] or fluorescence recovery after photo-bleaching [Pit2000, Sch2005] can be used to visualize the flow profile. Even thermal motion of confined colloidal tracers can lead to the slip length [Jol2006]. For more insights on methods to measure slip, see articles of Lauga et al. [Lau2007], Neto et al. [Net2005] and McGraw et al. [McG2014].

In this work, the slip length is measured in a thin film system, where the flow process is driven by an internal driving force: a thin film of a hydrophobic polymer retracting from a hydrophobic surface [Rei1992, Jac1998b, Rei2009]. The slip length is measured by applying full hydrodynamic models to the observed kinetics and geometries [Fet2005, See2005, Fet2007b, Bäu2008, Jac2008, McG2015, Hae2015, McG2016]. An introduction into the used method that was developed by the Jacobs' group and co-workers is given in the following.

2.4.1 Slip Length via Dewetting Dynamics

The dewetting of a thin film is driven trough capillary forces. The effective force F_{c} per unit of length l that acts at the three-phase contact line is given by

$$\frac{F_{\mathrm{c}}}{l} = |S| = \gamma_{\mathrm{lv}}(1 - \cos\theta_{\mathrm{Y}}) \approx \frac{1}{2}\gamma_{\mathrm{lv}}\theta_{\mathrm{Y}} \tag{2.8}$$

and consist of a negative capillary force pulling towards the dry side and a positive force at the wet side, where the liquid equilibrates 'back' to the undisturbed film [deGen1985, Bro1994].

The trigger for the dewetting process of a metastable film is usually either homogeneous nucleation, due to thermal energy, or heterogeneous nucleation because of inhomogeneities of the surface or the film, as for example dirt particles that act as nucleation cores (see Fig. 2.4) [Jac1998a]. In films with a thickness of only a few nanometers, spinodal dewetting can be observed [Vri1966, Ruc1974, Mit1993, Her1998, See2001, Rau2008]. This thesis deals with film thicknesses in the range of 100 nm, where holes are expected to nucleate heterogeneously, since homogeneous nucleation is slower [Jac1998a]. Sometimes, it is possible to observe a reminder of the nucleus in form of a small droplet in the center of the hole (see AFM-scan of a hole in Figure 7.6).

Independently from the trigger mechanism, the film forms holes that grow with time (see schematic in Fig. 2.4) and photographs in Fig. 6.2 and Fig. 7.2). The growth can be analyzed by the observation of the radius R of three-phase contact line. At later stages of the dewetting process, the surrounding rims become unstable due to Rayleigh-Plateau instabilities [Bäu2014]. The holes coalesce until only a network of liquid ridges is left on the surface. These ridges retract further to single droplets. The state of droplets, connected through a thin film with equilibrium film thickness h_{eq}, is usually considered as the final state. In a perfect world these droplets would merge to one single drop, but this process known as Ostwald ripening is extraordinary slow.

In general, the energy dissipation of the flow process is a superposition of viscous friction inside the liquid and friction dissipated at the solid/liquid interface due to slip. So the velocity of the hole growth $V = \frac{\mathrm{d}R}{\mathrm{d}t}$ can be written as

$$V = v_{\mathrm{v}} + v_{\mathrm{s}} = C_{\mathrm{v}}(\theta_{\mathrm{d}})\frac{|S|}{\eta} + \frac{|S|}{3\eta}\frac{b}{\omega}, \tag{2.9}$$

where s and v indicate slip and viscous contributions [Jac1998b, Fet2007a]. As long as the contact angle stays steady during dewetting, C_{v} is a constant that acts as a measure for the flow field near the three phase contact line [Bro1994]. $|S|$, the spreading parameter, is proportional to the actual driving force of the dewetting process F_{c} [Jac1998b]. Both terms depend on the viscosity η. The slip part of this equation with slip length b is valid as long as the rim of the hole – described by its width ω and height of the undisturbed film h_0 – grows in a self-similar way [See2001]. In this case $\omega = C_{\mathrm{s}}\sqrt{R}\sqrt{h_0}$ with a proportionality constant C_{s}, and Equation 2.9 can be written as

$$V = v_{\mathrm{v}} + \frac{K}{\sqrt{R}}. \tag{2.10}$$

K combines the relevant physical parameters as

$$K = \frac{1}{3}\frac{|S|}{\eta}\frac{b}{C_{\mathrm{s}}\sqrt{h_0}} \tag{2.11}$$

to a constant. This leads eventually – after separation of variables and integration [Jac1998b] – to $R \sim t^{\alpha}$ and the data such as in Figure 2.7 is described by

$$R(t) = A(t - t_0)^{\alpha} \tag{2.12}$$

with fitting parameters A, t_0 and α [Bro1997, Mas2002, Dam2003, Mün2005]. t_0 describes the time when the hole nucleates. The exponent α varies between 1 in case of no-slip, and $\frac{2}{3}$ in case of full-slip. The free fitting parameter A acts as proportionality constant. Through a detailed analysis of the hole growth data with the help of Equation 2.10 and Equation 2.12, the slip length b can be measured.

2.4.2 Slip Length via Rim Profile Analysis

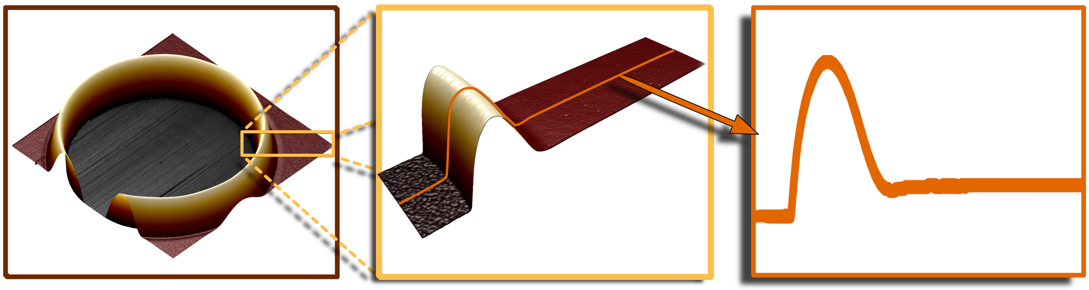

Figure 2.5: AFM scan of a hole and its rim profile, in a glassy polymer film.

During dewetting, the material from the inside of a hole is accumulated in a surrounding rim (see Fig. 2.5). All holes considered for the present thesis have reached a radius of 12 µm and the prepared film height is in the range of 100–130 nm to ensure that variations in the film height are not responsible for the changes in the observed rim profile. The radius is chosen at 12 µm, because usually at that value, the rim shows not yet significant undulations or fingers, as bigger holes lead to the development of a Rayleigh-Plateau instability [Bäu2014] (see Fig. 6.2c holes on the left edge).

Depending on the slip condition this rim has a characteristic decay on its 'wet' side into the undisturbed film. One distinguishes monotonic and oscillatory decays (see Fig. 2.6). A detailed explanation and derivation of the models to describe the shape of the rim can be found in earlier publications of the Jacobs' group [Fet2007b, Fet2005, Fet2006b, Bäu2009b]. This section gives only a brief overview on a rim shape analysis is performed to gain the slip length.

A linear stability analysis of the full Stokes equation on the 'wet' side of the rim leads to a characteristic equation

$$\left(1+\frac{h_0}{3b}\right)(h_0k)^3+4Ca\left(1+\frac{h_0}{2b}\right)(h_0k)^2-Ca\frac{h_0}{b}=0. \tag{2.13}$$

With the capillary number

$$Ca=\frac{\dot{s}\eta}{\gamma_{\mathrm{lv}}}, \tag{2.14}$$

defined by the surface tension γ_{lv}, the dewetting velocity $\dot{s}$ and the viscosity η. Equation 2.13 has two solutions for k, which satisfy the condition that the rim drops down

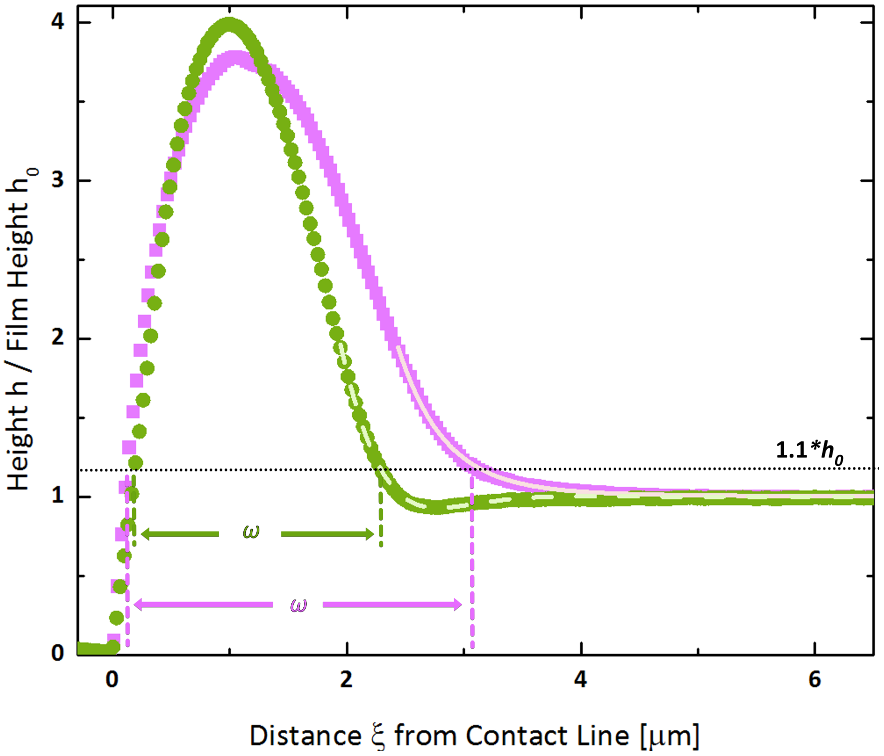

Figure 2.6: Typical representation of an oscillatory (green dots) and a monotonic (pink squares) rim profile. Dashed and solid line show models of the shapes, generated with Equation 2.16 and Equation 2.17.

to the undisturbed film. Either k_1 and k_2 can be two negative real numbers or a pair of complex conjugated numbers with negative real part.

$$k_{1,2} = k_{\mathrm{r}} \pm i k_{\mathrm{i}}. \tag{2.15}$$

Complex numbers describe the rim profile through

$$h(\xi)_{\mathrm{oszi}} = h_0 + (f \cdot \cos(k_{\mathrm{i}}\xi + \phi) \cdot \exp(k_{\mathrm{r}}\xi)) \tag{2.16}$$

as an oscillatory shaped rim, which consists in practice usually of just one single dip. Monotonic decays are modeled by a superposition of two simple decays with $k_{1,2}$ as real numbers

$$h(\xi)_{\mathrm{mono}} = h_0 + f_1 \cdot \exp(k_1\xi) + f_2 \cdot \exp(k_2\xi). \tag{2.17}$$

The frequencies f, phase shift ϕ and the attenuation constants k as well as the film height h_0 are fitting parameters.

With the knowledge of these parameters, Equation 2.13 delivers the slip length

$$b_{\text{osci}} = \frac{1}{4h_0} \frac{3k_{\text{r}}^2 - k_{\text{i}}^2}{\left(k_{\text{r}}^2 + k_{\text{i}}^2\right)} - \frac{h_0}{2} \tag{2.18}$$

and the capillary number

$$Ca_{\text{osci}} = -\frac{h_0}{8} \frac{3k_{\text{r}}^2 - k_{\text{i}}^2}{k_{\text{r}}^2} + \frac{h_0^3}{12} \frac{\left(k_{\text{r}}^2 + k_{\text{i}}^2\right)^2}{k_{\text{r}}^2}. \tag{2.19}$$

Analog, in the monotonic case

$$b_{\text{mono}} = \frac{1}{4h_0} \frac{k_1^2 + k_1 + k_2 + k_2^2}{k_1^2 k_2^2} - \frac{h_0}{2} \tag{2.20}$$

and the capillary number

$$Ca_{\text{mono}} = -\frac{h_0}{4} \frac{k_1^2 + k_1 k_2 + k_2^2}{k_1 + k_2} + \frac{h_0^3}{6} \frac{k_1^2 k_2^2}{k_1 + k_2}. \tag{2.21}$$

Compared to the analysis of a hole growing in time, the analysis of the AFM-depicted surrounding rim delivers usually results with less uncertainty. Therefore, this is the preferred method to measure slip lengths for the purpose of this thesis. Unfortunately, the method itself is not capable to distinguish between true and apparent slip.

2.5 Recent Developments & Previous Work

Most of the already mentioned studies concerning slip (see Sec. 2.4 and Sec. 2.3) deal with simple liquids, polymer solutions, or polymer melts of high molecular weight in systems with high shear rates or externally applied forces. Usually, the solid/liquid interface involves a smooth or (artificially) rough wall. Therefore, explanations for the molecular slip mechanism are for example based on entanglement reduction or roughness approaches, as presented in Section 2.2.1. However, this work is devoted to slippage and its molecular mechanism in the case of short-chained polymer melts that are unable to entangle. Due to the special choice of hydrophobic polymers and hydrophobic substrates, the system has an internal driving force for the dewetting process of a thin film, so no external shear is necessary. Thus shear rates are very low. Furthermore, the used substrates are very smooth and self-assembled. This section gives an overview of the scientific developments directly linked to the subject of the present thesis.

Slippage of a liquid is only possible if the liquid does not wet the substrate [deGen1985]. Together with an entangled polymer, these are sufficient conditions for slip. Yet, for non-entangled polymers, the sufficient condition is unclear. A lot of research in our

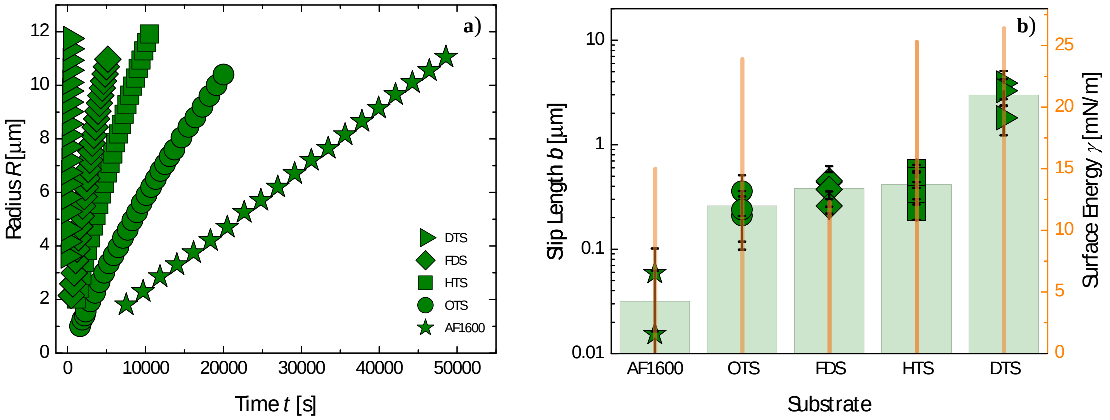

Figure 2.7: Dewetting dynamics (**a**) and slip lengths (**b**) of PS (13.7 kg/mol) on DTS (triangles), HTS (squares), OTS (circles), FDS (diamonds) and AF1600 (stars), at 110 °C. Dewetting dynamics data is shown with reduced density to enhance clarity. Green bars indicate the mean value of the respective single data points. Orange bars indicate the surface energy of the substrates. Data partially published, see [Fet2006a] for DTS and OTS data; [Bäu2008] for DTS, OTS and AF1600 data; [Bäu2010a] for DTS, OTS and AF1600 data; [Bäu2012a] for DTS, HTS, OTS and AF1600 data; [McG2014] for DTS, OTS, FDS and AF1600 data.

group was done to study whether the substrate is a candidate to enable slippage of non-entangled polymer melts.

From the knowledge that the slip length of non-entangled polymers is very small on amorphous low surface energy Teflon® AF1600 coatings [Bäu2008], the surface energy itself was subject of research, whether a certain level of surface energy is necessary and sufficient for slippage. Experiments on fluoridated silane SAMs, which also feature a low surface energy, showed that the slip lengths of PS were comparable to slip lengths on other non-fluoridated silanes rather than to PS on AF1600 (see Fig. 2.7b). Consequently, surface energy could be ruled out as being the only reason for slippage [McG2014]. Eventually, a hypothesis was developed that low surface energy is necessary but not sufficient for the observed slip lengths. Instead, the structure of the substrate seems to play a major role, combined with a liquid that is affected by this structure.

Fetzer et al. [Fet2007a, Fet2005] studied the slip behavior of non-entangled polystyrene melts on hydrophobic self-assembled monolayers of silanes with two different chain lengths (OTS, DTS). On both substrates, slip lengths were significantly higher than the prepared film thickness of about 100 nm. Although, both used silane substrates were chemically identical, equally rough and hydrophobic, slip lengths on the shorter silane SAM were one order of magnitude greater than on the longer SAM (see Fig. 2.7b). A direct link between the length of the silane molecules and the slip length is a too simple approach as measurements on intermediate long silanes (HTS) showed [Bäu2012a]. Although, with 16 carbon atoms the length of the HTS chain is closer to the length of OTS than to DTS, a corresponding tendency of the slip length was not clearly visible (see

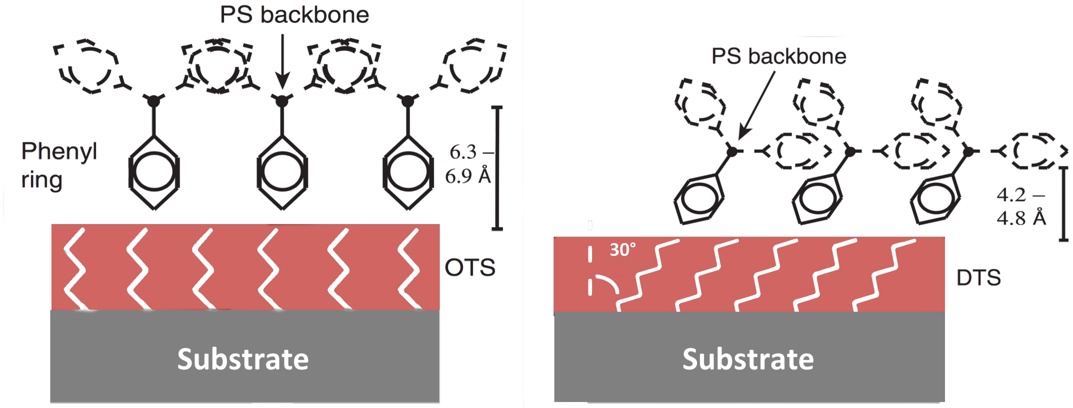

Figure 2.8: Schematics of the solid/liquid interface of a PS film on OTS (left) and DTS (right) as deduced from X-ray reflectometry analysis [Gut2013].

Fig. 2.7). Besides the implications of these findings, reducing the properties of a SAM to the length of the individual chains is not appropriate, since it is not a matter of course to assume the chains as being stiff, non-deformable, or upright standing [Cas2015].

With the help of scattering experiments, our group and co-workers [Gut2013] analyzed polystyrene films on DTS and OTS substrates and found electron density depletion zones between the respective substrate and polymer melt. They correlated the different heights of the zones with tilt angles of the polystyrene's side groups (see Fig. 2.8). According to their model calculations, the phenyl side groups should have a tilt angle of about 30° on DTS and less than 10° on OTS. Both tilt angles would correspond to the averaged tilt angle of the silane chains in the underlying SAM. Accordingly, the adjacent chain segments are flatly oriented relative to the substrate. Since scattering experiments are not able to actually visualize the true molecular order – especially in lateral direction – this hypothesis was the starting point of the present thesis.

MD simulations and sum-frequency generation spectroscopy on simple hard surfaces have shown, that polystyrene and its side groups are able to orient along a wall [Hud2011, Lyu2011, Gau2000, Cla2001] and at the liquid/air interface [Bri2001]. Furthermore, aromatic rings like benzene or phenyl rings are known to be able to orient relative to each other, known as π-π-stacking (e.g. [Nak2014, Nak2003, Jor1990, Rav1985]). Such a layer of oriented molecules could act as an effective substrate on top of the actual substrate and influence the motion of the rest of the polymer film.

Dewetting of polymers on top of brushes of polymers of the same type is well-studied in literature [Pas2006, Che2016]. In these cases, slip is often a matter of interpenetration between the fixed polymer brushes and the mobile melt. Especially polystyrene, PDMS and PMMA are common examples for such an autophobic behavior [Rei2000b, Lee2016, Xue2009, Mac2005].

Polymers are of common interest in simulations. Mostly, polymers are described by a coarse-grained model flowing over a simple solid substrate [Ser2008, Pri2004, Pri2010], an artificially structured surface [Tre2013, Pri2005, Che2012], or a polymer brush [Mül2009, Pas2006, Pas2008]. Often the highest slip length is reported for the smoothest substrate [Che2012]. Although such studies are very useful to describe the dynamics of the polymer and the individual chains, the monomers are usually considered as a simple link in the polymer chain. To see individual arrangements of the monomers, all atom simulations are necessary. For example Hudzinsky et al. [Hud2011] studied the internal structure and density of atactic polystyrene under shear and compared a capped to a supported film. Clancy et al. [Cla2001] combined the coarse-grained approach with an atomistically detailed model, to simulate the orientation of the phenyl rings at the liquid/air interface, inspired by the experimental findings of Gautman et al. [Gau2000] and Briggman et al. [Bri2001].

Self assembled monolayers of silanes are a popular model system and thus very well studied. Their growth process was subject of in situ monitoring on various substrates, as for example on silicon [Bie1995, Wan2003, Kul2005]. The resulting surfaces are well characterized by X-ray methods, AFM roughness measurements and surface energy determination [Pet2002, Ste2015, Les2015]. In the meantime, a broad understanding of their internal molecular structure was also developed with the help of MC (e.g. [Bar2000]) and MD simulations (e.g. [Zha2001, Yam2006, Yam2008]). An important characteristics, the tilt angle of the SAM molecules, is mainly but not only defined by their surface density, also the bonding lattice has an influence [Zha1995]. Chandross et.al. [Cha2004] studied the effect of disorder on the nanotribology of SAMs and found out, that on ordered SAMs the friction shows a non-monotonic dependency from the number of carbon atoms in the backbone of the silane, whereas on disordered SAMs the friction is independent of the number of carbon atoms.

Unfortunately no study is fully suitable for the experimental situation in the present thesis of a non-entangled polymer melt moving over complex surfaces of silanes, where not only the dynamics are subject of interest, but also a possible structure formation of individual chain segments. Therefore, tailored all-atom MD simulations of polystyrene on silane surfaces were initiated to supplement the experimental studies (see Chap. 8). Experiments and simulations presented in this thesis are dedicated to identify and rule out possible candidates for the missing sufficient precondition to enable slippage of non-entangled polymers.

3 Methods of Measurement

During this work, a variety of different experimental methods were used. Optical microscopy captures the dynamics of the dewetting process. Also, contact angles to derive the surface energy and hydrophobicity are measured by optical methods. Atomic force microscopy (AFM) is used to image the topography and roughness of the prepared films and surfaces. The AFM is also suitable to scan remaining droplets of the polymer film in order to measure their contact angle with the substrate.

A big part of this work is dedicated to the development of a molecular picture that could explain the slip mechanism: On the experimental side, X-ray reflectometry was used to analyze the structure of the self-assembled monolayers and the polymer films. This was continued, starting form the results of collaborative work of the Jacobs' group with Philip Gutfreund and Max Wolf [Gut2013], in close cooperation with the team of beam line 9 (BL9) at the DELTA synchrotron: Michael Paulus and Christian Sternemann. A theoretical modeling in terms of molecular dynamics simulations is presented in Chapter 8, which results from a collaboration with Laurent Joly (Institut Lumière Matière, Lyon, France).

This chapter gives an overview of the measuring instruments, as well as the components of the studied systems, and techniques to prepare them.

3.1 Optical Microscopy

To capture the dynamics of the dewetting polymer film as for example seen in Figure 7.2, a Leica DM 2700 M optical microscope (Leica Microsystems GmbH, Wetzlar, Germany) was used (see Fig. 3.1). The microscope is equipped with a LED light source and a set of long working distance objectives in the range from 5 to 100 times magnification (Leica N PLAN). Furthermore, the eyepiece gives another 10 times magnification. All objectives and the microscope itself are able to operate in dark field mode, which is useful to see a possibly present dust contamination of the samples and of the films during preparation. Two polarizing filters allow to see optically active materials.

A five megapixel color camera (Leica MC 170 HD) is attached to a computer that runs Leica LAS V4.5 to record and process images. A Linkam heater with attached controller (TMS 92; temperature precision: 0.1 °C), operated via LabView, heats the sample during the actual dewetting experiment.

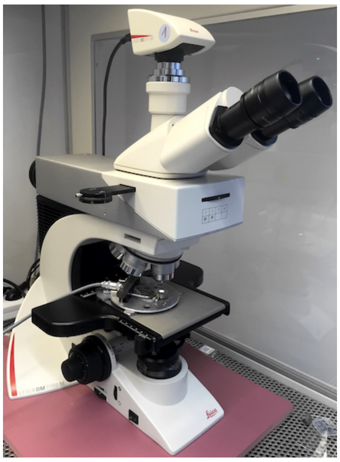

Figure 3.1: Optical microscope Leica DM 2700 M with mounted Leica MC 170 HD camera and a Linkam heat stage attached to a Linkam Controller TMS 92 (out of image section).

To extract the hole radii from a series of pictures a custom script based on ImagePro$^{©}$ Plus 4.5 (Media Cybernetics Inc., Rockville, MD, USA) was programmed. The script detects the hole, traces the three phase contact line and records the averaged diameter with the corresponding uncertainty (standard error of the mean) as a function of time.

3.2 Contact Angle Measurement with Optical Microscopy

An easy method to characterize the wetting properties and the energy of a surface is to measure the contact angle of a liquid on top of this surface (sessile drop method). This can be done for macroscopic droplets by optical microscopy. A customized setup that is inspired by the system OCA 15 Plus (Dataphysics Instruments GmbH, Filderstadt, Germany) illuminates the droplet from one side, while a camera (camPro03, EHD Imaging GmbH, Damme, Germany) with a zoom objective (Optem 70XL, Thales Optem Inc., Fairport, NY, USA) captures images from the opposite side (see Fig. 3.2).

Two picture series are recorded: one while the droplet is pumped up with liquid and another while sucking out the liquid again. During the first phase when the droplet increases its size and pushes the three-phase contact line, the advancing contact angle is captured. The receding contact angle is measured in the second phase, when the droplet shrinks again. The difference between advancing and receding contact angle gives the hysteresis, which is a measure for the smoothness and chemical homogeneity of the surface. The mean of the two values is taken as the equilibrium contact angle.

With the help of OCA 20 (Dataphysics Instruments GmbH) the pictures of the droplets are computed and analyzed concerning their left- and right-sided contact angle. To do

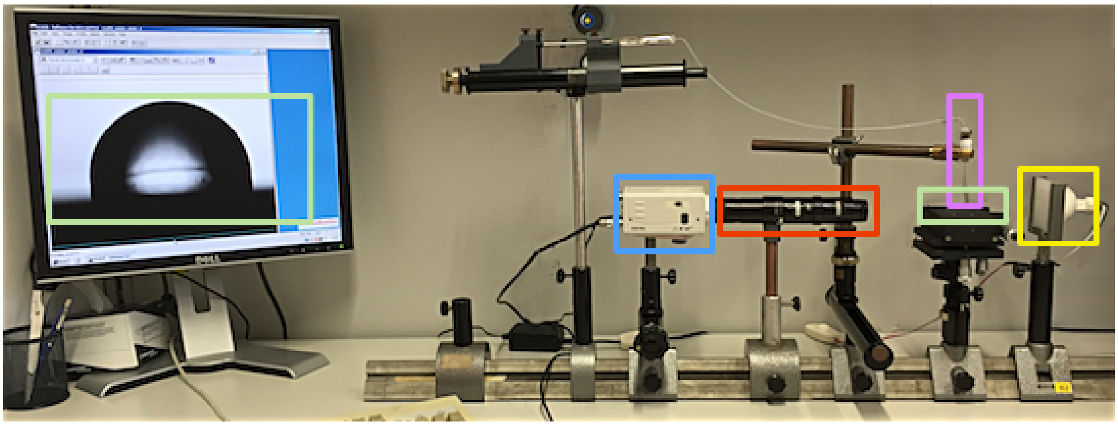

Figure 3.2: Setup to measure contact angles by optical microscopy: light source with diffuser (yellow), sample stage with sample (green), tube (purple) connected to a syringe, zoom objective (red), and camera (blue).

so, the software fits in every frame a segment of an ellipse to the droplet shape[1] and calculates the angles.

3.3 Atomic Force Microscopy

Besides optical methods to capture droplets, holes, films and surfaces, an atomic force microscope (AFM) provides the possibility to capture the actual shape and topography. The technique of the AFM goes back to the mid 1980's where G. Binnig and H. Rohrer invented the scanning tunneling microscope [Bin1982, Bin1986], the base of modern scanning probe methods.

As a probe, usually a pyramidal tip of a size of some microns scans a surface. The contact area between tip and surface is accordingly small, typical tip radii are in the range of a few nanometers, thus the contact area is less than $50\,\text{nm}^2$, which enables the high resolution of an AFM. Under optimal conditions, even atomic resolution can be achieved.

The tip is attached to a small cantilever that is fabricated out of a silicon chip. Besides silicon or silicon nitride, also tips built from diamond, carbon nanotubes or plastics with various geometries are available. With the help of a piezo scanner, the probe is able to follow the topography of the surface with sub-nanometer precision (see Fig. 3.3b). Due to interactions of the tip with the surface, the cantilever gets bent. A laser, focused on the backside of the cantilever, projects the deflection to a four-quadrant photodiode. This signal is computed through a feedback loop to operate the piezo(s).

---

[1] An ellipse is used instead of a circle to compensate the influence of the syringe's tube.

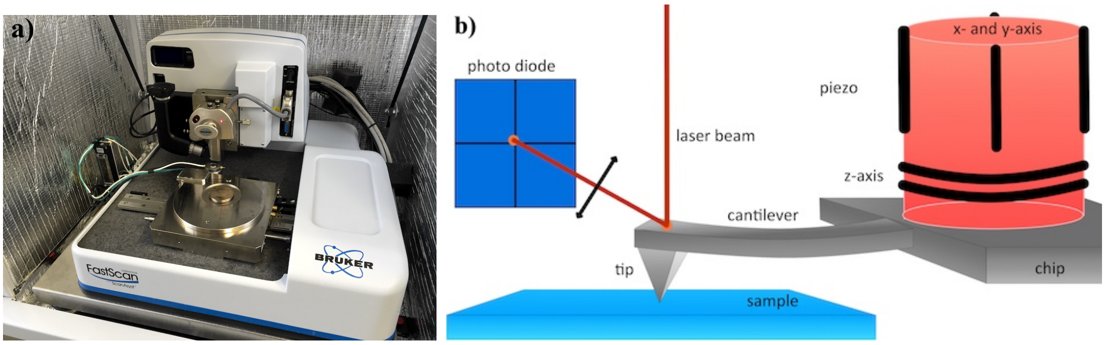

Figure 3.3: a) AFM Bruker Dimension FastScan, but with installed Icon (StarGate) head. **b)** Functional principle of an AFM.

In the basic operation mode – called *contact mode* – the tip stays in contact with the surface while scanning. To minimize wear of the tip (and/or the surface), AFMs are also capable of operating in *intermittent contact mode*, which avoids a permanent contact of the tip with the surface.

3.3.1 TappingMode$^{\text{TM}}$

A commonly used intermittent contact mode is *TappingMode*^{TM}, which is especially suited to characterize sensitive polymer films and liquid droplets [Rei2000a, Her2000, See2001, Fet2005, McG2011, McG2016]. The cantilever gets externally oscillated next to its resonance frequency to a constant amplitude. When the tip approaches the surface, the formerly free oscillation is damped, due to interactions with surface. Typically, the tip touches the surface only in the lower turning point of its movement. While scanning, the amplitude is re-adjusted to the initial value, but the phase changes. Both, the control signal of the amplitude and the phase change are recorded, together with the topography. The amplitude signal emphasizes edges, while the phase shift is a measure for energy dissipation.

3.3.2 PeakForce QNM®

A recent advancement to the pure TappingMode$^{\text{TM}}$ is PeakForce Tapping$^{\text{TM}}$ combined with quantitative nanomechanical property mapping, commercially named *Peak Force QNM*® (PFQNM) [Pit2010, Bit2012]. It adds the advantages of capturing force distance curves [But2005, Seo2007, Car2007] to TappingMode$^{\text{TM}}$, while maintaining its typical speed and resolution. Every time the tip hits the surface, a force-distance curve is captured, and therefore parameters like elasticity, adhesion, and deformation can be recorded at every scan point. In contrast to TappingMode$^{\text{TM}}$, the drive frequency is far below the resonance frequency, and not the amplitude of the oscillation is kept constant, but the maximum deflection of the cantilever, which means the maximum applied force.

Because of this precise control of the force, along with the gained information, PFQNM is especially suitable for soft samples (e.g. in biology [Los2014, Ple2011]), as well as to probe the hardness of samples [Trt2012].

3.3.3 Equipment

All AFM images in this thesis are captured with a Bruker Dimension Icon® (see Fig. 3.3a) or a Dimension FastScan™ (Bruker Nano Surfaces, Santa Barbara, CA, USA) which is equipped with a Nanoscope V controller. The main differences lies in the features of the exchangeable scan heads: The FastScan™ reaches scan speeds in the range of 100 Hz, but the x-y scan range is reduced to 35 µm × 35 µm compared to 90 µm × 90 µm for the Icon head. Since the imaged samples have no or slow dynamics the high scan rates of the FastScan™ are not necessary. Also the differences in scan range are not of any concern, because the typical image size of a rim, hole or substrate does not exceed 25-30 µm. So both setups were used equally.

As probes, standard Olympus tips (OMCL-AC160TS) with a typical radius of 7 nm were used along with Bruker FASTSCAN-A probes with 5 nm radius. A typical workflow with the AFM is indicated in Figure 2.5: The surrounding rim of a hole in the range of 24 µm diameter is scanned in detail. From this cross-section single scan lines are extracted from which the slip length gets calculated (see Sec. 2.4.2).

3.4 X-Ray Reflectometry (XRR)

X-ray reflectometry is a common tool used to resolve and characterize thin layers and their electronic composition (e.g. [Mez2006, Gut2013, Les2015, Ric1998, Ste2014]). Most of the XRR measurements in this thesis were performed at beam line 9 (BL9) at **D**ortmunder **El**ek**t**ronenspeicherring**a**nlage (DELTA) a synchrotron at TU Dortmund, Germany.

DELTA consists of three main components: the linear accelerator (LINAC), a booster synchrotron (BoDo) and the actual electron storage ring (see Fig. 3.4). Electrons emitted by the gun are pre-acclerated through LINAC. The transfer channel T1 leads them to BoDo which completes the acceleration. Through T2, electrons with an energy of approx. 1.5 GeV and a beam current of 130 mA enter the outer storage ring, where they stay with a lifetime of approx. 10 h [Tol2008].

The actual radiation for BL9 is generated by a superconductive asymmetric wiggler (SAW), which has a critical energy of 7.9 keV. A Si (311) double-crystal monochromator provides an energy resolution of $\Delta E/E \simeq 10^{-4}$ that enables to choose energies in the range of 4-30 keV [Pau2005, Kry2005]. The width and the height of the beam is defined by an array of slits acting as a collimator. This results in a beam size of 1 mm × 0.2 mm

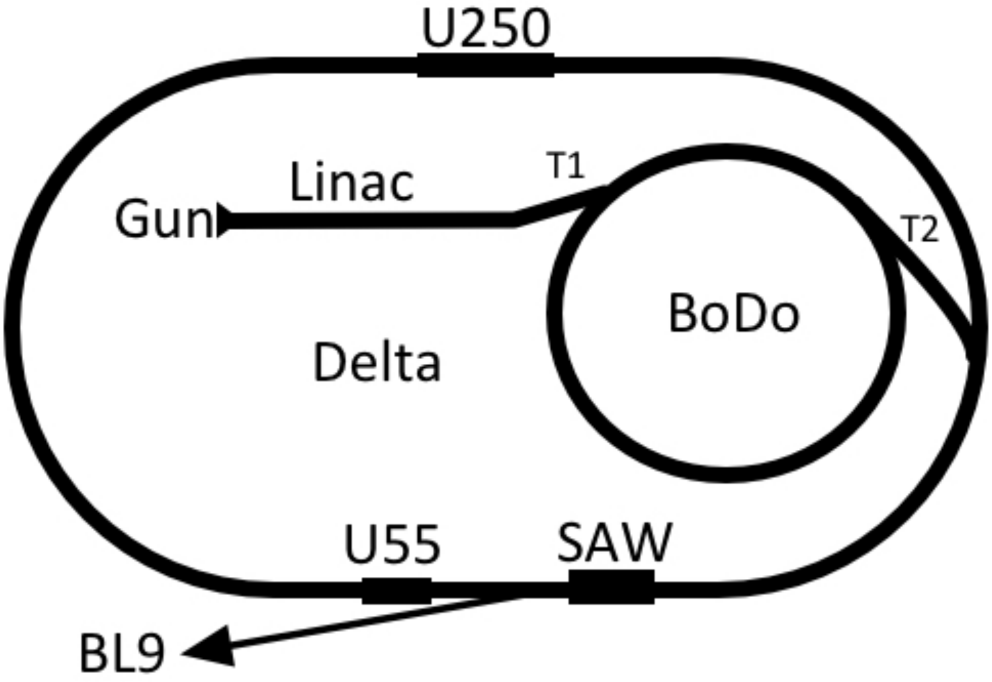

Figure 3.4: Simplified design of **D**ortmunder **El**ek**t**ronenspeicherring**a**nlage (DELTA): The sketch shows the electron gun, the linear accelerator (LINAC), the booster synchrotron (BoDo) and the outer electron storage ring. T1 and T2 are transfer channels. U55, U250 and SAW are insertion devices. SAW feeds BL9 [TUD2016].

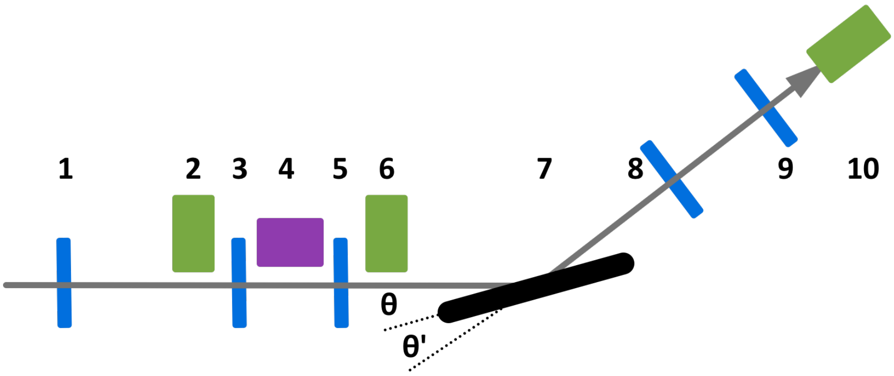

Figure 3.5: Pathway of the beam at BL9 according to [Pau2008]: 1, 3, 5, 8, and 9 slit systems; 2 and 6 NaI normalization detectors; 4 auto-absorber and fast shutter; 7 sample; 10 NaI detector.

at the sample position. A silver foil auto-absorber ensures that the flux is limited. Before and after the auto-absorber, two NaI detectors measure the flux before the beam hits the sample.

The sample is mounted on a six-circle diffractometer. The reflected beam passes a final slit system that defines the typical angular resolution of about 0.015° before another NaI detector measures the reflected intensity (see Fig. 3.5). For more information on BL9 please refer to the detailed description of the setup [Pau2008].

Measurements in Chapter 5.3.4 are performed with a Bruker AXS D8 diffractometer that uses a sealed X-ray tube with a line focus copper anode (40 kV, 40 mA). This corresponds to a typical beam energy of 8 keV. Due to the low flux compared to BL9, measurements take longer at this device. Moreover the intensity at higher scattering angles decreases, which lowers the range in scattering vector q_z (see Chap. 5.3.1). Also the resolution concerning the angle itself is decreased because of a more divergent beam.

The handling and fitting of the data acquired by XRR is described in Section 5.3.

4 Materials

The system prepared for dewetting experiments is a glassy polymer film on top of a hydrophobized silicon wafer or quartz crystal (see Fig. 4.1). This section gives an introduction to the polymers, coatings, and substrates, used in the present thesis.

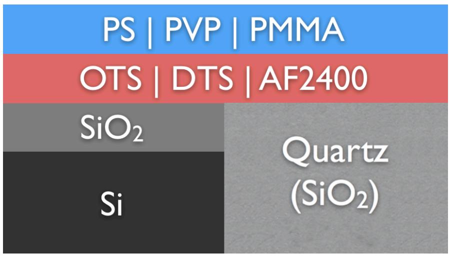

Figure 4.1: Schematic of the prepared dewetting system: A polymer film floated on a hydrophobized wafer. The used silicon wafers usually carry a natural oxide layer of various thickness.

4.1 Polymers

Polystyrene (PS) and polymethyl methacrylate (PMMA) are two of the most used plastics. CD cases or some food packages for example are made out of PS. A lot of packing and insulating material are made of foamed PS. PMMA is better known by the names acrylic glass, Perspex®, or Plexiglas®. Besides those two popular polymers, poly(2-vinyl) pyridine (PVP) is used, because of its similarity to PS (see Fig. 4.2). These three polymers were chosen because of their side groups: Polystyrene features a phenyl ring with a delocalized electron (π-electron system). With PVP, the electron system is altered by replacing one carbon atom with a nitrogen atom, but keeping the ring-like side group structure. In the case of the used poly(2-vinyl) pyridine, the second carbon atom (starting from the bonding side clockwise) is replaced. Therefore, the abbreviation P2VP is also common to distinguish it from other variants. The particular PVP in the present study is terminated with COOH. Table 4.1 lists physical properties and suppliers for polymers used in this work.

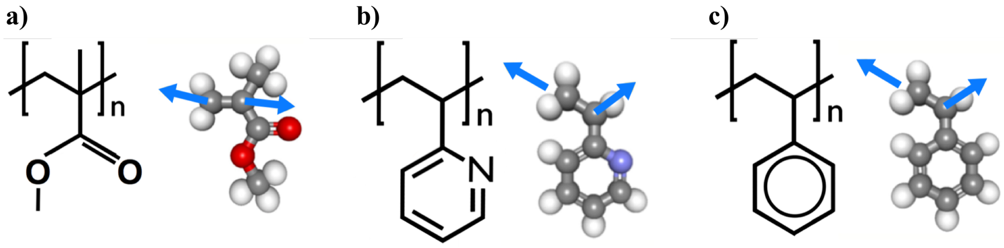

Figure 4.2: Monomeric unit of **a)** poly(methyl) methacrylate (PMMA), **b)** poly(2-vinyl) pyridine (PVP) and c) polystyrene (PS) in ball-and-stick representations [Hil2010, Mol2006] and as chemical formulas.

4.1.1 Composition & Structure of Polymers

The size of a polymer chain with N covalently bound monomers (see Fig. 4.2) can be characterized by its molecular weight

$$M_N = NM_{\text{mono}}, \tag{4.1}$$

where M_{mono} is the molecular weight of a monomer. Values are given by 104 g/mol for PS, 100 g/mol for PMMA, and 105 g/mol in the case of PVP. N is also called the degree of polymerization. Usually not all polymers in a given sample have the same degree of polymerization. This is expressed by the polydispersity index (PDI) which is defined as the ratio between mass average molar mass M_{w} and number average molar mass M_{n}

$$PDI = \frac{M_{\text{w}}}{M_{\text{n}}}. \tag{4.2}$$

The mass average molar mass is given by

$$M_{\text{w}} = \sum_N w_N M_N, \tag{4.3}$$

with w_N the weight fraction of a polymer with degree N. Accordingly the number average molar mass is defined as

$$M_{\text{n}} = \sum_N n_N M_N, \tag{4.4}$$

where n_N is the number fraction of a polymer with degree N. A sample that consists only of polymers with the same degree of polymerization has a PDI of 1 and is described as monodisperse. The index increases with polydispersity. For more information on molar mass distributions see Reference [Rub2003].

Polymers used during this thesis feature a PDI close to 1 (see Tab. 4.1), where available. The only exception are experiments with isotactic polystyrene in Chapter 9, where no such quality was commercially available at the date of the study.

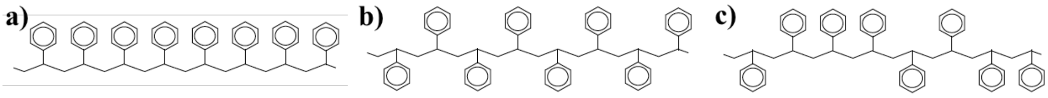

Figure 4.3: Tacticity of a linear polystyrene chain: **a)** isotactic **b)** syndiotactic, and **c)** atactic.

Monomers can be combined in different ways to form polymers. The way they combine is defined during the polymerization process. The resulting microstructure has, besides the chemical composition, a major impact to the physical properties. The orientation of the side group is described by the tacticity. If the side groups point in the same direction, the polymer is called isotactic. A chain with equally distributed side groups to either side is called syndiotactic, whereas a random distribution is named atactic. Figure 4.3 gives an overview over the possible orientations.

Polymers can branch out in different ways: A simple linear chain, a ring- or star-like structure even more complex architectures like comb-structures are possible. Usually such a structure is not stretched out to its maximum length, but – due to entropic reasons – coiled. So the spatial extent is measured by the radius of gyration R_g, which is defined as the mean quadratic distance of the monomers from the polymer's center of mass:

$$R_\mathrm{g}^2 = \frac{1}{N^2} \sum_{i=1}^{N} \sum_{j=1}^{N} \left(\vec{R}_i - \vec{R}_j \right)^2 . \tag{4.5}$$

For a linear chain the averaged radius of gyration is given by

$$\langle R_\mathrm{g}^2 \rangle = \frac{b^2 N_\mathrm{K}}{6}, \tag{4.6}$$

where b is the length and N_K the number of Kuhn monomers [Rub2003]. In the case of PS $b = 1,8\,\mathrm{nm}$ and $N_\mathrm{K} = \frac{M_N}{720\,\mathrm{g/mol}}$ [Rub2003]. For example for PS of 10 kg/mol $R_\mathrm{g} \approx 10\,\mathrm{nm}$.

4.1.2 Glass Transition

Depending on the temperature, a polymer can be solid or liquid, but it can also be glassy. The temperature at which this transition takes place is called glass-transition temperature T_g. An atactic polymer forms an amorphous phase after the cool down below T_g, whereas a polymer with isotactic parts tends to crystallize. The glass transition is not a phase transition of first order at a precise temperature. Rather, depending on the cooling rate, it takes place over a range of temperatures where the motion of the chains freezes. 'Freezing' is in this sense a matter of the time scale at which the motion is considered as frozen or stopped. Because the chains are not re-arranged this is called a second order phase transition.

Since short chains are more mobile than longer ones, the glass transition temperature is reduced with molecular weight. The film thickness has an influence on T_g, as well. This topic is under vivid discussion and has been demonstrated for supported and free-standing films well below 100 °C [Ked1994, Mat2000, Dal2000, Her2001, Bäu2012b]. To exclude such effects, only molecular weights well above 5 kg/mol and below 100 kg/mol, are used for this work. Furthermore, films are usually prepared with a thickness of about 100 nm and above. Films with 50 nm thickness are only used for XRR, where no monitoring of the dynamics is needed, but a thinner film thickness has advantages in the evaluation of XRR data. Films with these parameters feature bulk-like glass transition temperatures (see Tab. 4.1).

4.1.3 Viscosity

A liquid reacts to a shear stress with a certain shear strain. If the shear rate $\dot{\gamma}$ is proportional to the applied shear stress σ the liquid is named **newtonian**. The constant of proportionality is named viscosity η (see also Section 4.1.3). The relation

$$\sigma = \eta\dot{\gamma}, \tag{4.7}$$

with components $\sigma_{ij} = \eta\dot{\gamma_{ij}}$, where $\dot{\gamma_{ij}} = \partial u_i/\partial x_j + \partial u_j/\partial x_i$, tells also that a Newtonian liquid can transmit shear forces vertical to the direction of shear. This would not be the case for an ideal liquid without viscosity, because there would be no friction between single liquid layers.

In contrast to a purely Newtonian liquid, most realistic liquids feature a shear rate dependent viscosity $\eta\dot{\gamma}$. The liquid is named **shear thickening** if the viscosity increases with shear rate, and **shear thinning** in the opposite case. Especially long chained polymers perform in such a **viscoelastic** way, where an initial shear strain heals within a specific time τ. For short time scales, $t < \tau$, the liquid's behavior is elastic, and for $t > \tau$ viscous.

For a given kind of polymer, the viscosity of the melt is mainly defined by molecular weight and temperature. A higher temperature enhances the mobility of the chains and therefore reduces the viscosity. As already stated the chain's motion is not stopped below T_g, it's just extremely slow, which means that the viscosity can reach high values.

The WLF-equation (Williams, Landel, and Ferry [Wil1955]) gives a relation between viscosity and temperature:

$$\eta = \eta_0 \exp \frac{B(T_\mathrm{g} - T)}{f_\mathrm{g}(T - T_\infty)}, \tag{4.8}$$

with η_0 the viscosity at $T = T_\mathrm{g}$, T_∞ named Vogel temperature[1], f_g the polymers free volume, and B an empiric constant.

---

[1] Typically T_∞ is approx. 50 K below T_g, where the free volume reaches zero [Rub2003].

	Tacticity	Supplier	M_e [kg/mol]	M_w [kg/mol]	*PDI*	T_g [°C]
PS13k	atactic	PSS	16.6*	13.7	1.03	≈ 95
PS12k	atactic	PSS	16.6*	12.5	1.03	≈ 95
PSb	atactic	PSS	16.6*	47	2.35	$\approx 95^{\sharp}$
iPS	isotactic	Polymer Source	16.6*	108	3.48	$\approx 95^{\sharp}$
PVP10k	atactic	Polymer Source	$\approx 16^{\blacklozenge}$	10.8	1.08	≈ 78
PVP56k	atactic	Polymer Source	$\approx 16^{\blacklozenge}$	56.0	1.06	≈ 96
PMMA14k	atactic	PSS	12.5*	14.0	1.03	≈ 101
PMMA57k	atactic	PSS	12.5*	57.8	1.03	≈ 110

Table 4.1: Physical properties of the used polymers (PS13k was not used in experiments during this work, but is listed as comparison to former work). Where not otherwise indicated, values are taken from data sheets of PSS Polymer Standards Service GmbH (Mainz, Germany) and Polymer Source Inc. (Montreal, Canada); *[Mar2007]; $^{\blacklozenge}$[Cre1991]; $^{\sharp}\mathrm{T_g}$ estimated from values of comparable monodisperse atactic polystyrene.

The same argument of the glass transition being reduced with molecular weight holds for viscosity: A longer chain has a reduced mobility and with that an increased relaxation time, so the viscosity is increased. For low molecular weights this is described by the Rouse-Model with a linear behavior [Zim1956, RouJr1953]. However when the molecular weight is higher than a critical value named M_e, entanglements between the different chains come into play. This effect has no significant influence on the viscosity until the critical molecular weight M_c is reached. M_c is always 2–4 times larger than M_e [Rub2003]. Beyond this point the linear behavior changes to a power law with an exponent of 3, theoretically determined by de Gennes [deGen1971], respectively 3.4, experimentally found [Rub2003, Bäu2010c].

Since the reason for slip above M_c is well understood by the density of entanglements inside a liquid [deGen1971]. Essentially a stronger network, formed by longer chains, enhances the interfacial slip [Bäu2012a], this work focuses mainly on molecular weights below M_c, except for experiments in Chapter 7.3 where the molecular weight dependency is tested for PMMA and PVP.

4.1.4 Polymer Film Preparation

Polymer films can be prepared by dip-, spray-, or spin-coating out of a polymer solution. For this work, either toluene or tetrahydrofuran (THF) were used for spin coating. A drop of polymer solution is put onto the substrate, which rests on a rotation stage. Immediately after putting the droplet, the stage is set into rotation. Because of centrifugal force, the liquid gets uniformly distributed across the surface, the solvent evaporates and a smooth homogeneous polymer film remains. The thickness h of the film depends on the concentration of the solution c and the speed of rotation ω, an empirical equation connects these parameter:

$$h = A\sqrt{\frac{c^3}{\omega}}. \tag{4.9}$$

A is specific empiric constant for each polymer and entails the molecular weight. In the context of this thesis polymer solutions in the range of 30 mg/ml are used at rotation speeds between 2000–4000 min^{-1} with the goal to prepare film heights in the range of 100–150 nm. Thinner films for XRR studies (see Sec. 7.4) with thicknesses in the range of 50 nm are prepared by lowering the concentration of the solution.

Since all surfaces used are highly hydrophobic, the solution would roll off the surface, therefore a direct spin coating is not possible. Instead, films are spin coated on freshly cleaved (hydrophilic) mica sheets and afterwards floated onto ultra-pure water (TKA-genpure, 18.2 MΩ at 25 °C, 6 ppb). Then, the film is picked up from the water surface with a hydrophobized wafer sample, that was cleaned in ultra-sonic baths of ethanol, acetone and toluene. The film rests now in a metastable, glassy state on the surface. The sample is stored and treated under clean room conditions where possible.

4.2 Substrates

The basic requirement for a controlled surface coating is a controlled surface itself. Silicon and quartz wafers that are used in semiconductor or optical industry, can be produced in a very controlled way. Their chemical composition is exactly reproducible as well as their roughness, which is – after a polishing process at the manufacturer – typically in the range of angstroms.

4.2.1 Silicon Substrates

Silicon wafers are delivered by Si-Mat (Kaufering, Germany) with (100)-orientation and p-doped with boron. This results in a typical resistance of 10-20 Ω/cm, according to the manufacturer. Wafers used in this work feature an amorphous native silicon oxide layer (SiO_2) of about 1.7 nm [Los2012a]. Usually, the polished side shows a RMS roughness in the range of 0.14(2) nm [Les2015].

4.2.2 Quartz Substrates

Quartz has a crystalline composition and develops no amorphous oxide layer, so it offers structured bonding sites for silanes in contrast to the amorphous silicon oxide layer.

Experiments on quartz where initially designed to pave the way for simulations with silane bonding sites on a simple lattice. Independently from that, it is possible to see effects of an altered substrate structure to the dewetting dynamics (see Chap. 6).

Nano Quarz Wafer GmbH (Langenzenn, Germany) delivered wafers cut from a single crystal with 34° relative to the XY-plane. The cut angle defines the resonance frequency of the quartz. A polishing on both sides down to a roughness below 0.5 nm was necessary to minimize tensions and deflections of the wafer that made XRR impossible (see Chap. 5.3.4). As a consequence, the wafers are translucent.

4.3 Coatings

A set of hydrophobic coatings is used to drive the dewetting process: Most important are self-assembled monolayers of silanes, that have become popular hydrophobic surfaces. They deliver a reproducible quality, are naturally homogeneous and smooth, and – because of their covalent bonds to the substrate – mechanically robust. The ready-made samples are easy to handle and easy to clean. Silanes act in our model system as a 'structured' surface, whereas polytetrafluoroethylene (PTFE), often called Teflon$^{\mathrm{TM}}$, is the amorphous companion.

4.3.1 Silanes

Silanes consist of two main parts named head and tail, also called backbone. The head is a silicon atom that is saturated with three chlorine atoms. The forth bond of the silicon atom connects to the tail that consists of a number of carbon atoms saturated with hydrogen. During this work, two silanes were used: one with twelve and the other with eighteen carbon atoms in the backbone (see Fig. 4.4). Their full names are dodecyltrichlorosilane ($CH_3(CH_2)_{11}SiCl_3$, termed 'DTS') and octadecyltrichlorsilane ($CH_3(CH_2)_{16}CH_2SiCl_3$, termed 'OTS') both supplied by Sigma-Aldrich Chemie GmbH (Munich, Germany).

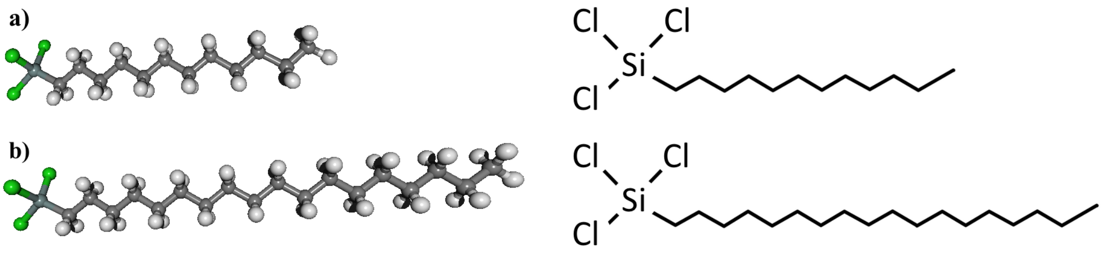

Figure 4.4: Ball and stick model [Hil2010, Mol2006] of **a)** DTS, and **b)** OTS. Chemical structure according to Sigma-Aldrich's data sheets [Sig2016b, Sig2016c].

Through a wet-chemical process [Sag1980] the head group binds covalently to the silicon oxide of the substrate. Besides that, a cross-binding between the head groups is possible [Wan2003, Yam2008]. The growing patches connect to a uniform self-assembled monolayer (SAM) building a surface that consist of hydrophobic CH_3-groups. The quality of the final coating depends on the preparation conditions and the used silane chain length [Brz1994, Han2008]. Accordingly, OTS prepared at room temperature should result in an optimal packing density of chains [Gru2007].

Coated silicon wafers are stored under clean room conditions (class 100) and are easy to clean in an ultra-sonic bath, due to their mechanical robustness [Din2006]. Before further usage, the individual wafer samples are usually cleaned in ultra-sonic baths of ethanol (absolute, reag. ISO, reag. Ph. Eur., ≥99.8% (GC), Sigma-Aldrich Chemie GmbH, Munich, Germany), acetone (analytical reagent grade, Fisher Scientific UK Ltd. Loughborough, UK) and toluene (for liquid chromatography LiChrosolv®, Merck KGaA, Darmstadt, Germany), each time for 3–5 min. With a thermal stability up to 250 °C these coatings are suitable for the complete temperature range of experiments in this work [Hel2002, Sri1998].

A detailed recipe for the preparation of silane coatings has been published by our group and was applied for all silane coatings of this thesis [Les2015]. The structural analysis of these coatings by AFM and XRR is part of this thesis and is described in detail in Chapter 5.

4.3.2 Teflon-like coatings: PTFE AF1600 & AF2400

Silanes form a highly hydrophobic surface. Teflon-like coatings can render a surface also strongly hydrophobic, yet in contrast to silanized surfaces, where crystalline structures may exist, they are amorphous.

As an amorphous substrate, a special kind of polytetrafluoroethylene (PTFE), named AF2400 (Poly [4,5-difluoro-2,2-bis(trifluoromethyl)-1,3-dioxole-co- tetrafluoroethylene]- dioxole 87 mol %, see Fig. 4.5), is used. The higher concentration compared to the formerly used AF1600 [Bäu2010b] with 65 mol %, leads to a higher thermal stability. The name refers to the glass transition temperature: AF2400 exhibits a T_g of 240 °C. This switch was necessary, because PMMA has a higher glass transition temperature than PS, so experiments are also performed in the vicinity of 160 °C. Chapter 5 will show that AF2400 and AF1600 are comparable in terms of their surface properties.

AF2400 is either dip- or spin coated onto a silicon wafer (see Sec. 5.1.2). Dip coating has the advantage of forming PTFE films without wrinkles and waves. To evaporate residues, the coated sample is annealed for 5–10 min to 66 °C which is 10 K above the boiling point of the used solvent (FC-72, ABCR GmbH & Co. KG). After that, it is annealed to 245 °C for about 5 min to give the film the chance to relax. Eventually, the samples are ready to use.

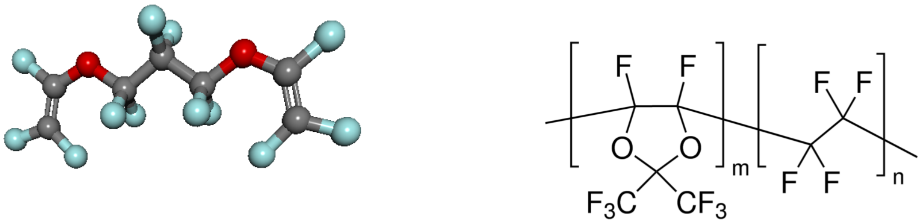

Figure 4.5: Ball and stick model [Hil2010, Mol2006] of PTFE AF. Chemical structure according to Sigma-Aldrich's data sheets [Sig2016a].

In contrast to silanes, AF2400 is sensitive against scratches and can not be cleaned mechanically (e.g. by wiping it with a cloth immersed in ethanol or toluene) or in an ultra-sonic bath, so the samples should not be stored too long before further use.

5 A Detailed Look at the Coatings

A detailed information of the substrate is the first and most important condition to get insights to the liquid's conformation at the interface to the substrate. The silane coatings used in this work have a long tradition as model surfaces [McG2016, Häh2012, Los2012b, Bäu2010b, Bel2008, Fla2007, Mez2006, Dos2005, Fet2005, Hub2005, Her1998]. Besides the standard characterization in terms of water contact angle, surface energy and roughness, this chapter will present the results of detailed X-ray reflectometry results and molecular dynamic simulations to reveal the conformation of the self-assembled monolayers. Moreover AF2400 is characterized to check whether it has the same surface characteristics as AF1600. This ensures the compatibility with experiments of former studies.

As described in Chapter 4, all silane surfaces used are prepared following the silanization procedure recently published by our group [Les2015]. This recipe leads to reproducible silane surface characteristics with very low roughness and high hydrophobicity.

AF2400 is prepared by dip coating a silicon wafer with a defined velocity in a solution. Thus, the film thickness can be tuned as needed. The resulting films are characterized concerning their hydrophobicity, roughness, and curvature.

5.1 Topography and Roughness

To quantify roughness this work, the root-mean-square roughness (RMS)

$$R_\mathrm{q} = \sqrt{\frac{1}{MN}\sum_{m=1}^{M}\sum_{n=1}^{N}(z(x_m, y_n) - \langle z \rangle)^2} \tag{5.1}$$

of AFM pictures with a size of 1 $\mu\mathrm{m}^2$ is used. Absolute values of the RMS roughness are not comparable to roughness values measured by XRR (see Sec. 5.3). Apart from the method of measurement, XRR roughness is related to the footprint of the X-ray beam, which is usually in the range of square microns or even square millimeters (see Sec. 3.4).

5.1.1 Silane Coatings

To give a basic impression of the silane coatings, Figure 5.1 shows 1 $\mu\mathrm{m}^2$ images captured by AFM in *TappingMode*^{TM}. Figure 5.1 upper row shows two silicon wafer samples coated with OTS (a) and DTS (b). Both SAMs are dense, homogeneous and without observable defects. Scratches across the image arise from the wafer's polishing process at the manufacturer. The fact that these scratches are still visible after silanization is a first indication that the silane layer reproduces almost the roughness of the underlying silicon [Les2015]. Usually OTS shows a slightly lower roughness than DTS (see Tab. 5.1). This could be a result of preparing DTS at room temperature, which is not optimal [Brz1994].

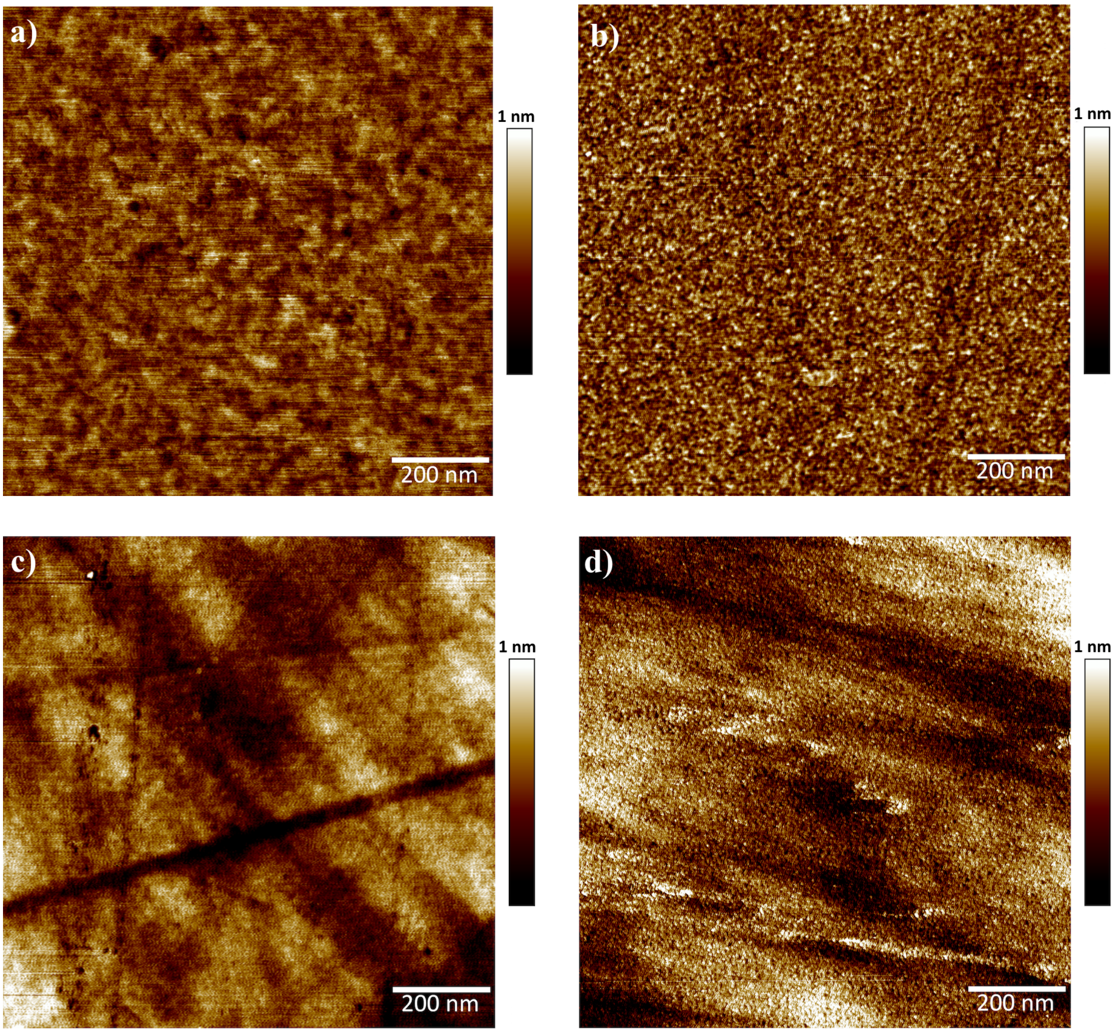

Figure 5.1: Roughness of OTS- and DTS-coated silicon (upper row) and quartz (lower row) wafers, captured by AFM. **a)** OTS on silicon; $R_\mathrm{q} = 0.11(1)\,\mathrm{nm}$, **b)** DTS on silicon; $R_\mathrm{q} = 0.30(3)\,\mathrm{nm}$, **c)** OTS on quartz (OTSQ); $R_\mathrm{q} = 0.18(1)\,\mathrm{nm}$, **d)** DTS on quartz (DTSQ); $R_\mathrm{q} = 0.23(3)\,\mathrm{nm}$

Figure 5.1 lower row shows the silanized quartz wafers. In the following coatings prepared on quartz are named with an additional Q to the silane abbreviation (OTSQ and DTSQ). Compared to silicon supported coatings (see Fig. 5.1 upper row) more scratches from the polishing are observable as well as a small waviness in lateral direction. However, the final coating shows a slightly increased, but comparable RMS roughness.

5.1.2 AF2400

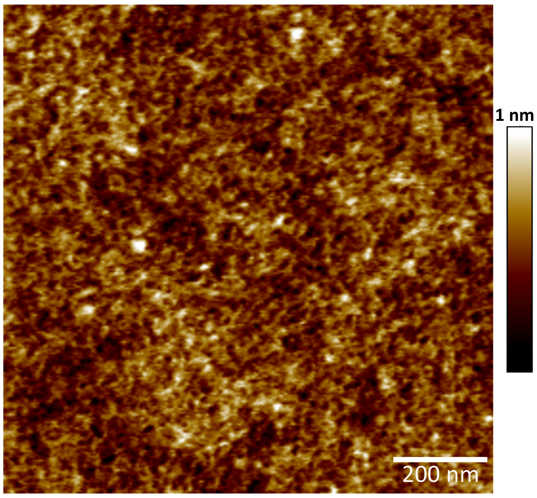

Figure 5.2: Roughness of an approx. 15 nm thick AF2400 film, dip coated on a silicon wafer, captured by AFM.

In former studies of our group [Bäu2014, Bäu2010c, Bäu2009a], PS was prepared on AF1600, which is thermally stable up to 160 °C. During this work, AF2400 was used because of its higher thermal stability, while all other surface parameters should remain comparable.

AF2400 is dip coated onto a piranha-cleaned (1:1 H_2SO_4:H_2O_2) silicon wafer. The cleaning steps are identical to those prior to the silanization [Les2015]. The dip coating takes place at a speed of 1 mm/s into a 0.6% solution of AF2400 in FC-72 (C_6F_{14}, ABCR GmbH & Co. KG) which results in an about 15 nm thick Teflon^{TM} film (see Fig. 5.2). The layer thickness was determined by ellipsometry, as well as by AFM (measuring the depth of a scratch in the Teflon coating).

A dip coated AF film exhibits no wrinkles on the lateral scale compared to a spin coated film (see Fig. 11 in Ref. [Bäu2010c] and Fig. 7.11 in this work). The RMS roughness determined by AFM is in the range of 0.49(2) nm. This is slightly higher than the roughness of the silane surfaces, but suitable for dewetting experiments without the risk of increased pinning effects, taken the fact that the radius of gyration of a PS chain is in the range of some tens of nanometers (see Sec. 4.1.1).

The dip coating reduces the waviness of the substrate on the micron scale and results in a lower RMS roughness, but unfortunately the coating is not planar over the whole

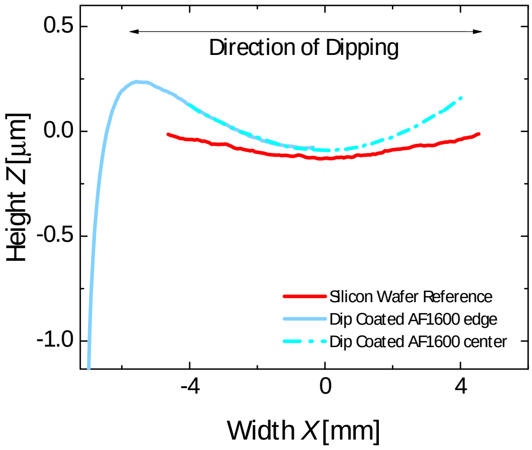

Figure 5.3: Cross section of an approx. 15 nm thick PTFE AF film, dip coated on a silicon wafer (blue), captured by WLI. Two separate scans of the sample's center and edge are stitched together. The red line shows an uncoated silicon wafer as a reference. Red and blue data are artificially shifted for better visibility and to match the sample's center.

sample. This is a consequence of the actual dipping process. The wafer sample is dipped vertically into the AF2400 solution. A meniscus develops at the edge of the sample, as soon as it touches the liquid. When the sample is pulled up again and leaves the liquid, another meniscus forms and the solution left on the wafer dries [Bri1990]. Figure 5.3 shows cross-sections of White-Light-Interferometry (WLI) pictures[1] of a 15 nm thick AF film dip coated on a silicon wafer and an uncoated silicon wafer as a reference. The surface coating exhibits a noticeably increased curvature of about 0.25 µm peak-to-valley (related to the measured range of 8 mm) compared to less than 0.15 µm of the silicon wafer reference it is prepared on. The curvature results in problems during X-ray reflectometry (details on that in Sec. 5.3.4).

5.2 Contact Angles & Surface Energy

In a situation where a droplet sits on a solid surface (see Fig. 5.4), three tensions are competing: solid-liquid (γ_{sl}), liquid-vapor (γ_{lv}) and solid-vapor (γ_{sv}). Their balance results in the formation of Young's contact angle θ_{Y} [You1805]:

$$\cos\theta_{\mathrm{Y}} = \frac{\gamma_{\mathrm{sv}} - \gamma_{\mathrm{sl}}}{\gamma_{\mathrm{lv}}}. \tag{5.2}$$

---

[1] WLI measurements were done with the help of Michael Hans at the group of Prof. Dr.-Ing. Frank Mücklich, Saarland University.

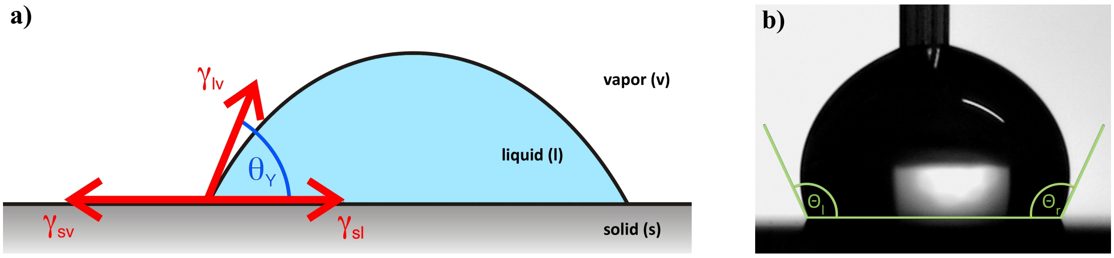

Figure 5.4: a) Schematic of a sessile droplet on a surface. The effective surface tensions γ_{lv}, γ_{sv}, and γ_{ls} lead to the Young's contact angle θ_{Y}. **b)** Typical snapshot of a droplet to measure left- and right-sided contact angles.

If $\gamma_{\mathrm{sl}} + \gamma_{\mathrm{lv}} \leq \gamma_{\mathrm{sv}}$, the liquid wets the substrate completely, $\theta_{\mathrm{Y}} = 0°$. In the opposite case, if $\gamma_{\mathrm{sv}} + \gamma_{\mathrm{lv}} \leq \gamma_{\mathrm{sl}}$ the liquid drips off from the substrate and the contact angle reaches its maximum value of 180°.

Contact angles can be measured statically and dynamically (see Sec. 3.2). The difference between advancing and receding contact angle gives the contact angle hysteresis, which is a sensitive indication for the surface quality: a low hysteresis ($< 15°$) is a characteristics for a smooth and chemical homogeneous surface [Cas1944, Wen1936].

Advancing water contact angles on OTS and DTS are well above 100° and – if prepared on silicon – feature a very low hysteresis of less than 10°. Contact angles on quartz are some degrees lower and the hysteresis is 4° higher in the case of OTSQ, and 11° higher in the case of DTSQ, as their respective counterpart on silicon. On AF2400, water exhibits a contact angle of 123(3)° with a hysteresis of 14(2)° (see Tab. 5.1). All measurements are performed with fresh ultra-pure water using the sessile drop method (see Sec. 3.2).

To compute the surface energy γ_{sv} given in Table 5.1 the Good-Girifalco equation [Goo1960] is combined with Young's equation for the equilibrium contact angle θ_{Y}

$$\gamma_{\mathrm{sv}} = \frac{\gamma_{\mathrm{lv}}}{4}(1 + \cos\theta_{\mathrm{Y}})^2. \tag{5.3}$$

Table 5.1 lists the surface energy determined by apolar liquids. As γ_{lv}, tabulated values for 1-bromonaphtalene (>95%, Fluka, $\gamma_{\mathrm{lv}} = 44.6\,\mathrm{mN/m}$) and bicyclohexyl (99%, Acros Organcis, $\gamma_{\mathrm{lv}} = 32.8\,\mathrm{mN/m}$) are combined with the averaged advancing and receding contact angles. The contact angles are in the range of 60° for bromonapthalene and 35° for bicyclohexyl. All silane-coated surfaces show comparable surface energies, whereas AF2400 has a significantly lower value, which corresponds to AF1600 of former studies [Bäu2008].

The spreading parameter (Eq. 2.8) that drives the dewetting depends on the contact angle of the liquid, therefore Table 5.1 also lists the contact angles for the applied

	Contact Angle $\theta(H_2O)_{adv}$ [°]	Hysteres. $\Delta\theta(H_2O)$ [°]	Roughness (RMS) R_q [nm]	Surface Energy γ_{sv} [mN/m]	Cont. Angle		
					θ(PS) [°]	θ(PMMA) [°]	θ(PVP) [°]
OTS*	110(1)	10(1)	0.11(1)	25.5(9)	63(1)	60(2)	59(2)
OTSQ	101(2)	14(2)	0.18(6)	24.3(5)	63(2)		
DTS*	108(2)	9(2)	0.30(3)	26.4(9)	52(3)	64(1)	60(2)
DTSQ	106(2)	18(2)	0.23(3)	25.8(8)	68(6)		
AF2400	123(2)	14(2)	0.49(2)	17.2(9)	66(2)	55(5)	60(5)

Table 5.1: Summary of surface characteristics of the used coatings ($\star$ Data for OTS and DTS were acquired during the supervision of N. Ackermann's Staatsexamensarbeit [Ack2013]).

polymer melts on the respective surface. To capture this data, a polymer film is annealed until it has completed its dewetting processes (see Fig. 7.2). The remaining droplets are quenched to room temperature which conserves their shape in a glassy state. Then droplets in the range of 3 to 10 microns in diameter are measured by AFM. The AFM operates in TappingMode^{TM} to minimize the risk of pushing or damaging the droplets (see Sec. 3.3). From each drop, different AFM cross-sections through the center are extracted. Values given in Table 5.1 represent mean values of the left and right contact angle, different lines and several droplets for each system. The detailed methods on how to actually measure the contact angle were developed during the supervision of N. Ackermann's Staatsexamensarbeit [Ack2013].

5.3 Structural Characterization

All data presented so far show superficial characteristics of the self-assembled monolayers. The following paragraphs will give more insight on the molecular composition and structure. This chapter pursues two different approaches: on the experimental side, the samples are characterized using X-ray reflectometry. The models derived from these measurements are the starting point for detailed molecular dynamics simulations on the theoretical side.[2]

---

[2] The simulations were carried out by Juan-Manuel Sanchez at the TU Kaiserslautern.

5.3.1 XRR Data Evaluation - Basic Principles

The following is only a very brief introduction to the basic principle of X-Ray reflectometry. More details can be found in the books of Metin Tolan [Tol1999] and Jean Daillant and Alain Gibaud [Dai2008].

XRR captures the specular reflectivity R as a function of the scattering vector

$$q_{\mathrm{z}} = \frac{4\pi}{\lambda} \sin\theta, \tag{5.4}$$

where θ is the angle of incidence. The construction of an electron density ρ_{el} profile (EDP) leads to a modeled reflectivity. To get the best fit to the measured data, the free parameters are varied within the effective density model [Tol1999]. In this model, the electron density consists of boxes. Each box is defined by its electron density ρ_{el}, thickness d and roughness σ. In contrast to a standard box model, the effective density model allows the boxes to overlap which ensures a smooth profile. Furthermore, the model is also valid for layered systems, where the roughness of the layers is not negligible compared to the thickness ($\sigma_i + \sigma_{i+1} \lesssim d_i$), which is often the case for very thin layers.

The obtained EDP is divided into slices of 1 Å which are used to calculate the reflectivity curve with Parrat's formalism [Par1954]. This is done until a least-square fitting algorithm leads to the best fit, and thus to the best model that describes the measured reflectivity.

Knowing that the EDP is a result of a fitting algorithm with a number of free parameters, one has to keep in mind that the EDP is not a definitive description of the sample, respectively its molecular composition. At this point, MD simulations come into play, that help to refine the molecular picture and the scope of the fitting parameters (see Sec. 5.3.3).

5.3.2 XRR Characterization of Coated Silicon

The characteristics of the supporting silicon wafer are well known at the date of purchase: The surface of the single-crystal wafer consists of an amorphous silicon oxide layer with a thickness of about 1.7 nm (measured by ellipsometry). So the binding and the formation of the SAM on top of it, have some degree of uncertainty (see Chap. 4.2). By comparing the layer thickness of the SAM with the length of a single silane molecule, one can already gain an impression of the arrangement. In an all-trans configuration, the height of the thickness of the silane layer should match the length of the elongated molecule.

For the analysis of silicon wafer based samples, beamline BL9 at DELTA synchrotron in Dortmund served as X-ray radiation source (see Chap. 3.4). Where not otherwise indicated, the beam energy was 13 keV, which corresponds to a photon wavelength of $\lambda = 0.95$ Å. Figure 5.5 depicts the specular reflectivities $R(q_{\mathrm{z}})$ of DTS- and OTS-coated silicon wafers. Figure 5.6 includes the corresponding constructed electron density profile

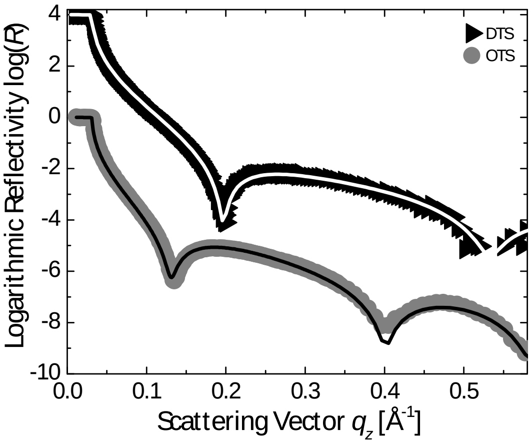

Figure 5.5: Reflectivity of DTS- (dark triangles) and OTS-coated (light circles) silicon wafers, captured at DELTA BL9 (Dortmund). Solid lines represent fits to the data. DTS data points are shifted for better visibility [McG].

(EDP). The EDP is built out of 4 layers that correspond to the bulk silicon, the silicon oxide layer, the head and the tail of the silane chain. For each layer, Table 5.2 lists the thickness d, electron density ρ_e and roughness σ. The substrate is to be considered as infinitely thick.

The head of the silane is a single silicon molecule that is covalently bound to a silicon atom of the substrate via an oxygen molecule. This chemical identity makes it difficult to distinguish the interface between head layer and silicon oxide layer. To get a good fit of the head layer's height, the known thickness of the oxide layer is used as reference. The head layer itself has a thickness in the range of 5–6 Å, with a slightly lower electron density than the silicon oxide layer – a first hint, that the head groups are closely packed. However, due to possible cross-binding between the head groups, this is not a reliable indicator for the density of chains per surface area. Steinrück et al. [Ste2015] recently published suggestions on how to include structures in the lower parts of the SAM into the fitting procedure of XRR data. This gets important for very neatly scans at a wide range of q_z. Steinrück et al. measured to values of $q_\mathrm{z} > 1$, whereas the presented data in this theses is at values of $q_\mathrm{z} < 0.7$, where none of these assumptions are needed to fit the data sufficiently and extract reliable informations of the tail layer.

The electron density of the tail group can be used to get insight into the packing density of the chains. The tail layer is very clearly detectable in the EDP. In the case of OTS it has a remarkably sharp interface towards the adjacent layers. Even in the case of DTS, where the roughnesses are slightly higher, it gives a clear picture. The OTS tail has an electron density of 0.351(1) Å^{-3} which corresponds to about 4–5 chains/nm^2, if they are assumed as an upright standing rigid chain, so that the tail layer can be seen as a homogeneous box with the dimensions electron density and layer width. Divided by the number of electrons in the tail (145 for OTS and 97 for DTS), this leads to

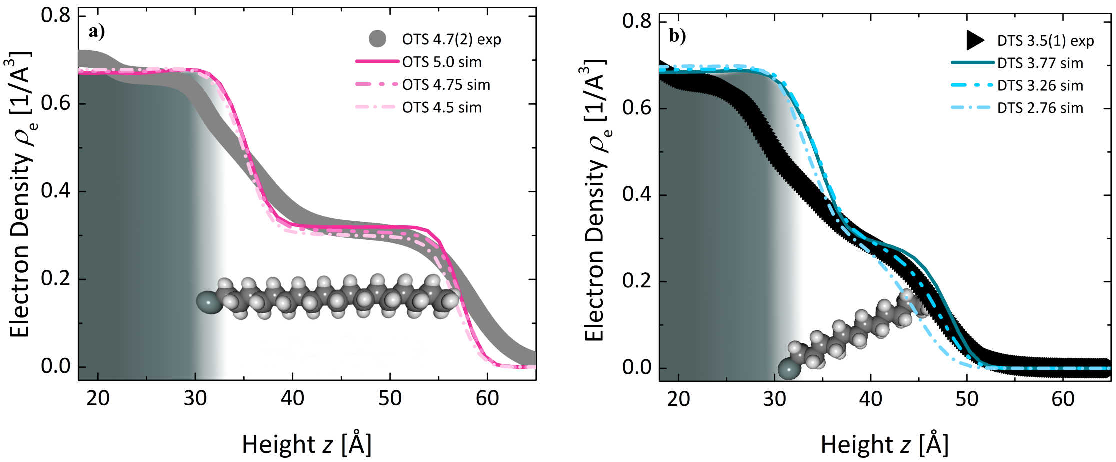

Figure 5.6: Electron density of silane coated silicon substrates obtained by XRR, in comparison to the electron density extracted from MD simulations [Cas2015]. The sketches of the gray fading plane an the silane molecule in the background represent a guide to the eye, to distinguish the respective layers in the EDP. From left to right: silicon, silicon oxide, head group layer, tail layer. **a)** Symbols: Typical EDP for OTS on silicon, constructed from XRR measurements. Lines: Simulated data for three different chain densities. **b)** Symbols: Typical EDP for DTS on silicon, constructed from XRR [McG]. Lines: Simulated data for three different chain densities.

the experimental chain densities (coverages) given in Figure 5.6. With this assumption, DTS with $\rho_e = 0.292(2)\,\text{Å}^{-3}$ would correspond to about 3–4 chains/nm^2. In the case of OTS this density is comparable to almost 100% crystalline density, and approximately 90% for DTS [Gut2013, Tid1990]. This is also in agreement with MD simulations (see Chap. 5.3.3 and Refs. [Ewe2012, Cas2015]).

By comparing the height of the tail layer with the theoretical length of the hydrocarbon chain, the tilt angle of the molecules can be estimated, if they are assumed as stiff, straight sticks. According to the performed simulations, the tail has a length of 2.25 nm for OTS and 1.49 nm for DTS [Cas2015]. The comparison with experimentally determined tail layer thicknesses leads to tilt angles below 20° for OTS and between 30° and 40° for DTS (relative to the surface normal, see inset of Fig. 5.8). The values are given as a range because this calculation is very sensitive to small variations of the measured layer height which has an intrinsic uncertainty. Also the assumption of stiff, non-bent sticks is not realistic, and the scatter between different samples and measurements is high. The recent silanization recipe and characterization publication of our group considers average values of several experiments [Les2015].

The roughness of OTS and DTS towards the air interface is comparable, although DTS is slightly rougher, a trend that is also observed by AFM (see Tab. 5.1).

Overall, XRR shows that – judging from the electron density of the tail layer – both, OTS and DTS are densely packed, with OTS being almost crystalline. A very simple view of the connection between layer height and molecule length tells that OTS molecules stand almost upright in the SAM. The very low roughness towards the air interface is a result of this remarkable assembly. DTS is less ordered, the packing density of the chains is lower and it has a higher roughness. This indicates a larger volume per chain and with that the freedom of more tilt.

5.3.3 Comparison of Measured and Simulated SAMs on Silicon

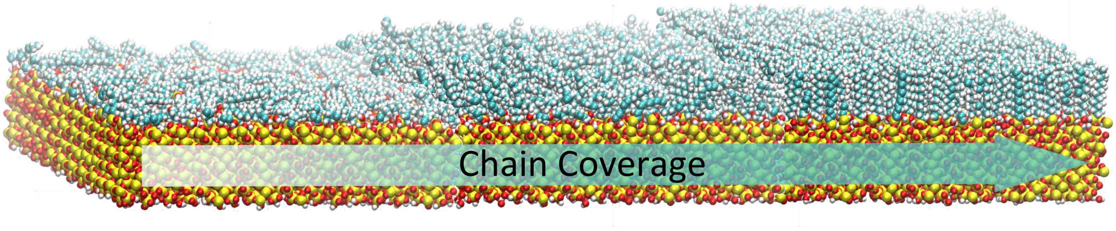

Figure 5.7: Simulated DTS layer with three different chain densities (1.0 chains/nm^2, 2.5 chains/nm^2 and 4.5 chains/nm^2) on top of a β-cristobalite (101) substrate. Silicon atoms are depicted yellow, oxygen red, carbon blue and hydrogen white. Figure modified based on Castillo et al. [Cas2015].

As indicated in Chapter 5.3.2, the construction of an EDP out of XRR data relies on some assumptions and a certain knowledge of the layered system. For example: How many layers are expected? What could be their roughness and thickness? In close cooperation with the group of Hans Hasse at TU Kaiserslautern, MD simulations where performed on the basis of the experiments described in this thesis to refine this conceptual picture. A very detailed description of the simulations as well as a comparison to the experimental situation and data can be found in our collaborative publication [Cas2015]. The comparison presented here will focus on electron density profiles and findings derived from them.

A β-cristobalite (101) substrate substitutes the amorphous silicon oxide. To this substrate, OTS respectively DTS molecules are bound randomly with a predefined density of binding sites. The density is varied between 5.52 nm^{-2}, when all binding sites of the substrate are occupied, down to 1 nm^{-2}, for each kind of silane. Figure 5.7 shows three snapshots of the simulation at different DTS chain densities from 1.0 chains/nm^2 to 4.5 chains/nm^2. The picture series shows that the chains start to straighten up with increasing density, the layer gets thicker and the surface smoother. All this corresponds with the present notion of the SAMs. However, the assumption that the chains are rigid is too simplified. At a very low density, the chains lie flat on the surface. When they are placed closer together, they reduce their overall tilt, as sketched in Figure 5.8a.

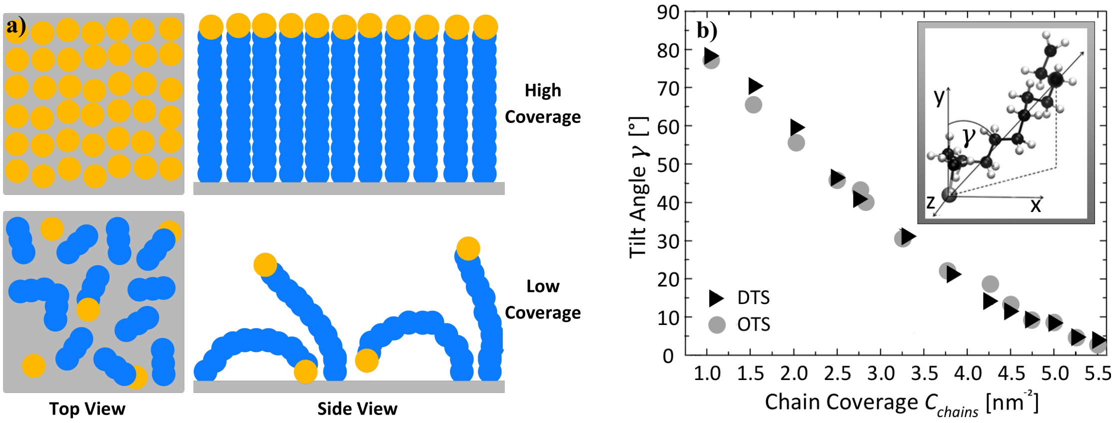

Figure 5.8: Dependency of the tilt angle on the chain coverage. **a)** Sketch of a very densely packed SAM (upper row) and a SAM with a low chain coverage (lower row). Yellow circles represent CH_3 groups, blue circles CH_2 groups. **b)** Tilt angle averaged over all chains and times as a function of coverage. Figure modified based on Castillo et al. [Cas2015].

The simulation snapshots clearly show that the chains are not rigid but bent, so the tilt angle measured from head towards every single molecule in the backbone is different [Cas2015]. With less space available for the individual chain, their curvature is reduced. This implicates that the highly ordered, densely packed surface consists mostly of the silane's tail CH_3 end-groups, whereas in less ordered systems, also hydrogen side-groups form parts of the surface (see Fig. 5.8a).

In Section 5.3.2, a very basic approach to calculate the tilt angle was introduced. In the MD simulations, it is possible to actually measure the angle between individual atoms. Figure 5.8b shows the tilt angle γ based on the chain's center of mass, averaged (see inset of Fig. 5.8b) over all molecules in the system, as a function of the chain coverage C_{chains}. Starting at almost 90° – which means flat lying chains – for a coverage of only 1 chain per nm^2, and ends at 0°, when all binding sites of the β-cristobalite substrate are occupied, at 5.52 chains per nm^2. OTS and DTS show the exact same behavior. The simulations confirm $\theta(\text{DTS}) \approx 30°$ and $\theta(\text{OTS}) \leqq 20°$ for the coverages of OTS and DTS given in Section 5.3.2.

Figure 5.6 shows electron density profiles measured by XRR (see Fig. 5.5) in comparison to profiles extracted from simulations. These profiles are derived from simulations where the chain density is in the range of the experimental values: 3.5(1) nm^{-2} for DTS and 4.7(2) nm^{-2} for OTS.

For both silanes the electron density curves from simulation and experiment match very well, only small deviations at the transition from substrate to the head group of the silane are visible. As already indicated the head group is chemically identical to the substrate, a cross-binding between head groups is not implemented, so the electron density in the simulation stays constant at this part of the EDP.

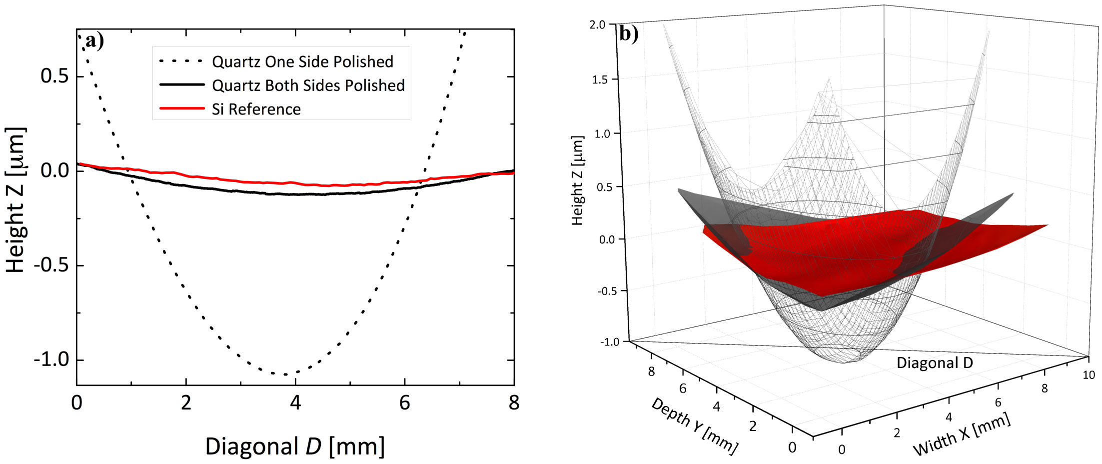

Figure 5.9: Curvature of wafer samples, cut from the center of the respective wafer, captured by WLI. **a)** Cross-section and **b)** 3D representation of a quartz wafer polished at one side (gray dotted and dashed) as received in the first place, and double side polished (gray solid surface) as reworked compared to a silicon wafer reference (red solid).

The electron density of the tail is in remarkable agreement in experiments and simulations: The curves match exactly in layer height, electron density and roughness. With the knowledge of the chain coverage in the simulations by design, it can be concluded that the real OTS and DTS have indeed the supposed coverages of $\approx 5\,\text{nm}^{-2}$, respectively $\approx 3.5\,\text{nm}^{-2}$, along with the above discussed tilt angles. By implication this means, that if actual DTS formed a more dense layer, the SAM would probably have the same structure as known from OTS-SAMs.

5.3.4 XRR Characterization of Coated Quartz

As seen in the previous section, in simulations, the structure can be controlled by a variation of the chain coverage, which is synonymous to the number of occupied binding sites at the substrate. Experimentally, this is not easy to control, since the silanes form the monolayer in a self-organized way. For example, changing the ambient temperature influences the formation and density of the SAM [Brz1994]. Possibly, a temperature slightly above 0 °C allows DTS to form a SAM comparable to the structure and characteristics of OTS prepared at room temperature. This should be tested in a future study. The present work followed a different approach by offering the silanes a substrate with different binding sites than the amorphous SiO_2 of a silicon layer. Often sapphire is used for this purpose (see for example Ref. [Ste2014]).

The handling, quality, and availability of quartz wafers is similar to silicon wafers, but they feature a crystalline structure at their surface, instead of an amorphous structure

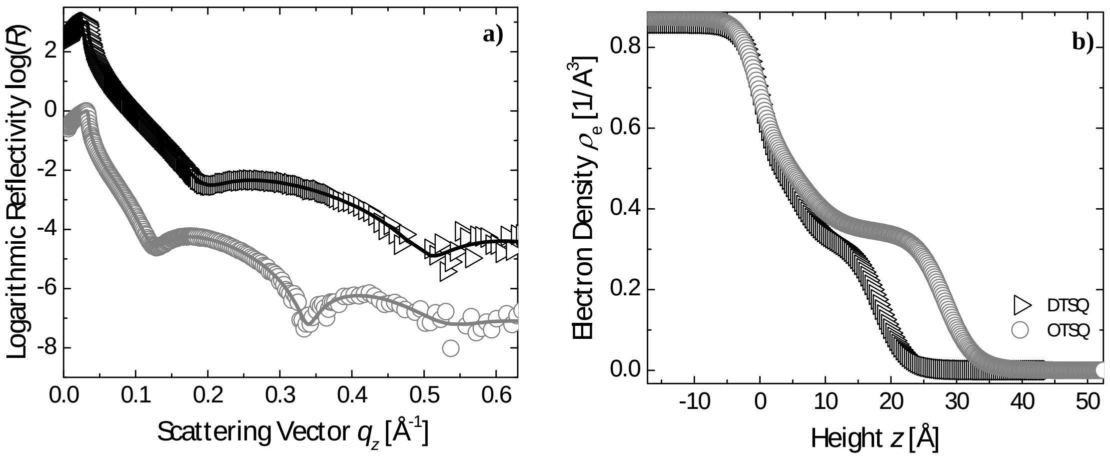

Figure 5.10: Results of XRR study of silanized quartz substrates. **a)** Measured reflectivity data R versus scattering vector q_z (Curves are shifted for better visibility). Solid lines show the best fit to the data. **b)** Calculated electron density from the fits in a). Grey Circles: DTS-coated quartz (DTSQ); Black triangles: OTS-coated quartz (OTSQ).

of SiO_2, as observed on the silicon wafers used here. The growth process of OTS on quartz compared to amorphous SiO_2 was very recently studied by XRR [Ste2012].

At the beginning of the experiments, the quartz wafers (purchased from NQW GmbH, Langenzenn, Germany) showed a pronounced curvature over the complete sample. Figure 5.9 shows White-Light-Interferometry (WLI) pictures[3] of the one-side polished quartz wafers (black dotted and black grid surface), as received, in comparison to a standard silicon wafer (red line and red surface). Over the measured distance of 8 mm the quartz sample shows a curvature, expressed by the peak-to-valley distance, of more than 1.5 µm, whereas the silicon reference shows less than 0.15 µm on the same scale. This circumstance made an alignment of the very angle sensitive XRR setup impossible (see Sec. 3.4).

In cooperation with the manufacturer, the wafers were polished on both sides to reduce internal stresses. The result is also depicted in Figure 5.9 as a gray solid surface and a black solid line. Now the sample features a curvature in the range of the silicon reference. However the curvature in certain directions still exceeds values needed for XRR of high resolution. Because if this, the D8 diffractometer was used instead of BL9. The D8 has a lower angle resolution and is not that sensitive to small surface irregularities.

Figure 5.10 shows the reflectivity curve for OTS and DTS silanized quartz (OTSQ and DTSQ) and the corresponding electron density profiles. To construct the EDP, the formerly used four layer model was reduced to three layers: tail, head and bulk silicon oxide (quartz). The exact values are listed in Table 5.2. The tail group's roughness, electron density and thickness matches its counterpart on amorphous silicon. Furthermore, the

---

[3] WLI measurements are done with the help of Michael Hans at the group of Prof. Dr.-Ing. Frank Mücklich, Saarland University.

		OTSQ	OTS	DTS	DTSQ
Quartz	ρ_e [Å^{-3}]	0.875	-	-	0.858
	σ [Å]	1.82(7)	-	-	2.31(5)
Si	ρ_e [Å^{-3}]	-	0.702	0.702	-
	σ [Å]	-	1.2(3)	1.5(1)	-
SiO_2	d [Å]	-	9.8(1)	9.5(1)	-
	ρ_e [Å^{-3}]	-	0.654(1)	0.664(1)	-
	σ [Å]	-	1.58(20)	2.73(5)	-
Head	d [Å]	6.6(4)	5.46(5)	6.22(5)	6.2(4)
	ρ_e [Å^{-3}]	0.558(30)	0.558(10)	0.460(1)	0.509(20)
	σ [Å]	5.1(5)	4.10(9)	3.90(8)	3.3(5)
Tail	d [Å]	21.6(3)	21.68(3)	11.85(4)	12.0(4)
	ρ_e [Å^{-3}]	0.343(20)	0.312(10)	0.292(2)	0.325(10)
	σ [Å]	4.0(4)	4.07(9)	4.23(9)	3.7(4)

Table 5.2: Parameters of the models used shown in Figure 5.5, Figure 5.6, and Figure 5.10. ρ_e, d and σ corresponds to the electron density, thickness of the layer and roughness [McG].

smooth surface roughness determined by AFM (see Tab. 5.1) is supported. By considering the number of electrons in an OTS or DTS molecule and the total integrated electron density, the chain coverage can be estimated to 5.1(4) nm^{-2} for OTSQ and 4.0(3) nm^{-2} for DTSQ. Roughness and thickness of the head groups are comparable to values on standard silicon. It has to be mentioned that the electron density of the DTSQ head layer is more comparable to OTS and OTSQ than to DTS. The reason for that could be difficulties of the fitting method distinguishing the head from the chemical identical substrate (see increased roughness value of the quartz substrate in the fit of DTSQ). Nevertheless, it could also be a characteristic of a more dense packing of the SAM. All measurements were performed with a Bruker AXS D8 diffractometer with the help of Michael Paulus at TU Dortmund.

5.4 Summary

All used coatings, silane and PTFE AF, result in very smooth (RMS $R_q < 0.5$ nm) and highly hydrophobic surfaces ($\theta(H_2O)_{adv} > 101°$). Water contact angle hysteresis for silanes on standard silicons are in the range of 10° or below, silanes SAMs on quartz show a slightly higher hysteresis. Surface energies for silane coatings are in the range of 25 mN/m, AF2400 features about 17 mN/m. Overall, for the determined parameters (roughnesses, contact angles and surface energies) AF2400 shows the same characteristics as the formerly used AF1600. By dip coating AF2400 instead of spin coating it, the waviness of the coating was reduced. Unfortunately, the surface is not planar enough to be suitable for XRR. The XRR characterization of the silanized quartz wafers show that the SAMs are basically comparable to SAMs prepared on amorphous silicon. The calculated chain densities of 4.0(3) nm^{-2} for DTSQ and 5.1(4) nm^{-2} for OTSQ are comparable to the values given in Section 5.3.3 for SAMs on silicon wafers with an amorphous silicon oxide layer (3.5(1) nm^{-2} and 4.7(2) nm^{-2}). In general, OTS forms SAMs with a coverage of about 4–5 chains per nm^2 whereas the density of a DTS-SAM is about 3-4 chains per nm^2. The noisy landscape seen by AFM (see Fig. 5.1a and Fig. 5.1b) leaves no measurable footprint in XRR or is not resolvable with the used setup.

6 Quartz and PS

As seen in Chapter 5, the silanization of quartz and silicon results in slightly different SAMs, which is also expected in simulations where the lattice of the bonding sites was varied [Zha1995]. AFM scans of OTS and DTS prepared on quartz show a more noisy and stepped landscape as if prepared on standard silicon wafers. Also the higher water contact angle hysteresis of 14(2)° for OTSQ, respectively 18(2)° for DTSQ, hint to a more inhomogeneous surface as compared to amorphous silicon substrates.

The hypothesis is that on the quartz surface, the silanization leads to a different morphology of the packing of the silanes inside the SAMs that either enhances or suppresses slip as compared for silanization onto silicon wafers. To enable a very precise comparison, the very same polystyrene is prepared under identical conditions on all four substrates: OTS-coated on standard silicon and quartz wafers (OTS, OTSQ), and DTS on standard silicon and quartz (DTS, DTSQ). The experiments take place at 110 °C, which is in the middle of the already studied temperature range of PS13k [Fet2007b].

6.1 Experimental Details

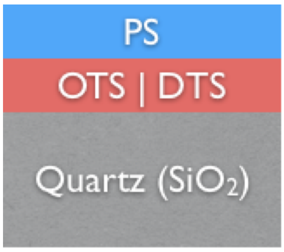

Figure 6.1: Schematic of the prepared dewetting system: A polystyrene film floated on a silanized quartz wafer.

Single crystalline quartz wafers (see Sec. 4.2.2) and standard silicon wafers with an amorphous silicon oxide layer (see Sec. 4.2.1), are silanized with OTS or DTS through a wet chemical process [Les2015]. As detailed in Section 5.3.4 the resulting OTSQ- and DTSQ-SAMs show surface energies and roughnesses that are comparable to OTS and DTS (see Chap. 5). XRR analysis reveals that the DTSQ-SAM is less ordered than the OTSQ-SAMs, as also seen for DTS and OTS. For the values acquired, DTSQ and OTSQ are slightly more densely packed as the respective silane SAM on amorphous silicon. The

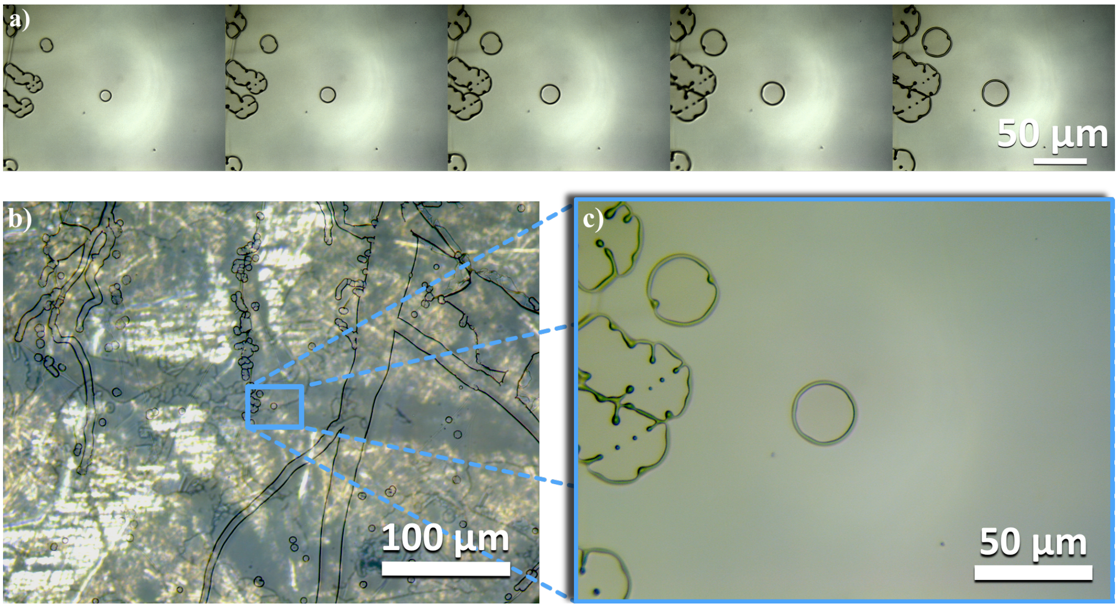

Figure 6.2: Optical micrographs of a 128(5) nm thick PS12k film dewetting from an OTS-coated quartz (OTSQ) at 110 °C. **a)** Time series of a growing hole. Time between snapshots is 20 min. **b)** Overview picture at lower zoom: Straight dewetting fronts and hole rims develop across the sample. The wafer is translucent, so the polymer film appears colorless and the heat stage is visible in the background. **c)** Zoom to the center of the left picture. The hole has reached a radius of 12 µm.

differences observable in water contact angle and contact angle hysteresis (see Tab. 5.1), as well as in AFM overview scans (see Fig. 5.1), indicate a slightly decreased homogeneity for SAMs on quartz as compared to standard silicon wafer substrates.

On top of the hydrophobic self-assembled monolayer (SAM) a 128(5) nm thick 12.5 kg/mol polystyrene (PS12k) film is prepared (see Fig. 6.1) by spin coating a 30 mg/ml solution polystyrene in toluene onto a freshly cleaved mica sheet, at 2500 min^{-1}.

6.2 Results

When heated above its glass transition temperature ($\approx 95\,^\circ$C, see Tab. 4.1), holes nucleate across the sample and the film starts to retract from the hydrophobic substrate. The growth of one representative hole is captured by optical microscopy, as seen in Figure 6.2a.

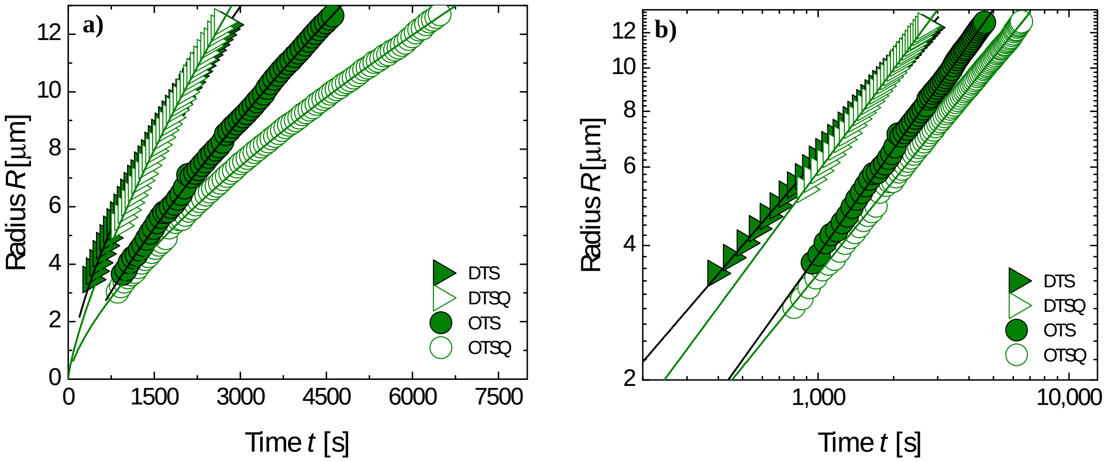

Figure 6.3: Radius of growing holes in 110 nm thick PS12k films as function of time on OTS-coated quartz (OTSQ, open circles), OTS-coated silicon (OTS, filled circles), DTS-coated silicon (DTS, filled triangles), and DTS-coated quartz (DTSQ, open triangles) at 110 °C (For better visibility only every second data point is drawn). Lines represent best fits to the date with respective exponent α: $\alpha_{\mathrm{OTSQ}} = 0.6929(1)$, $\alpha_{\mathrm{OTS}} = 0.761(1)$, $\alpha_{\mathrm{DTS}} = 0.784(1)$, and $\alpha_{\mathrm{DTSQ}} = 0.656(1)$.

6.2.1 Dewetting Dynamics

From a picture series – as depicted in reduced density in Figure 6.2 – the hole's radius R is recorded as a function of time (see Fig. 6.3). With the help of Equation 2.10 it is possible to extract the slip length already from the hole growth dynamics [Fet2007a], but this method is not as accurate as the rim profile analysis [Fet2007b, Bäu2009b]. The hole growth data and fit values of exponent α (see Fig. 6.3) are only shown as additional information and will not be further evaluated. They are in the range of 0.656(1) for DTSQ to 0.784(1) for DTS. Slip lengths are calculated using the rim profile analysis (see Sec. 2.4.2), as described in the following.

Obviously, a hole grows faster on a DTS surface, than on an OTS one and it makes almost no difference whether the SAM is prepared on silicon or on quartz. The dynamics in Figure 6.3 show that the dewetting of PS on both DTS and DTSQ is faster than on OTS and OTSQ. The overall trend and distance between OTS and DTS, respectively OTSQ and DTSQ is maintained. The fitting values of α indicate a slightly higher slip regime on quartz-supported SAMs. Since the values are very close together they should not be interpreted without considering the rim profile analysis.

6.2.2 Rim Profile Analysis

Figure 6.4a shows the corresponding rim profiles to the holes of which the dynamics are shown in Figure 6.3. Rim profiles are captured by AFM and normalized to the film

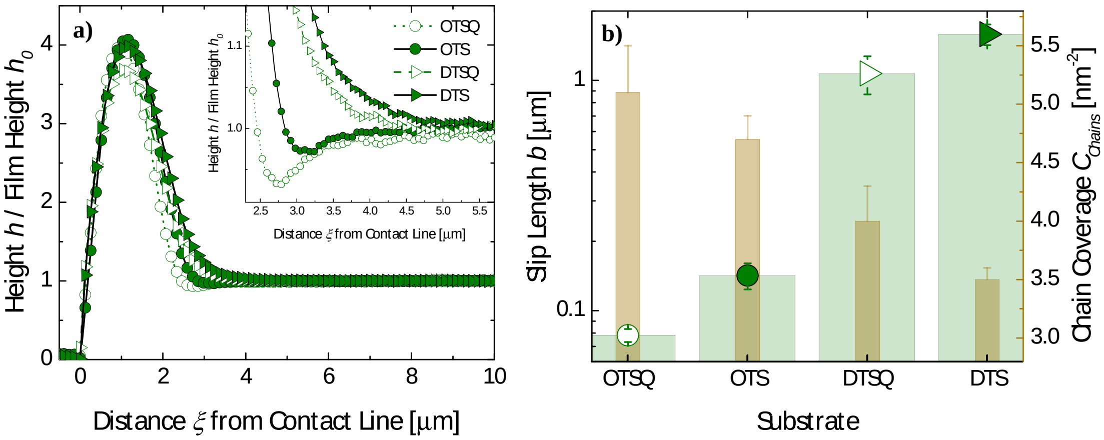

Figure 6.4: a) AFM captured rim profiles of holes with a radius of 12 µm in PS12k films at 110 °C on OTSQ (open circle), OTS (filled circle), DTSQ (open triangles), and DTS (filled triangles). The prepared film thickness $h_0 = 128(5)$ nm. Curves are normalized to the height of the undisturbed film h_0 and the three phase contact line is shifted to 0. **b)** Averaged slip length for PS12k on OTSQ, OTS, DTSQ, and DTS, as acquired by rim profile analyses of several holes and samples (green symbols and green bars as guides to the eye). Error bars represent the error of the mean. Brown bars: Chain coverages of the self-assembled monolayers as discussed in Section 5.3. Error bars represent the standard deviation.

height of the undisturbed film h_0 as well as shifted in ξ direction to overlay all three phase contact points on top of each other. The inset is a zoom into the region of the 'wet' side of the rim in order to show the decay part of the rim that is relevant for the fitting procedure ($h \geq 1.1 \cdot h_0$ and a scope of ξ in which h reaches h_0). All holes have reached a radius of 12 µm.

PS12k shows on both DTS-covered substrates a monotonic decay whereas on the OTS substrates the decay is oscillatory. Furthermore, the minimum on OTSQ is deeper than on OTS and the monotonic shape on DTSQ is not as pronounced as on DTS.

By fitting the profiles with the method introduced in Section 2.4.2, the slip lengths are gained and displayed in Figure 6.4b, for each substrate. The graph combines values of the data in Figure 6.4a with additional holes not shown here, such that the error bars represent the statistical variation on the observation of at least four holes. Additionally, the graph shows the chain coverage for each substrate, as obtained in Section 5.3, indicating that the smallest slip length is measured on the most densely packed SAM and vice versa.

No matter if prepared on amorphous silicon or quartz, PS12k shows a significantly larger slip length on the less ordered silane SAMs ($b \geq 1$ µm for DTS and DTSQ) than on the more ordered SAMs ($b \approx 0.1$ µm for OTS and OTSQ). Overall, the slip lengths on quartz-supported SAMs tend to be slightly lower.

6.3 Discussion & Conclusion

The comparison between quartz and standard silicon-supported SAMs was to show if amorphous or crystalline distributed binding sites for the silanes have an influence on the slip length of PS. Experiments with PS12k on DTS and OTS prepared on standard silicon (with a native silicon oxide layer) resemble the known results by Fetzer et al. [Fet2007b]. This ensured that the prepared SAMs and PS for the current study are comparable with former work and provide a reliable reference.

Neither the raw data for the dynamics nor a detailed evaluation of the slip length based on the analysis of rim profiles reveals a major impact: Yet, quartz-supported SAMs tend to cause smaller slip lengths than silicon-supported SAMs, whereby the reduction to b is the largest for the OTS-SAM on quartz. Slip on DTSQ is one order of magnitude higher than on OTSQ, which is the same for DTS and OTS. These results corroborate the hypothesis that a certain type of order is required for slippage, which is the case for all silane SAMs studied here, yet the best ordered SAM, OTSQ, provokes the smallest slip lengths and on the 'worst' ordered SAM, DTS on standard silicon, the largest slip lengths are achieved.

A future study will show the connection between the degree of order of the SAM and the slip length on the basis of mixed SAMs of OTS and DTS. Indicating that the slip length is higher on mixed SAMs than on uniform SAMs [McG].

7 Influence of the Liquid on the Slip Boundary Condition

As seen in Chapter 6, in dewetting experiments on DTS-SAMs, non-entangled polystyrene (PS) shows slip lengths in the range of more than 1 µm. This is remarkable, since values for the same polymer on OTS drop down to some hundred nanometers. The main reason for this big difference is still unclear. OTS and DTS feature the same wetting properties and are chemically identical.

In general PS shows a higher slip length on structured silane SAMs than on amorphous substrates like AF1600 [Bäu2012a, Bäu2008]. The assumption, that surface energy plays a leading role, was ruled out by using a fluoridated silane with 10 carbon atoms (FDS), which has the same surface energy as AF1600. Results on FDS are comparable to other silanes but not to AF1600 [McG2014]. This leads to the suspicion that the structure of the surface plays a key role.

The structure of silane SAMs is well understood (see Chap. 2 and Chap. 5). As seen in Chapter 6, besides a certain roughness, the substrate has to provide a certain degree of order to induce strong slippage. This work focuses on differences concerning tilt angle and surface coverage with respect to the silane tail. Knowing that the surface coverage for DTS is lower than for OTS, resulting in a higher averaged tilt angle of the molecules, one can summarize that a DTS-SAM is less ordered than an OTS-SAM.

In an earlier study of our group and co-workers [Gut2013], it was tried to link the order of the SAM to the order of the polystyrene film in the vicinity of the solid/liquid interface. The XRR study revealed an interfacial layer between the bulk polystyrene and the underlying silane surface. This layer is thicker on OTS than on DTS. For OTS they state approximately 6 Å, which can be identified with the height of an upright standing phenyl ring, the side group of polystyrene. In the case of DTS, the layer has a thickness of just about 4 Å. A phenyl ring can only fit into this layer if it is tilted by 30°. Both phenyl ring tilt angles in this model match the tilt of the corresponding substrate (see sketch in Figure 7.1). The rest of the chain is assumed as lying flat, which is also seen in simulations on flat/solid surfaces [Lyu2011].

Phenyl rings can stack under certain circumstances, also known as π-π-stacking (e.g. [Nak2014]). The question is, whether a special combination of order-inducing substrate and a polymer that is receptive to this order, leads to strong slip [McG2014]. How could the liquid be influenced by the structure of the substrate? Is a presumed stacking of the phenyl rings more stable and more likely at 30° tilt? This study shall answer these

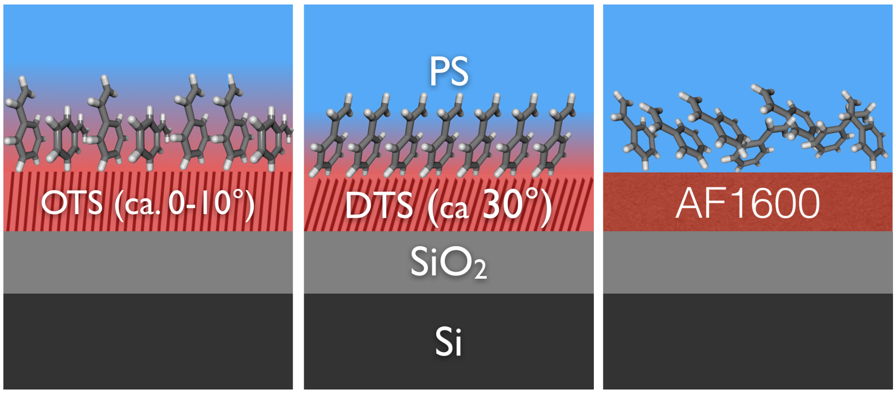

Figure 7.1: Conception of a possible phenyl ring ordering and π-π-stacking of PS side groups at the interface to structured OTS and DTS (as already proposed in [Gut2013]) and amorphous AF1600. For clarity only monomers are drawn and bulk chains are neglected. Sketches of monomers are drawn using BallView 1.4 [Hil2010, Mol2006].

questions by analyzing the slip behavior of polymers provided with differently structured side groups. Films of polystyrene (PS), poly(2-vinyl) pyridine (PVP), and poly(methyl) metacrylate (PMMA) dewetting on differently structured hydrophobic surfaces are compared concerning their slip length. A recent study with PMMA on UV-treated OTS tried to link the wettability of the substrate with the slip length derived from hole growth data [Ohk2014]. The UV-treatment induces an oxidation of the hydrophobic CH_3 groups to hydrophilic COOH groups. They reported that, with increasing time of UV-treatment, the PMMA films become more stable. Unfortunately, the authors did not report any explicit values for the slip length, and since they spin-coated PMMA directly on their substrates, they did not prepare PMMA films on non-treated OTS.

The following study will show – besides the known values for PS – slip lengths for PVP and PMMA on OTS, DTS, and AF2400[1].

7.1 Experimental Details

7.1.1 Substrates

Figure 7.1 depict the experimental systems: A standard (100)-silicon wafer with amorphous silicon oxide layer (≈ 1.7 nm, see Chapter 4.4) is coated with a hydrophobic layer. Either a silane SAM, prepared via a wet chemical process [Les2015] or a 15 nm thin dip-coated Teflon® AF layer (see Sec. 5.1.2) is used. All surfaces feature high hydropho-

---

[1] All data and pictures for PVP and PMMA on DTS and OTS in the following chapter were acquired during the supervision of Sebastian Backes' master's thesis [Bac2013]. Data for PS is included as comparison and in reference to former work of Renate Fetzer [Fet2006a] and Oliver Bäumchen [Bäu2010a].

bicities with water contact angles well above 100° and low surface energies, combined with a very smooth and homogeneous surface quality described by low water contact angle hysteresis $\leq 15^\circ$ and RMS roughnesses below 0.5 nm with respect to an AFM scan of 1 µm x 1 µm (see Tab. 5.1). Silanized wafer are individually cleaned in ultra-sonic baths of ethanol, acetone and toluene before they get covered with a polymer film.

7.1.2 Polymers and Films

On top of the hydrophobic substrates, polymer films with a thickness of about 110(10) nm are prepared from toluene solution via spin coating (PVP $M_\mathrm{w} = 10\,\mathrm{kg/mol}$, 40 mg/ml, $2000\,\mathrm{min}^{-1}$; PMMA $M_\mathrm{w} = 14\,\mathrm{kg/mol}$, 38 mg/ml, $4000\,\mathrm{min}^{-1}$) onto freshly cleaved mica sheets. Afterwards, the films are floated onto an ultra-pure water surface (TKA-genpure, 18.2 MΩ at 25 °C, 6 ppb) from where they can be picked up with the actual substrate.

PVP plasticizes and swells in contact with water [Fel1993]. Depending on how much water invades the film, its glass transition temperature is significantly reduced and the film spreads on water. This makes it impossible to control thickness and homogeneity. Floating on a cooled water surface near 0 °C turned out to suppress the intake of water. PVP films prepared under those conditions showed the same quality as known from PS and PMMA.

The main part of this study focuses on atactic polymers below their critical entanglement length M_c. PVP 10 kg/mol (PVP10k) and PMMA 14 kg/mol (PMMA14k) are compared to PS 13.7 kg/mol (PS13k), see Table 4.1. In Section 7.3, a second set of experiments is described, where entangled PVP and PMMA (PVP56k $M_\mathrm{w} = 56.0\,\mathrm{kg/mol}$ and PMMA57k $M_\mathrm{w} = 57.8\,\mathrm{kg/mol}$, see Table 4.1) are used to test whether or not also in these polymers, slippage can be provoked by long chains. These experiments will be compared to data of PS [Bäu2010b].

The used polymers differ in T_g from 78–96 °C for PVP to 101–110 °C. To keep the timescales of the experiments and the viscosities comparable, the temperature range is chosen relative to T_g.

7.1.3 Experiment

Above their glass transition temperature T_g the prepared films dewet from the hydrophobic substrates. Figure 7.2 shows a picture series of such a dewetting process by the example of a PMMA14k film on OTS.

The process is controlled via a Linkam heater and captured by optical microscopy (see Chap. 3.1 and Fig. 7.2 and Fig. 7.4). When the monitored hole reaches a radius of 12 µm, the dewetting is abruptly stopped by quenching the polymer below T_g. The glassy film, respectively the hole is scanned via AFM (see Chap. 3.3 and Fig. 7.4). From the shape of the hole's rim into the undisturbed film, the slip length can be extracted (see Sec. 7.2.2).

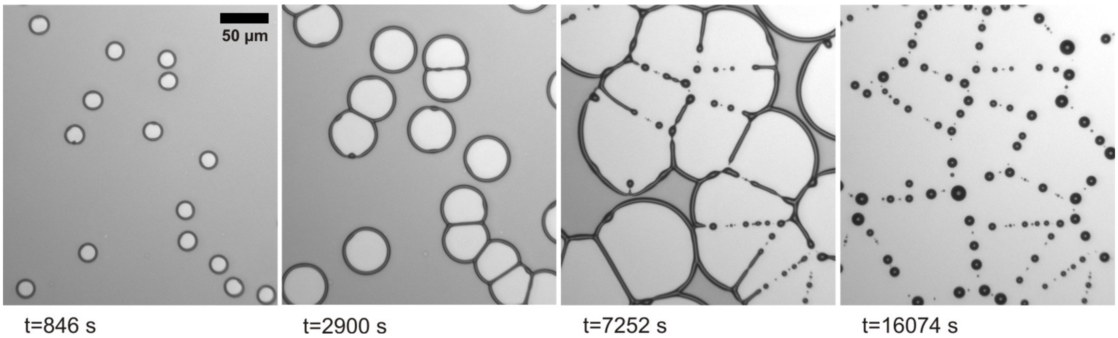

Figure 7.2: Different stages of a dewetting polymer film (PMMA, $M_w = 14\,\mathrm{kg/mol}$, $T = 150\,^\circ\mathrm{C}$, $h_0 = 120\,\mathrm{nm}$) on an OTS-coated silicon wafer.

7.1.4 Viscosity

Since the used polymers have different glass transition temperatures, comparing their slip lengths at the same temperatures is not appropriate. Rather, the molecular weights of PVP10k and PMMA14k are comparable, so the viscosity is mainly influenced by temperature. Furthermore, for low molecular weights as used for this study, viscoelastic effects can be neglected, and the liquid can be considered as newtonian [Fet2006a], which means that dynamics are dominated by their viscous properties. For this reason a comparison in dependence of the viscosity is inevitable.

By analyzing the dynamics of the hole growth and the rim profile of the hole – as described in the following sections (see also Chap. 2.4) – the capillary number Ca (see Eq. 2.19 and Eq. 2.21) and the viscosity η can be derived from the experiment. Equation 2.14)

$$\eta = Ca\frac{\gamma_{\mathrm{lv}}}{\dot{s}}, \tag{7.1}$$

connects the capillary number and the viscosity, whereby for PVP $\gamma_{\mathrm{lv}} = 50\,\mathrm{mN/m}$ and for PMMA $\gamma_{\mathrm{lv}} = 45\,\mathrm{mN/m}$ [Poc2002]. The dewetting velocity is described by $\dot{s}$. When the hole reaches a radius of $12\,\mu\mathrm{m}$, the dynamics get frozen by rapidly quenching the sample back to room temperature. This means, the velocity at the very end of the dewetting corresponds to Ca derived from the analysis of the holes rim as captured by AFM. In practice, the velocity is calculated as the time-dependent derivative at the end of the curves depicted in Figure 7.5.

The WLF-Equation (Eq. 4.8) describes the temperature-dependent behavior of the viscosity theoretically (see Sec. 4.1.3 and Ref. [Wil1955]). Figure 7.3 shows the viscosity as a function of temperature for PVP10k and PMMA14k as determined during this study, together with the corresponding fits of the WLF-Equation. With the knowledge of T_{g} and the assumption that T_∞ is about $50\,^\circ\mathrm{C}$ lower than T_{g} [Rub2003], only η_0 and B/f_{g} are fitting parameters. Where for B/f_{g} the known value for PS 30.3 was used as a start value [Rub2003]. WLF data and experimental values match nicely. Consequently, to

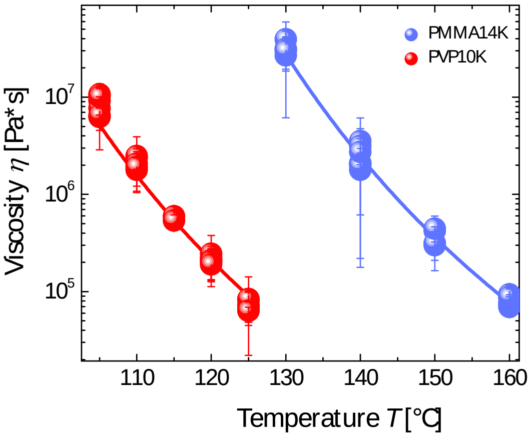

Figure 7.3: Viscosity of PVP10k (red) and PMMA14k (blue) as function of temperature. Solid lines represent the best fits of the WLF-Equation.

compare PMMA14k and PVP10k at the same viscosity, experiments with PVP10k have to be performed 30-35 K below the corresponding PMMA14k experiments. In the case of PMMA14k the studied temperature range was chosen between 130 °C and 160 °C, accordingly the temperature range for PVP10k dewetting studies was chosen from 105 °C to 125 °C.

7.2 Influence of the Polymer Chain's Side Group on Slippage

Assuming that phenyl rings are influenced by the substrate's structure and therefore develop their own order at the interface, it is possible that dynamic properties like viscosity and friction in this liquid layer differ from the not-oriented bulk material. Imaginable is layer of stacked molecules right at the interface that reduces friction towards the rest of the liquid, as sketched in Figure 7.1. This situation would be comparable to the apparent slip case, in which the very first liquid layer is stuck, but the flow profile in the upper layers implies a slip length (see Sec. 2.2). In this case, the used method to measure slip would deliver high readings.

The altered structure of PVP and PMMA compared to PS should change the characteristics of such a layer, and with that the slip length.

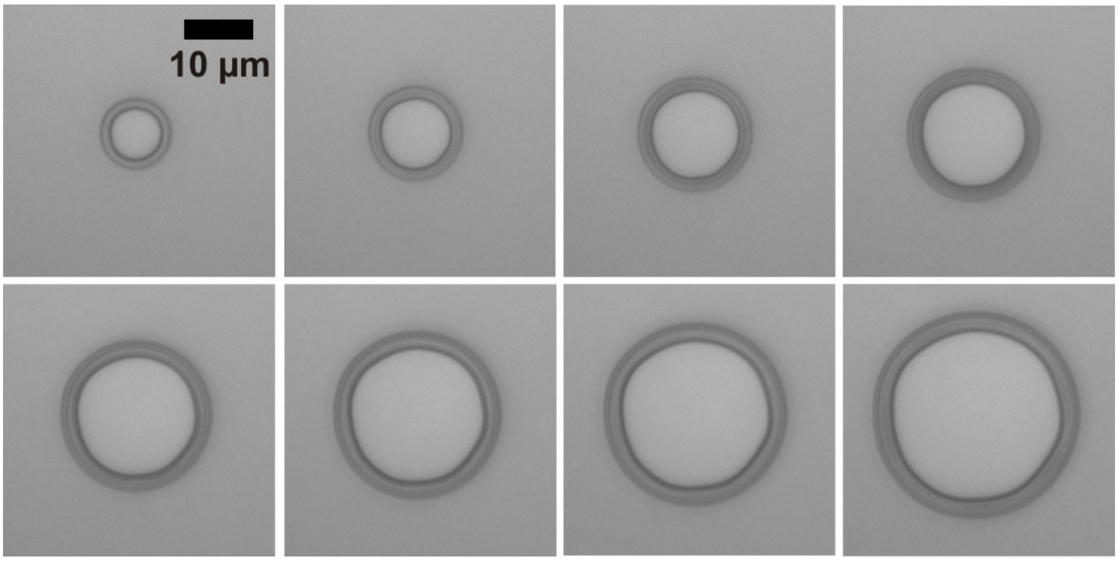

Figure 7.4: Growth of a hole in a 110 nm thick PVP10k film on a DTS-hydrophobized silicon wafer, at 105 °C. The process is stopped when the radius reaches 12 µm (time between snap shots: 698 s).

7.2.1 Evaluation of the Hole Growth Dynamics

From a picture series as seen in Figure 7.4, the radius R can be recorded as function of time t[2]. Figure 7.5 shows typical curves for $R(t)$ at different temperatures for PVP10k and PMMA14k on OTS and DTS. Curves for both polymers on AF2400 are included in Figure 7.12. A double logarithmic scale is chosen because of large differences in dewetting time. For example, a hole in a PVP10k film, dewetting on silanes at 125 °C takes 3 min to reach a radius of 12 µm, whereas at 105 °C, it takes 5 h. For PMMA14k, this range is between 5 min at 160 °C and 28 h at 130 °C.

Solid lines are best fits of Equation 2.12 to the data. The exponent α gives a first indication if the dynamics is in full, partial or no-slip regime (see Sec. 2.4.1). Values for PVP vary from 0.68 to 0.76, which is in the region of partial slip. PMMA exhibits with $\alpha = 0.72$ to $\alpha = 0.84$ slightly larger values, indicating lower slip. However, for each polymer and at a given temperature, no big differences between the dynamics on OTS or DTS are observable. On AF2400, α takes values between 0.81 and 0.92 for both PVP10k and PMMA14k.

A further analysis of the velocity $v = \dot{R}$ as a function of $\sqrt{R}^{-1}$ leads to the slip length. Yet, in this work the slip length is determined by the more accurate rim profile analysis.

---

[2] Figure 7.4 shows only a reduced amount of pictures. The actual density of snapshots is higher to ensure a smooth capture of the hole growth.

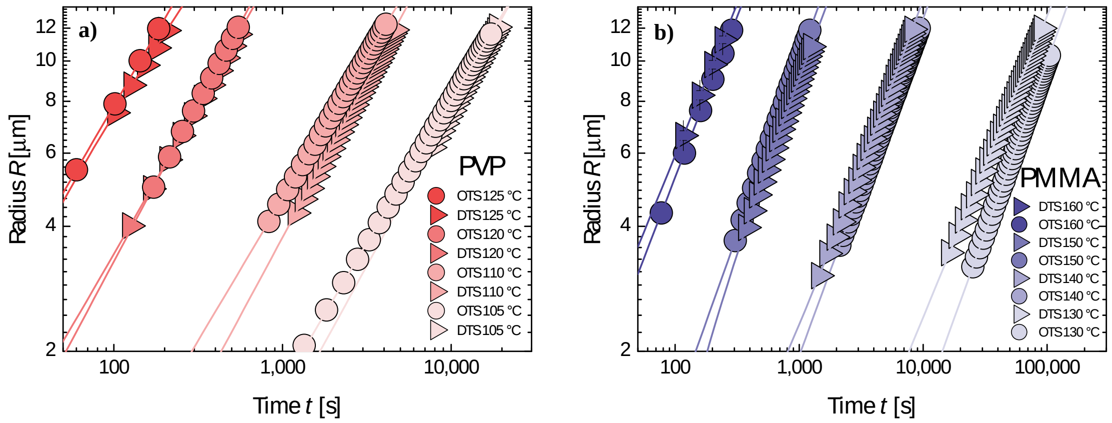

Figure 7.5: Radius versus time of growing holes in PVP10k (red) and PMMA14k (blue) films on DTS (triangles) and OTS (circles) at different temperatures (lower to higher temperatures are indicated by color shading from light to dark). Solid lines represent the best fit of Equation 2.12 to the data with $0.61 \leq \alpha \leq 0.84$. Graphs are shifted such that their origin agrees with the onset of the hole, according to the fit. For reasons of clarity, only every second data point is drawn.

7.2.2 Rim Profile Analysis & Evaluation of the Slip Length

Starting point for the analysis of the rim profile is an AFM scan, as shown in Figure 7.6. This picture shows a total view of a hole, whereas for the actual analysis one representative cross-section of the rim (see Fig. 7.7) is sufficient. To combine data acquired during the dewetting under optical microscopy and afterwards captured by AFM, the same hole should be analyzed. Nevertheless, AFM readings of further holes in the same sample can contribute to expand statistics.

The fitting procedure described in Section 2.4.2 leads to the slip length b. All rim profiles recorded for this study (see Fig. 7.7 and Fig. 7.13) showed a more or less pronounced minimum on their wet side. Accordingly, they were modeled using Equation 2.16, which allows the calculation of b with Equation 2.18.

Figure 7.7 and Figure 7.13 show representative cross-sections of all studied systems and temperatures. PVP10k was probed on OTS and DTS at 105 °C, 110 °C, 120 °C, and 125 °C, PMMA14k on silane substrates at 130 °C, 140 °C, 150 °C, and 160 °C. A comparison to the amorphous AF was performed at 110 °C and 120 °C for PVP10k, and at 140 °C and 150 °C for PMMA14k.

For PVP10k on OTS, a slight trend to deeper minima with increasing temperature is visible in the inset of Figure 7.7a. This indicates a decreasing slip length. For PVP10k on DTS, no such tendency is noticeable. All rim profiles show similarly shaped min-

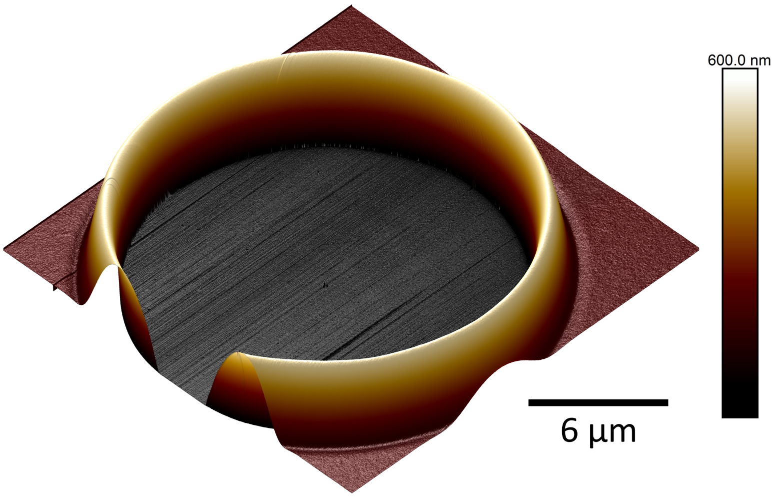

Figure 7.6: 3D rendered AFM image of a 24 µm wide hole in a glassy PMMA14k film on OTS, after dewetting at 150 °C.

ima, which is also the case for PMMA14k no matter on which substrate or at which temperature.

Figure 7.8 depicts the slip length extracted from the fitting of the rim profiles in dependency of temperature and viscosity. For PVP10k, slip lengths are above 100 nm on DTS and OTS and below 100 nm on AF2400. This trend is known from PS (see Fig. 7.9). Yet, in the case of PVP the difference between DTS and OTS is only small. In contrast to PS, PVP shows a higher slip length on OTS compared to DTS, but on a different scale. For PVP10k the slip length decreases slightly with temperature. Values vary overall from 0.1 µm to 0.4 µm, which is in the range of PS on OTS. Compared to PS, the temperature dependency is less distinct. In the case of DTS there is no consistent trend at all.

In the case of PMMA14k, slip lengths on DTS and OTS are on a lower level and and partially below 100 nm. However values on DTS and OTS stay above those determined on AF2400. PMMA14k shows slip lengths in the range of 0.1–0.2 µm, without any visible temperature dependency (see Fig. 7.8). Within the errors, there is no significant difference between DTS and OTS. By tendency, PMMA14k shows a slightly enhanced slip on DTS. Overall, all values match the range estimated by MD simulations $b \approx 15 \cdot (2R_\mathrm{g})$ [Bar1999], which results with $R_\mathrm{g}(\mathrm{PMMA}) = 3.18\,\mathrm{nm}$ [Rub2003] in slip length of about 100 nm.

Figure 7.9 summarizes the averaged slip lengths[3] for PS13k, PVP10k and PMMA14k on DTS, OTS and AF2400 respectively AF1600. Values for the viscosity of PS13k were

---

[3] Averaged slip length are acquired by the rim profile analysis of several (at least four) holes and samples. Error bars represent the error of th mean.

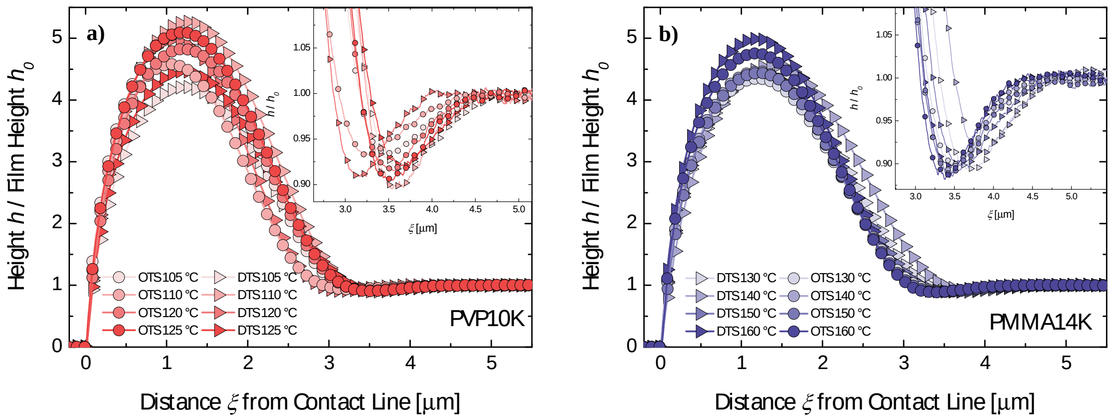

Figure 7.7: Rim profiles of dewetted PVP10k (red) and PMMA14k (blue) films on OTS (light circles) and DTS (dark triangles). Data is normalized to the prepared film height h_0 and the three-phase contact-line is shifted to 0. The graphs depict a reduced pixel density of the scans, to enhance clarity.

calculated using the WLF-equation (Eq. 4.8) and data from the original measurements [Fet2006a]. All three studied polymers show slip lengths below 50 nm on AF substrates without any temperature dependency. On silane substrates, slip lengths are clearly enlarged. PS13k exhibits the most distinct temperature and substrate dependency. With increasing temperature the slip length decreases. Slip lengths of PS13k on DTS exceed 1 µm. This remarkable behavior is neither found for PVP10k nor for PMMA14k. Values for PVP10k on both silanes are in the range of PS13k on OTS. For PMMA14k they even fall below this level, but stay above typical results on AF.

7.2.3 Discussion

For all studied polymers, the slip length on silanes is always larger than on AF. This suggests that ordering effects play an important role. Since PS yields the largest slip lengths, it seems to be most sensitive to the structure of the substrate. In this notion, the decrease of the slip length with increasing temperature, reaching close to the values of PVP10k and PMMA14k could be explained by an enhanced mobility of the PS molecules that would destroy the presumed order.

The presented findings corroborate the molecular picture derived from XRR-studies of PS (see Fig. 7.1 and Ref. [Gut2013]): The phenyl rings of PS follow the orientation of the SAM and form above the DTS substrate a layer that makes slipping for the rest of the liquid easier, whereas on OTS the phenyl rings arrange in a less stacked manner (see Fig. 7.1). Remarkable is the difference in slip length between PS and PVP, taken the fact that PVP is actually very similar to PS, yet in the phenyl ring only one carbon atom is exchanged by a nitrogen atom. The high slip length of PVP on DTS breaks down

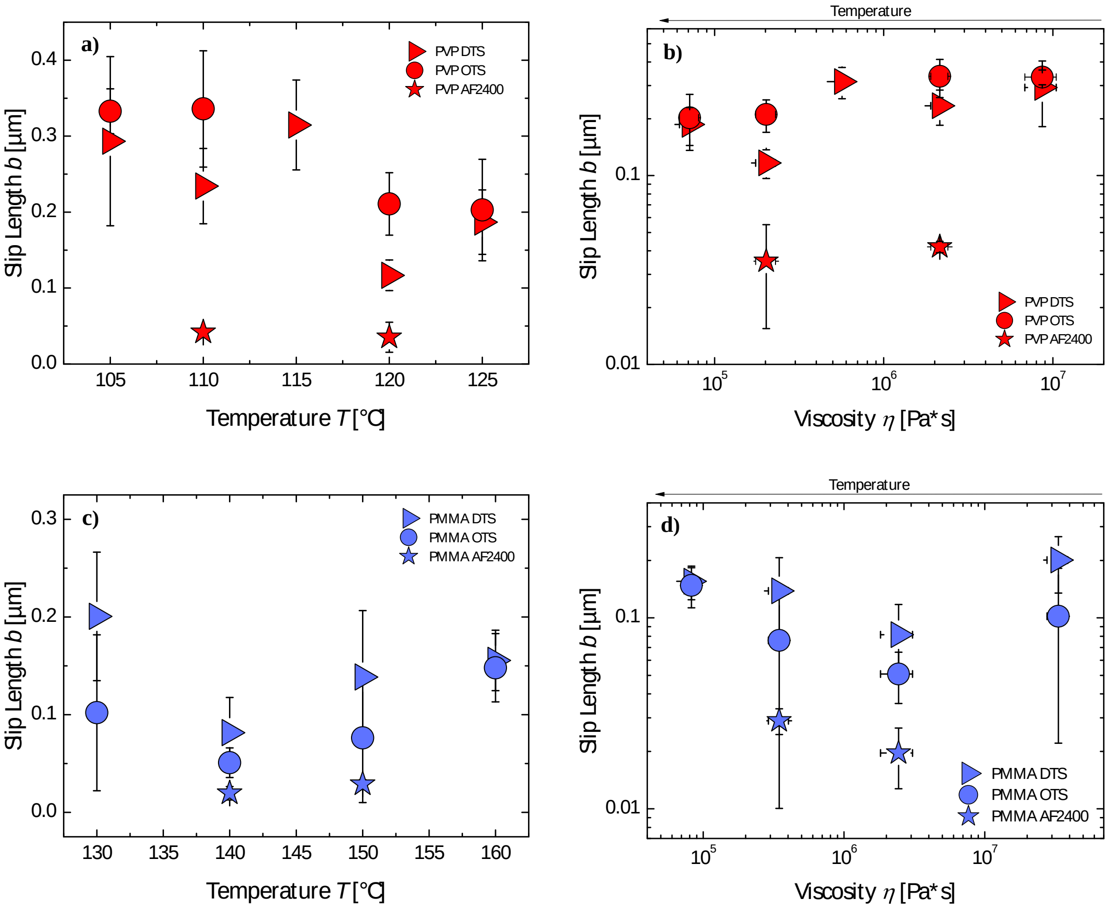

Figure 7.8: Averaged slip lengths b of PVP10k (red) and PMMA14k (blue) for different temperatures (**a)** and **c)**) and viscosities (**b)** and **d)**) on DTS (triangles), OTS (circles) and AF2400 (stars). Each data point represents the average over at least four individual measurements. Error bars represent the error of th mean.

to the level known from OTS. This fits very well in the presently introduced molecular picture: The ability of the side groups to form a π-π-like staking is hindered, because the delocalized π-electron system is disturbed. As a result, the interfacial layer is less pronounced (see Fig. 7.10). PMMA molecules have no ring-like structured side groups, that would be able to adopt any chain-wide order. An interface layer – as in the sense of PS and somewhat less pronounced in the sense of PVP – is not conceivable for PMMA. This would explain the relatively low slip lengths without temperature dependency. Only a minor ordering of the chains towards the structured substrate is imaginable, in contrast to the absence of any ordering on amorphous AF2400, as sketched in Figure 7.10. The assumption that the 30° tilt angle of the phenyl rings – induced by the DTS substrate – is energetically favorable as compared to 0°, enabling a kind of π-π-stacking, fits nicely

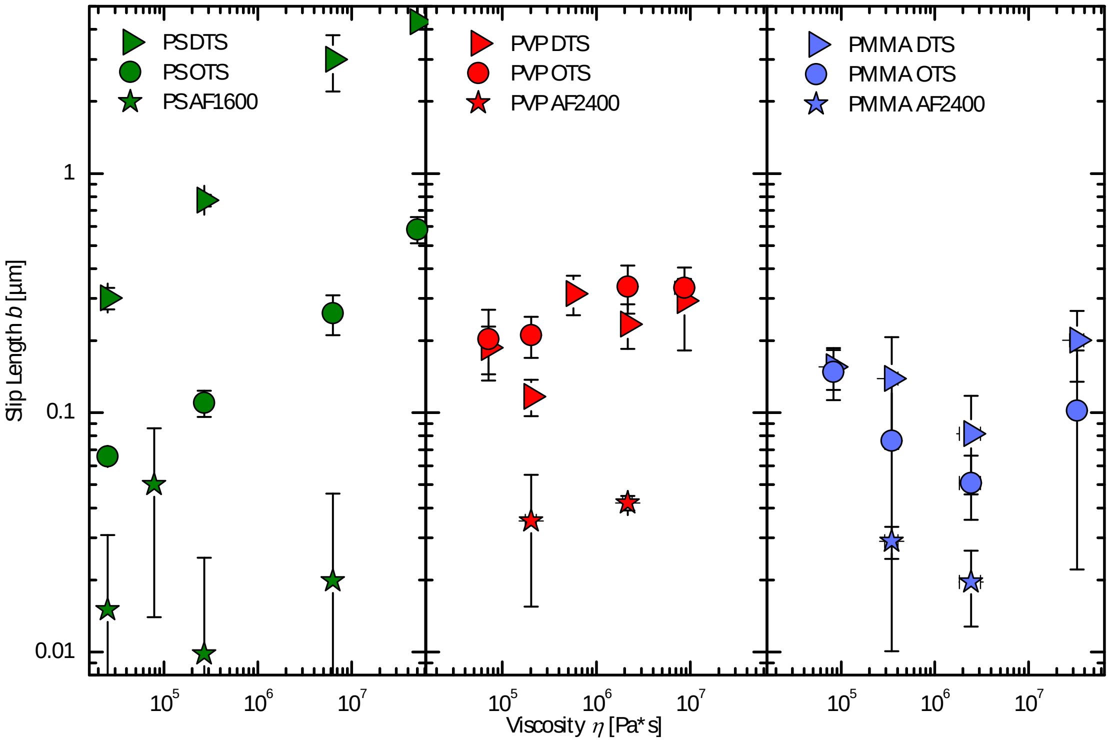

Figure 7.9: Overview of slip lengths of unentangled polymer melts (PS13k (green) [Fet2006a, Bäu2010a], PVP10k (red), and PMMA14k (blue)) on three different substrates DTS (triangles) and OTS (circles), and AF2400/AF1600 (stars), at different viscosities (tuned by temperature). Each data point represents the average over at least four individual measurements. Error bars represent the error of th mean.

into the presented model and would explain the big differences between DTS and OTS in the case of PS. Yet, there is still no direct proof that the side groups arrange in the suggested way nor that these angles are proven to influence the stacking. The aim of ongoing MD simulations presented in Chapter 8 is to evaluate if the phenyl rings of PS are influenced by the substrate in the setup of the simulation, and if this is the key for extraordinary slip lengths.

Apart from large slippage depending on the choice of the substrate and the kind of polymer, slippage can also be induced by entanglements. The next section is dedicated to the question whether PVP and PMMA show enhanced slippage above their critical molecular weight, as known from PS.

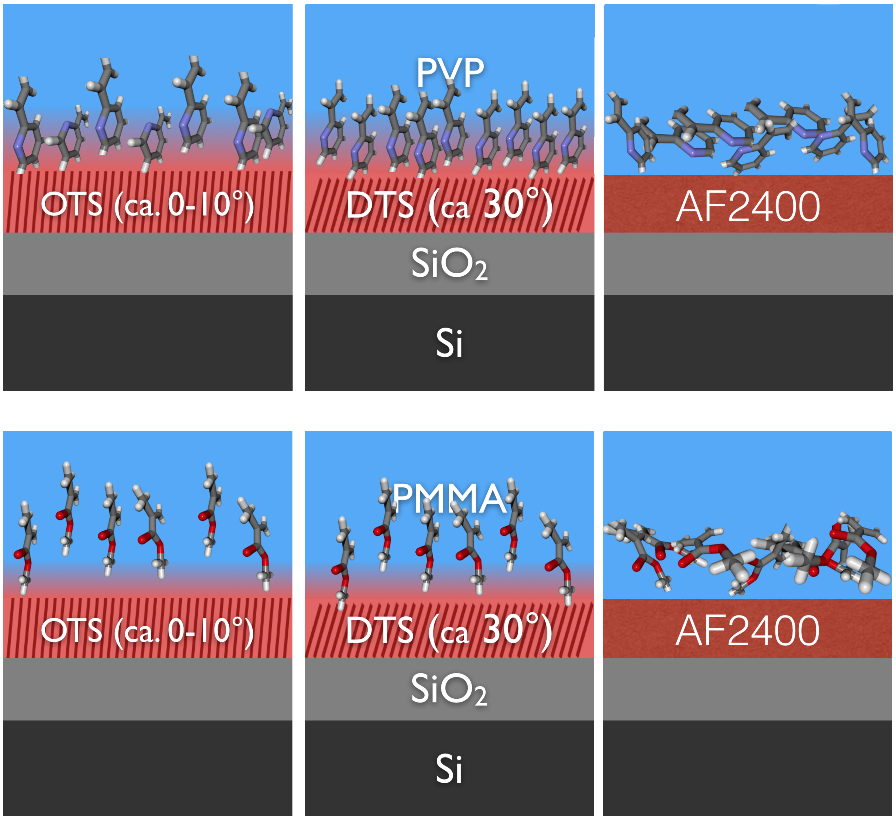

Figure 7.10: Conception of a disturbed π-π-stacking of PVP side groups (upper row) and PMMA groups (lower row) arranging at the interface to structured OTS and DTS and amorphous AF2400. For clarity, only monomers are drawn and bulk chains are neglected. Sketches of monomers are drawn using BallView 1.4 [Hil2010, Mol2006].

7.3 Influence of the Molecular Weight

As already mentioned in Section 7.2, the slip length for PMMA14k and PVP10k on amorphous AF is significantly lower than on silane-SAMs. Figure 7.11 shows a picture series of a dewetting PVP10k film at 110 °C on AF2400 and on DTS. By eye, it is already visible that the process is faster on the silanized surface. This behavior is known from PS [Bäu2008]. Bäumchen et al. [Bäu2009a] also showed that the slip length of PS increases with molecular weight, as soon as the critical molecular weight for entanglements M_c is exceeded. This was already modeled and predicted by de Gennes [deGen1971] and can be explained with the density of entanglements inside the liquid: With increasing chain length the network gets stronger and slippage is enhanced. However, towards the substrate, the density of entanglements is reduced. Strictly speaking, this kind of slippage can be seen as an example of apparent slip [Bäu2012a].

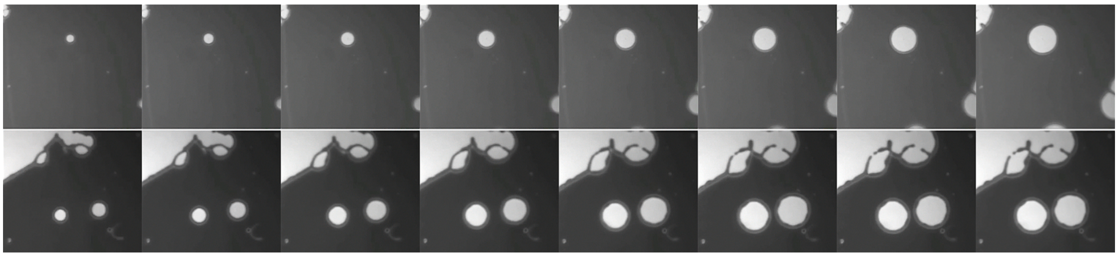

Figure 7.11: Snapshots of a dewetting PVP10k film with a thickness of approx. 100 nm on AF2400 (upper row) and DTS (lower row) at 110 °C. Time between single frames: 188 s.

The experiments and results presented in the following should be understood as a proof of concept that PVP and PMMA show a similar molecular weight dependent slip length. Therefore two molecular weights for each polymer were used: one above M_c and one below.

7.3.1 Experimental Details

For PS, M_c is about 35 kg/mol [Rub2003]. For PVP and PMMA, M_c should be in the same range (see Sec. 4.1.3 and Table 4.1). Therefore the already known results from PVP10k and PMMA14k – below M_c – are used together with supplementary measurements for 56 kg/mol PVP (PVP56k) and 57.8 kg/mol PMMA (PMMA57k), above M_c.

Preparation procedures and implementation are analog to the previously presented experiments. The hydrophobic AF2400 coating is applied to a piranha-cleaned standard silicon wafer sample by dip coating (same cleaning procedure as prior to silanization, see Ref. [Les2015]). Dipping the sample with a speed of 1 mm/s into 0.6% solution of AF2400 in FC-72 results in a 15 nm thick coating that features a roughness of 0.49(2) nm and a surface energy of 17.2(9) mN/m (see Sec. 4.3.2 and Sec. 5.1.2).

Polymer films are prepared as usual via spin coating on mica (30 mg/ml; 2500 min^{-1}; 110(10) nm), floated onto ultra-pure water and picked up with the prepared, hydrophobized wafer sample.

7.3.2 Dewetting Dynamics

Experiments were performed at two selected temperatures for each polymer: 110 °C and 120 °C for PVP10k/PVP56k as well as 140 °C and 150 °C for PMMA14k/PMMA57k. Figure 7.12 shows the radius of a growing hole as a function of time in PVP and PMMA films of low and high molecular weights at all four studied temperatures. A double logarithmic scale is chosen because of big differences in dewetting time. For example, a hole in a PMMA14k film takes about 400 s at 140 °C to reach a radius of 12 µm, whereas at the same temperature in PMMA57k it takes more than 700,000 s, in other words more than 8 days. The reason for this is the higher viscosity due to the higher molecular

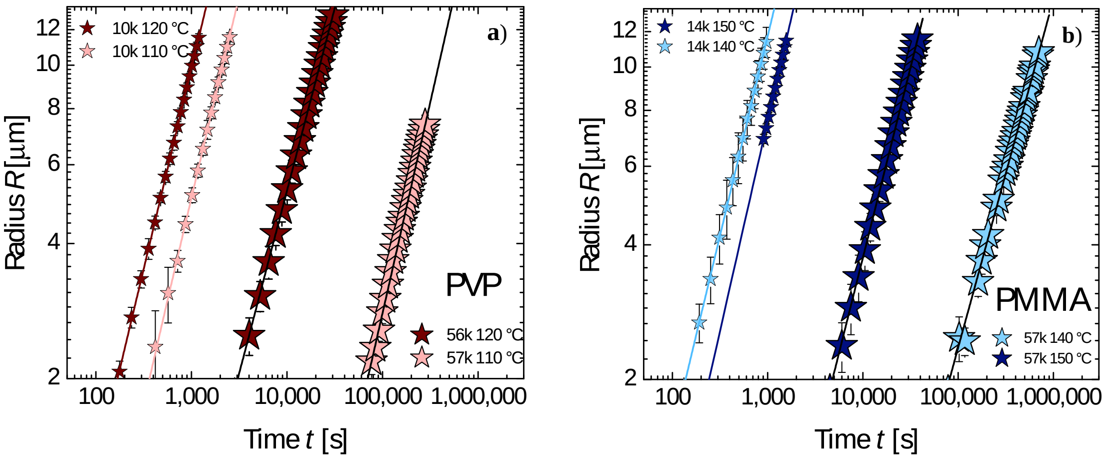

Figure 7.12: Radius versus time of growing holes in PVP10k (small red stars), PVP56k (big red stars), PMMA14k (small blue stars) and PMMA57k (big blue stars) films on AF2400 at different temperatures. Solid lines represent the best fit of Equation 2.12 to the data with $0.78 \leq \alpha \leq 0.92$. Graphs are shifted, so that their origin agrees with the onset of the hole, according to the fit. For reasons of clarity only every second data point is drawn.

weight. The influence of the molecular weight to the viscosity, respectively the speed of the receding film, is by far greater than varying the temperature by 10 K. The subjective impression of the time scales should not lead to a misjudgment of the corresponding slip lengths. The figure also shows best fits of Equation 2.12, leading to values of α between 0.78 and 0.92, with no clear trend for a particular molecular weight regime or temperature. As before, the slip lengths will be determined by the rim profile analysis, see next section.

7.3.3 Rim Profile Analysis

Figure 7.13 depicts the rim profiles corresponding to the dewetting dynamics depicted in Figure 7.12, normalized by the prepared film height h_0. At a given temperature, the high molecular weight polymer shows always a smaller minimum at the wet side of the film, indicating an enhanced slip length. Although some shallow minima are recorded for instance for PMMA57k at 140 °C, the rim profiles stay in the oscillatory regime. Therefore, the slip lengths were always determined with Equation 2.18 after a fitting of Equation 2.16 to the data. The resulting slip lengths are shown in Figure 7.14 as function of molecular weight. Judging from the distribution of the single measurements (see Fig. 7.14a), the two temperatures studied for each polymer do not have a significant influence on the slip lengths. Accordingly, an averaging over both temperatures seems reasonable to emphasize the molecular weight dependency (see Fig. 7.14b). Although the molecular weight is only moderately raised over M_c, values start to rise from

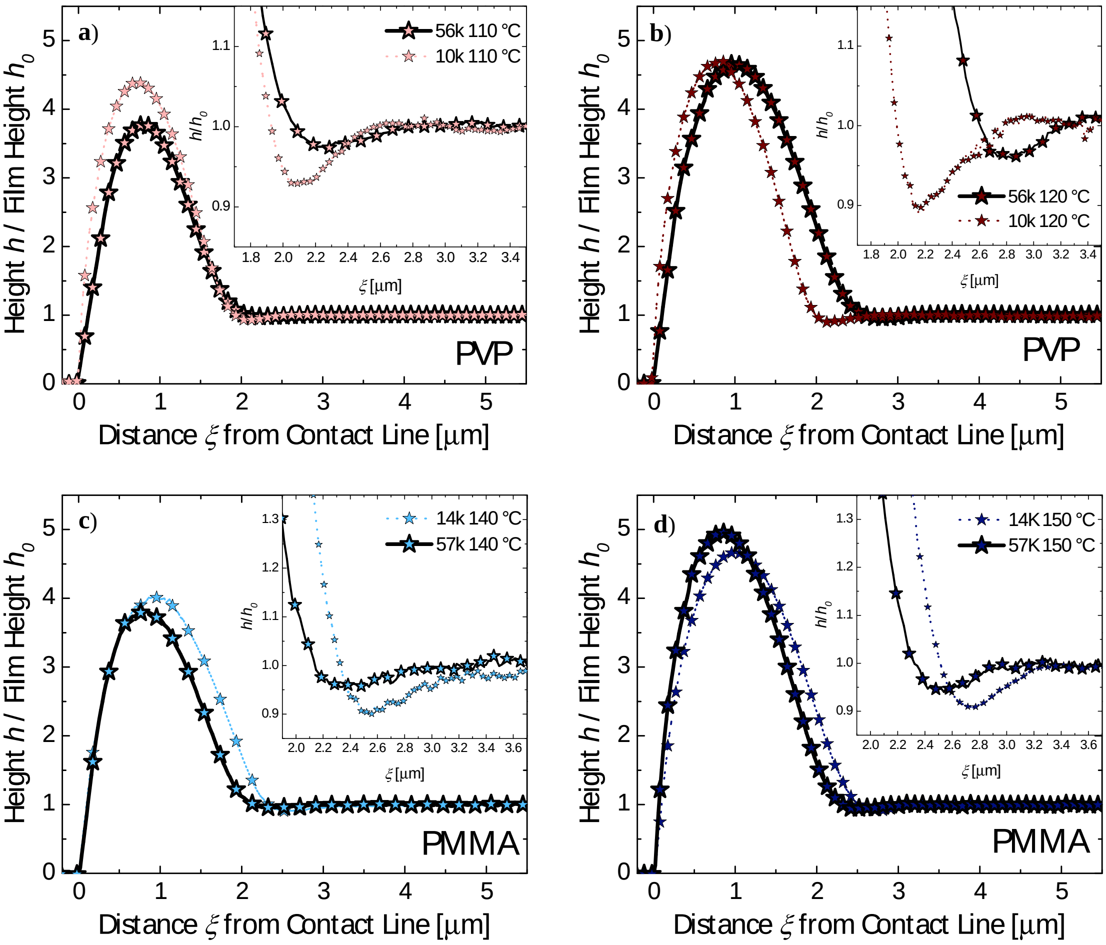

Figure 7.13: Rim profiles of dewetted PVP10k (thin red stars), PVP56k (bold red stars), PMMA14k (thin blue stars) and PMMA57k (bold blue stars) films on AF2400, captured by AFM. Data is normalized to the prepared film height h_0 and the three-phase contact-line is shifted to 0. The graphs depict a reduced pixel density of the scans, to enhance clarity.

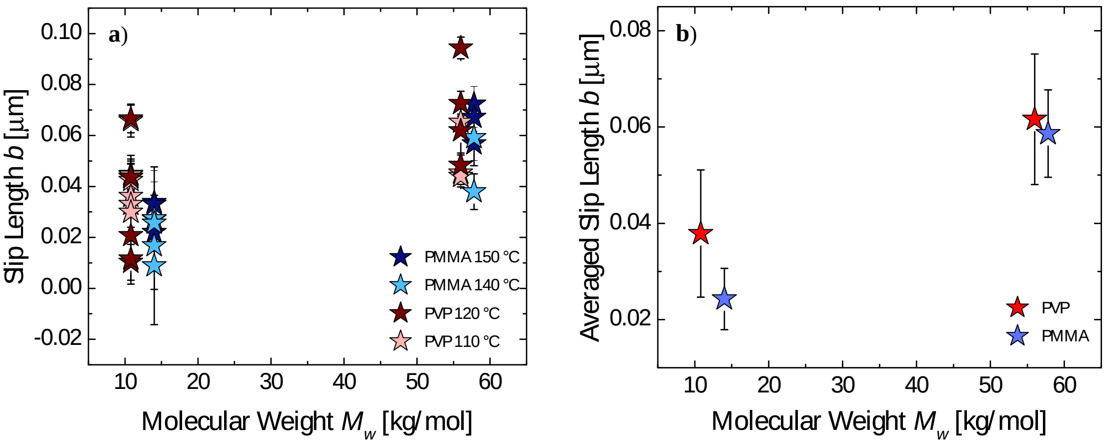

Figure 7.14: Slip length b of PVP10k (thin red stars), PVP56k (bold red stars), PMMA14k (thin blue stars) and PMMA57k (bold blue stars) as a function of molecular weight M_w on AF2400, derived from rim profile analysis. **a)** Single measurements, depicting all values at the respective low (light colored) and high (dark colored) temperature. **b)** Average values over all measured temperatures.

about 0.3 µm, for PMMA14k and PVP10k, to about 0.6 µm. With the knowledge of the behavior of polystyrene, doubling its slip length from less than 1 µm below its M_c to about 2 µm above M_c [Bäu2009a], the behavior of PMMA and PVP is qualitatively comparable.

7.3.4 Discussion

The presented data for PVP and PMMA is in line with the readings of polystyrene, showing an increased slip length above M_c. A clear trend to more monotonic rim profiles for the studied high molecular weights is observable. Varying M_w with respect to M_c and beyond, has a similar effect on the morphology of the rim profile as changing other conditions that influence slip, like the substrate or the polymer itself.

For certain, this study can only be understood as a basic comparison and validation. To reveal a quantitative behavior with increasing M_w – as seen for PS – more data has to be acquired at higher molecular weights. This would also improve the clarity of the trend compared to the relative high scatter of the presented single measurements. A future study focusing on this molecular weight dependency should result in a different slope of b as a function of M_w, since this behavior and calculation, given in [Bäu2009a] and [deGen1971], depends on polymer specific parameters. The molecular mechanism for this is explained in the mentioned publications, and not the main goal of the present thesis.

7.4 XRR Characterization of PMMA and PS Films

Starting point for the hypothesis of ordering side groups at the interface towards an ordered substrate was the detection of an interface layer between the polystyrene melt and the silane SAM [Gut2013]. This layer is characterized by a reduced electron density, and a certain thickness that can be connected to the height of the polystyrene's phenyl rings and their order.

With this picture in mind, PMMA should not form a similar layer, because it does not have a side group that is able to arrange in this manner (see Fig. 7.10). To investigate this, a comparative XRR study of PMMA14k and PS12k films prepared on DTS was carried out at DELTA BL9 (Dortmund, Germany).

PMMA14k and PS12k films were prepared with a thickness of 50 nm by spin coating on mica out of a 15 mg/ml toluene solution at 2500 min^{-1}. The film thickness was chosen as a good compromise between a 'bulk-like behavior' of the film and simplifying the modeling of the layered experimental system at time of data evaluation. The films are still well above the radius of gyration of PMMA14k and PS12k (see Sec. 4.1.3), have a bulk-like glass transition temperature, and are still experimentally handy, since too thin films would disrupt while floating.

The prepared PS12k samples were annealed on DTS for 30 s, at 120 °C – PMMA14k at 150 °C. Afterwards they were analyzed in the X-ray beam of BL9, driven at 13 keV.

Figure 7.15a shows the reflectivity R as a function of the scattering vector q_z for bare DTS, PS12k on DTS, and PMMA14k on DTS. The high-frequency oscillations (Kiessig fringes) arise from the 50 nm film thickness, a thicker film would result in even shorter oscillations, which would be more difficult to model. Here, the modeled reflectivity is drawn as a solid line, the corresponding electron density curves $\rho_\mathrm{e}(z)$ are shown in Figure 7.15b.

Unfortunately, the quality of the studied DTS coating is not as convincing as already seen in Chapter 5. Because of this, the model parameters of the pure DTS could not be transfered without refinement to the polymer-coated samples. This explains small differences in $\rho_\mathrm{e}(z)$ for $z \lessapprox 30\,\text{Å}$.

To interpret the reflectivity curve for the polymer covered DTS, one has to assume a box model that includes an interfacial layer between DTS and polymer bulk with a reduced electron density. The resulting minimum in the electron density curve is clearly seen in Figure 7.15 for both polymers. The results for PS on DTS correspond very well to the ones shown in our previous study [Gut2013]. Therein, however, the gap was interpreted as an indication for a possible π-π-stacking of the phenyl side-groups in PS. Surprisingly, in the new results, the gap is also necessary to model the PMMA reflectivity. PMMA however lacks a delocalized electron system of the side groups, and therefore a stacking is not possible. Hence, the gap cannot be the main characteristics for slippage. It is thereby

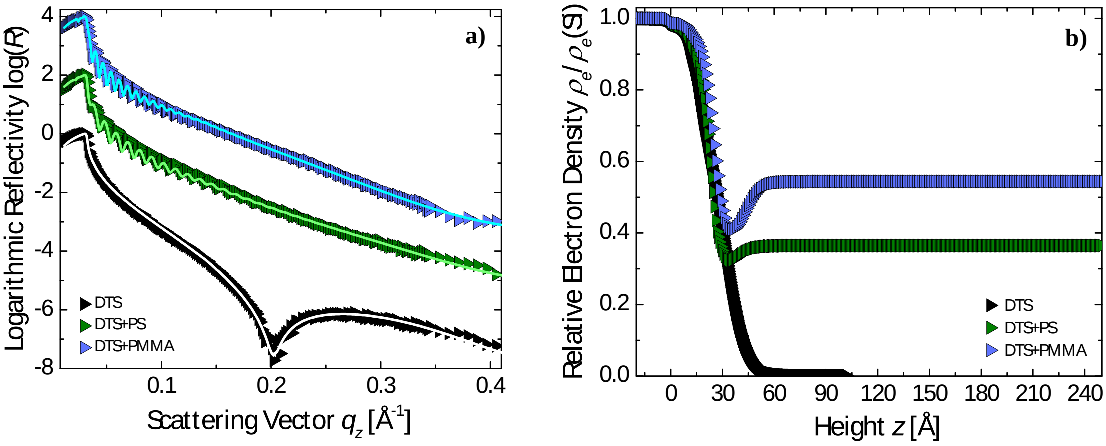

Figure 7.15: XRR analysis of 50 nm thick PMMA14k (blue) and PS12k (green) films on DTS. **a)** Measured reflectivity data R versus scattering vector q_z. (Curves are shifted for better visibility). **b)** Constructed electron density $\rho_e(z)$ matching the fits (solid lines) in a). Curves are normalized to the ρ_e of the silicon substrate. Black: Bare DTS substrate prepared standard silicon wafer.

not excluded, that a slip boundary condition leads to a dip in the electron density, yet for other reasons than stacking.

What are alternative explanations for a reduced electron density at the solid/liquid interface? Consulting the literature on XRR data of similar systems, a dip is frequently found (e.g. [Mez2006]). A common explanation (see a discussion in the reviews by Lohse et. al. [Loh2015] and by Neto et. al. [Net2005]) is the presence of a gas layer (e.g. in the form of nanobubbles) at the interface. Along the same line, also artifacts, like float gaps or other spatial inhomogeneities of the polymer film, might lead to an electron density dip, since the XRR signal collects information averaged over several square millimeters. Nanobubbles are unlikely for polymeric systems, yet float gaps cannot be completely avoided during the preparation of the films on non-wettable substrates. MD simulations implicate that in the presence of a thin gas layer the no-slip boundary condition vanishes [Loh2015]. Yet, the computed slip length are orders of magnitude below the slip lengths in our experimental system. To get a closer insight into the molecular origin of slip in our systems as well as the reduced electron density, all-atom MD simulations of polystyrene on silane-like substrate are initiated and will be discussed in the next chapter.

Since from the given data the latter can not be excluded, and the hypothesis of ordering phenyl rings is only one possible interpretation of the data. The systems will be analyzed with more sensitive methods, like grazing incidence diffraction in future. This is ongoing collaborative work with Philip Gutfreund and Max Wolff at DESY (Hamburg, Germany).

7.5 Summary

The influence of the liquid on the slip boundary condition was studied for non-entangled and entangled polymers. To see whether the side-group of the polymer has an influence on the slip length, slip of non-entangled PVP and PMMA was compared to former results of non-entangled PS. On both – DTS and OTS – surfaces PVP exhibits a slip length of some hundreds of nanometers, which is on the level of PS on OTS but significantly lower than PS on DTS. A slight temperature dependency is still visible (slip lengths decrease with increasing temperature). For PMMA on silanes, the slip length is even lower than in the case of PVP. A temperature dependency is not observable. However, for all studied polymers, slippage on silanized surfaces is always higher than on amorphous Teflon® AF surfaces.

On Teflon® AF surfaces, PVP and PMMA follow the same trend as known from PS: slip lengths increase with molecular weight. For this 'proof of concept' study, only one molecular weight above the critical molecular weight of entanglements was used.

The XRR analysis of PMMA films on DTS reveals a similar interfacial electron depletion between silane substrate and bulk polymer film as already seen in previous studies of PS on silane substrates, indicating that the hypothesis of ordering phenyl rings at the interface is only one possible interpretation of the data.

8 Molecular Dynamics Simulations

Based on modern simulation tools, molecular dynamic (MD) simulations have been set up in order to independently develop a possible molecular picture of the interface between liquid and solid, where an interfacial liquid layer is hypothesized with properties deviating from the bulk liquid. From the experiments, this interfacial layer is identified of being responsible for the slip boundary condition. However, from the experiments, only indirect evidence is given for this interfacial layer, e.g. by dewetting experiments or by XRR, where a depletion of the electron density function between solid and liquid is observed. Experimental insight into the molecular (re)arrangements at this interface during the sliding of the dewetting polymer melt is not possible. Therefore, MD simulations shall explore this situation.

This chapter tries to develop an independent picture of structures and dynamics at the interface. For this purpose, every atom of the polymer melt and the substrate was rebuilt in molecular dynamics simulations. The presented work is a close collaboration with Laurent Joly (Institut Lumière Matière, Lyon, France)[1].

8.1 Simulation Details

In the MD simulations, by using the LAMMPS package, three differently ordered substrates were set up together with polystyrene [Pli1995].

The simplest substrate is silica (see Fig. 8.1a) with a hydroxyl surface density of about $4.5\,\mathrm{nm}^{-2}$, to mimic the oxide surface of a silicon wafer [Zhu1987]. To get such a surface conformation, a β-cristobalite SiO_2 crystal is cut along the (111) plane, at a depth where the surface shows non-bridging oxygen atoms with the desired density. All oxygen atoms are saturated with randomly oriented hydrogen atoms. Further details on the design of this surface can be found in References [Pui2003, Ho2011]. The whole layer stays rigid during simulations. This type of substrate/system will be named SiOeq in the following, where 'eq' means 'equivalent'.

---

[1] Simulations were set up and designed in close cooperation. The code base and the theoretical background was delivered by Laurent Joly. Simulations were split into two work packages: 1. Systems with substrate and polymer to simulate friction. 2. Systems with only bulk polymer to simulate viscosity. The first part was computed at Saarland University, the second part at Institut Lumière Matière. The present work only shows and analyzes data from Part 1.

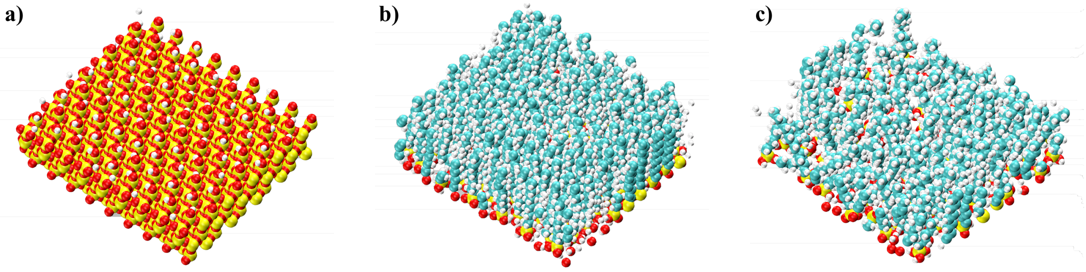

Figure 8.1: Simulated substrates depicted as space-filling models, from left to right: β-cristobalite (SiOeq), DTS with a density of 5.0 chains/nm^2 (OTSeq), and DTS with a density of 3.5 chains/nm^2 (DTSeq). Carbon: blue; Silicon: yellow; Oxygen: red; Hydrogen: white. Images generated with VMD 1.9.2 [Hum1996].

The other two surfaces mimic the silanized substrates. In the simulations, the two experimentally studied OTS- and DTS-SAMs (see Chap. 5) are represented through DTS chains, which are randomly placed on a hexagonal lattice at the bottom of the simulation box with a predefined density, equal to the density of OH bonding sites on a typical silicon dioxide surface. The head group's bonding position stayed in place throughout simulations. The supporting silicon and silicon dioxide were neglected and replaced by a meanfield 9-3 Lennard-Jones potential, describing the van der Waals (vdW) interactions. As seen in Chapter 5, the differences in structure between OTS- and DTS-SAMs arise mainly from their different grafting density and not their different lengths. With this knowledge the simulations are reduced to DTS molecules only, but with two different grafting densities. A density of 5.0 chains per nm^2 corresponds to a typical OTS-SAM (see Fig. 8.1b), the equivalent to a DTS-SAM is simulated with a density of 3.5 nm^{-2} (see Fig. 8.1c). For convenience the two different simulated surfaces/systems are named OTSeq and DTSeq in the following.

The entire simulation box has dimensions of about 46 Å in x- and about 45 Å in y-direction (see Fig. 8.1 and Fig. 8.3). Periodic boundary conditions are used along both directions, effectively forming a lateral infinite environment.

Polystyrene was designed with a length of 10 monomers, corresponding to a molecular weight of approximately 1 kg/mol. This low value – compared to experiments – was chosen as a compromise to reduce computing time.

Inter- and intra-molecular interactions are described by the OPLS-AA (Optimized Potentials for Liquid Simulations-All Atom) force field [Jor1996]. Long-range Coulomb interactions are computed with the particle-particle-particle-mesh (PPPM) method [Hoc1988].

Initial simulations were carried out at 600 K to increase the dynamics of the system and to reduce simulation time at the initial equilibration phase. Figure 8.2 shows the first 60 ps of the DTSeq system at 600 K in 10 ps snapshots: The simulation starts with 45 chains randomly placed above the substrate. In the very first step, the total simulation box is wider than its final size, to be able to place the molecules randomly on the regular

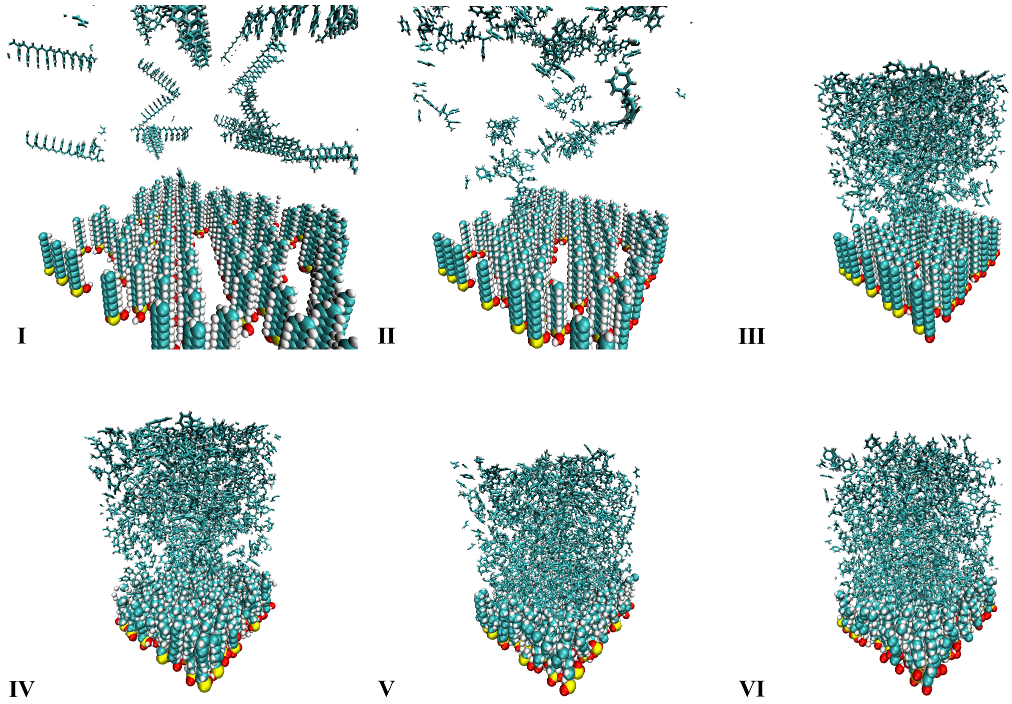

Figure 8.2: Snapshots of the initial configuration and first relaxation steps of DTSeq system at 600 K in time steps of 10 ps. For better visibility, the polystyrene is depicted in ball and stick representation, whereas a space-filling model was used for the silane substrate. Images generated with VMD 1.9.2 [Hum1996].

lattice, and ensure that they do not touch. In the second step, the box shrinks and the polystyrene is allowed to move, in contrast to the silanes. Step III shows the box at its final size. The polystyrene film is kept below a certain z-level by an artificial wall (not visible). From Step IV onwards, the silanes are allowed to move. The artificial wall is removed in Step V, the polymer forms now an approximately 40 Å thick film, and the system continues its equilibration in the NPT ensemble (constant number of atoms, pressure and temperature) for 4 ns, in total (Step VI and later).

After another equilibration phase of 4 ns in the NPT ensemble, the actual production phase of 4 ns starts. The liquid was maintained at the respective temperature using a Nosé-Hoover thermostat [Nos1984, Hoo1985]. The equations of motions were integrated using the Velocity-Verlet algorithm [Ver1968, Ver1967] every 1 fs. The above described very first steps (I-V) are only carried out at 600 K. After finishing the simulation at 600 K, the temperature was decreased in steps of 50 K down to 350 K. The final configuration of the higher temperature was always used as the starting configuration of the simulation at the next lower temperature.

The simulations are designed to yield the slip length via the Green-Kubo formalism [Boc2013]. The autocorrelation function to derive the friction coefficient κ is taken from the simulated systems that contain the polystyrene melt and one of the three substrates. For each temperature, an independent simulation of bulk polystyrene delivers the viscosity η. Eventually, both readings lead to the slip length b, according to Navier's definition $b = \eta/\kappa$ (see Eq. 2.5 [Nav1823]). The following data evaluation focuses on 'visible' structural formations and processes in the polystyrene-substrate systems. The analysis of the dynamics in detail – including the slip length – will be part of a future work.

8.2 Data Processing and Evaluation

8.2.1 Mass Density

The upper row of Figure 8.3 shows snapshots of the three simulated systems at 350 K. For each time step, the position of every single atom is known. By averaging over time the noise is reduced and it is possible to compute a mass density profile for each kind of atoms (see lower row Fig. 8.3). The 'head group' combines the density of the silicon and oxygen atoms of the silane layer. This group is not present in the SiOeq system. The oscillations in mass density of the substrate arise from the crystal or crystal-like structure of the β-cristobalite (SiOeq) and the very dense silane (OTSeq). The oscillations decline with less crystallinity: The curve for DTSeq shows only one peak at the head group's position, whereas the tail of the silane chain has an almost smooth trace.

Between polystyrene film and substrate the mass density features a dip (see gray arrows in Fig. 8.3). The overall shape, including this dip, matches the characteristics of the electron density discussed in Section 7.4 and determined by our group and co-workers [Gut2013], in the past.

8.2.2 Electron Density

From the mass density determined in simulations, precisely the known number density of the atoms, it is possible to estimate the electron density. A MATLAB® script assigns the theoretically associated electrons to every atom and sums them up. This simple approach does not care for the exact position of the electrons and the size of individual atoms, for example in delocalized systems. However, considering the given noise, this should not make a visible difference. Figure 8.4a shows the electron density profiles (EDP) calculated from the number densities corresponding to the data shown in Figure 8.3. To

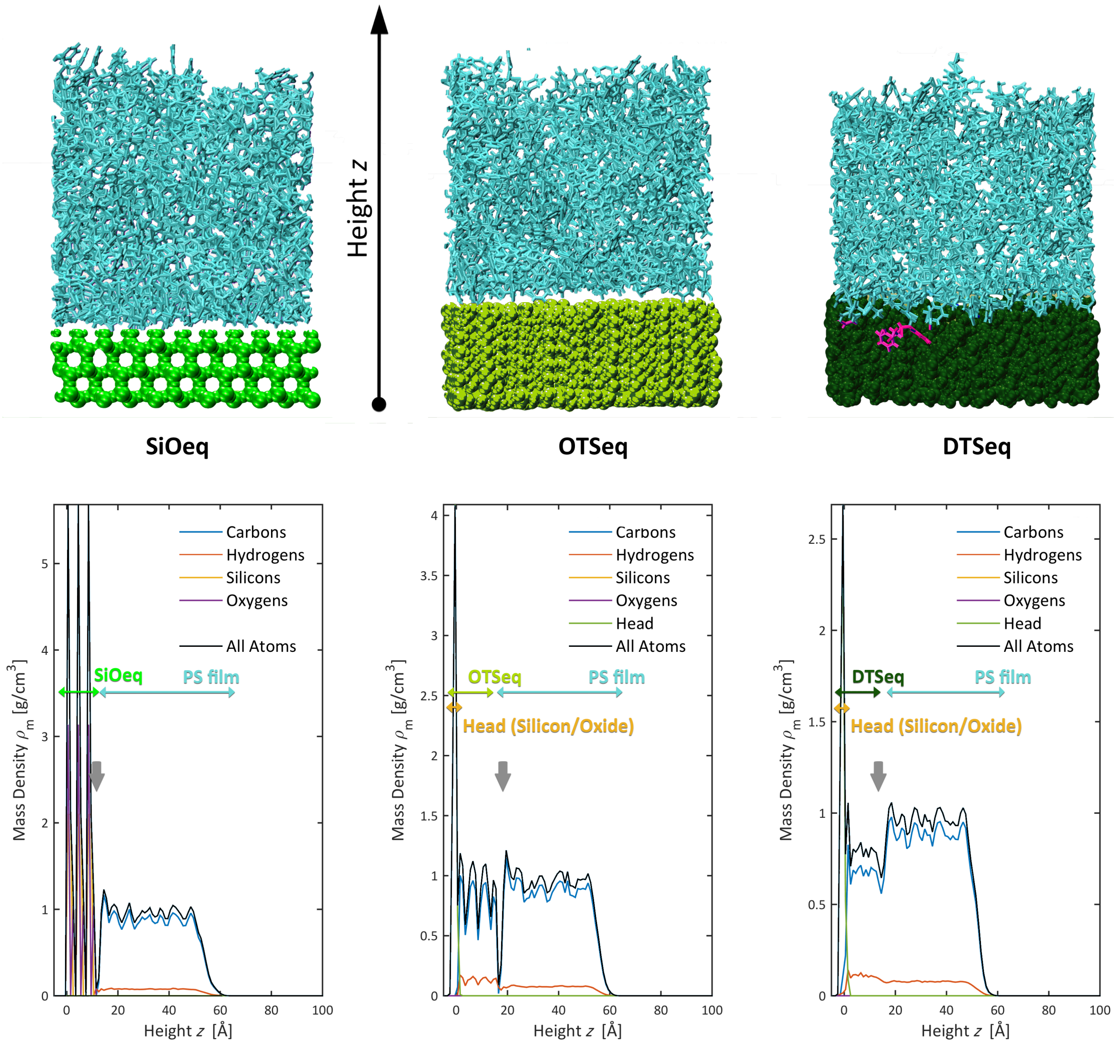

Figure 8.3: Upper row: Snapshots of the SiOeq, OTSeq and DTSeq systems, at 350 K. The polymer melt is colored in light blue. Segments of the polymer that are below the mean height of the respective substrate (green) are colored in purple. To improve clarity the polymer is depicted as a ball and stick model, whereas the substrate is drawn using a space-filled model. Images generated with VMD 1.9.2 [Hum1996]. Lower row: Corresponding mass density profiles $\rho_\mathrm{m}(z)$. Please note the tilted z-axis compared to the snapshots. To reduce noise, the data is smoothed using a moving average smoothing with a range of 1 (Equation 8.1). The gray arrows mark the 'dip' in mass density between PS film and substrate.

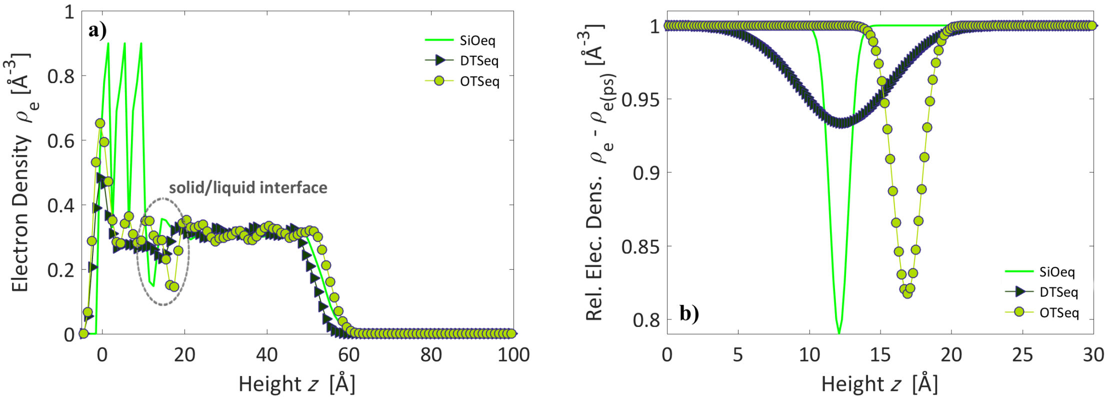

Figure 8.4: a) Electron density profile of the SiOeq (solid line), OTSeq (circles) and DTSeq (triangles) systems, at 350 K. Data is smoothed by a moving average smoothing with a range of 3 (see Eq. 8.1). **b)** Fits of the dip zone between polymer and substrate, normalized to the mean electron density of the polystyrene film.

simplify a further analysis of the curve and to damp the oscillations of the substrate, a moving average smoothing

$$y(n) = \frac{1}{range}(x(n) + (x(n-1) + \cdots + (x(n-(range-1))), \tag{8.1}$$

with a *range* of 3 is applied to the ρ_e. The EDP match very well the already measured and simulated EDPs for DTS and OTS (see Chap. 5.3.3 and other data gained by our group and co-workers [Les2015, Cas2015]), except for the absolute height of the OTSeq layer compared to actual OTS. The difference in height arises from the design of the simulations that uses only DTS molecules to mimic the SAMs. Although the current simulations use a simplified approach to recreate the OTS- and DTS-SAM by just varying the lateral density of a DTS layer, the overall characteristics in electron density are reproduced nicely: OTSeq shows a sharp interface between silane layer and polymer film in contrast to the rougher interface of DTSeq, also seen in the sharp and broad shapes of the interfacial dip (see Fig. 8.4b). A result that nicely corresponds to the real substrates. Absolute ρ_e values for the silane's tail are for the simulated substrates in the range between 0.2–0.4 Å^{-3} and also match the one the experiments shown in Figure 5.6 nicely.

8.2.3 Electron Density Dip Between Substrate and Polymer

The dip in ρ_e between substrate and polymer film resembles the interface layer recently discovered by our group and co-workers [Gut2013]. Since that study links the dimensions of the dip to an alignment of the chains, this part of the EDP is of special interest. To measure the position, relative depth, and relative width, the EDP is normalized to the mean electron density of the polymer film. Alternatively these parameters could be

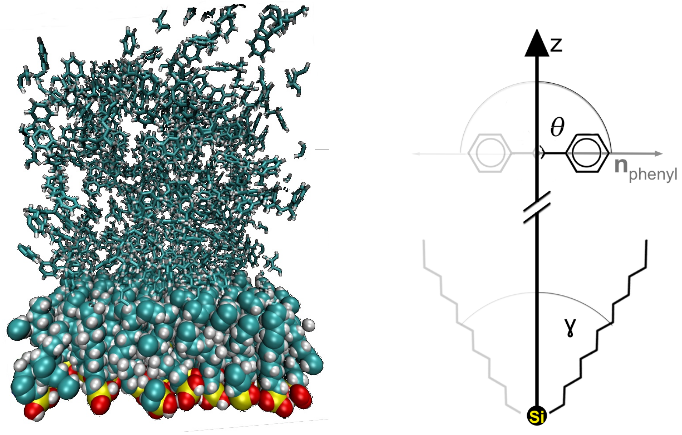

Figure 8.5: Definitions of the tilt angles of the phenyl ring and the silane chain. The tilt θ of the phenyl ring is measured relatively to the z-axis of the simulation box. The tilt of the silane molecule γ is defined from the tail's center of mass to the surface normal (equivalent to z-axis). Simulation snapshot generated with VMD 1.9.2 [Hum1996].

measured relative to the substrate, but because of the fluctuations for SiOeq and OTSeq, as well as the smeared out data for DTSeq and the absolute difference, averaging over the homogeneous PS electron density is more meaningful. Moreover, this method helps to distinguish changes of the dip independently from temperature induced changes of the polymer film, when comparing simulations at different temperatures, as to be seen in Section 8.3.1.

A MATLAB® scripts detects the peaks/dips and fits a Gaussian curve to the data. Figure 8.4b shows fits to data of the SiOeq, DTSeq and OTSeq systems at 350 K. In the SiOeq and OTSeq simulations, the dip is fairly narrow and almost identical in depth. Because of the thicker OTSeq silane layer – about 15.4 Å compared to about 11.1 Å for SiOeq – the dip is shifted to higher z-values, but the relative position above the substrate remains almost constant. In the case of DTSeq, the dip is broader and less deep, which indicates that the interface between silane and polystyrene is not sharp. The minimum of the dip is – compared to OTSeq – shifted to the left, meaning that on the one hand the DTSeq-SAM is, on average, smaller in height than the OTSeq-SAM. On the other hand this suggests, that the interface is a mixed zone of polymer and silane. A look at the snapshots in Figure 8.3 visualizes this interpretation. In the SiOeq and OTSeq systems, a clear gap between PS and the substrate is visible, whereas in the DTSeq system the SAM is open-pored enough for the polystyrene to penetrate the subjacent layer. In general, the polymer film is closer to the DTSeq substrate than to the other two.

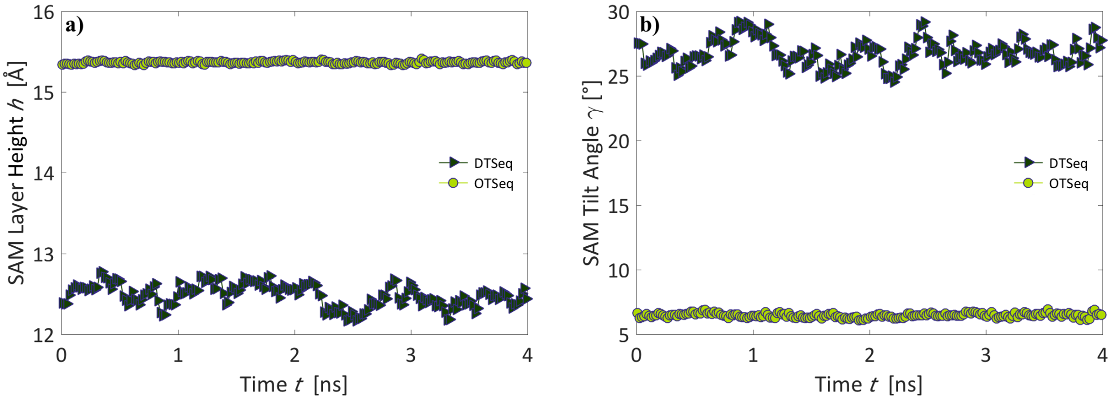

Figure 8.6: a) Averaged SAM layer height h and **b)** mean tilt angle γ of DTSeq (triangles) and OTSeq (circles) as a function of time, at 350 K. Every data point represents a spatial mean value averaged over 10 ps (For better visibility, only every second data point is drawn).

8.2.4 Tilt Angles

The grafting densities of the silane molecules has a direct impact on their tilt angle and therefore on the height of the silane layer, as already discussed in Chapter 5 and in one of our recent collaborative studies [Cas2015]. This can also be shown in the present simulations: The tilt angle γ of a single silane tail is defined from its center of mass to the surface normal, as sketched in Figure 8.5. The tilt angle θ of the phenyl side group is measured with respect to z-axis of the simulation box. Please note, that the direction of the tilts (azimuthal angle) is not taken into account. With these definitions, $\gamma = 0°$ characterizes an upright standing silane chain, and averaged $\theta = 90°$ randomly oriented side groups.

Figure 8.6a shows mean values of the silane SAM's height h as a function of the simulation time t at a simulation temperature of 350 K. The height of the OTSeq-SAM layer stays almost constant at 15.4 Å, whereas the DTSeq fluctuates over time between 12-13 Å. A comparison of the actual height of the DTS molecule to the length of an elongated chain (head + 15.04 Å tail length) leads to tilt angles of about 6° for OTSeq and 25-30° for DTSeq (see Fig. 8.6b). Both dimensions match the values known from measurements and simulations in both cases (see Chap. 5). Because of the OTSeq's high grafting density the chains have almost no room to bend, whereas the lower density in the DTSeq-SAM enables them to bend and to wobble.

To analyze whether the grafting density and the bending of the silanes have an effect on the alignment of the polystyrene's phenyl rings, their density and tilt angle is measured. Figure 8.7a shows the number density ρ_n of only the phenyl rings (without backbone) as distributed in the simulation box along the z-axes. All densities fluctuate around their 'bulk' value and have a slight peak towards the substrate. Keeping in mind that the height of the SiOeq substrate is 11.2 Å the phenyl rings stay mainly above this level,

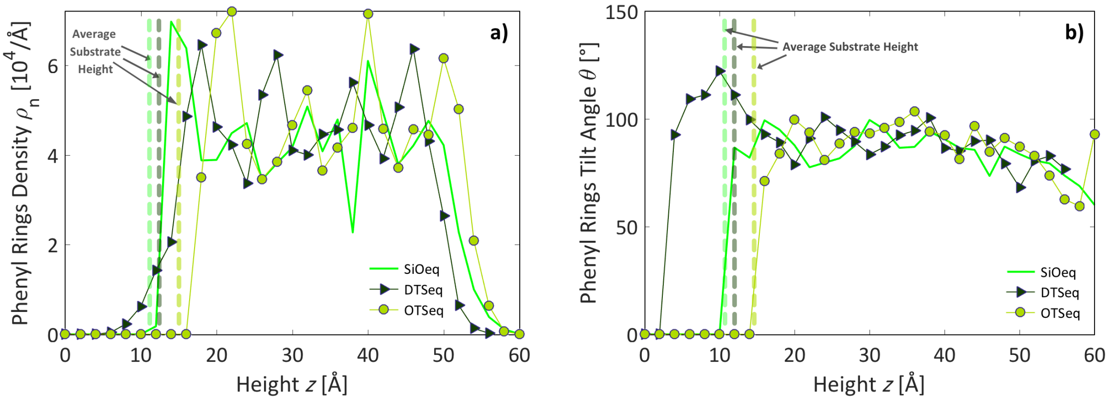

Figure 8.7: a) Time averaged mass density ρ_n of phenyl rings on SiOeq (solid lines), DTSeq (triangles), and OTSeq (circles), at 350 K; **b)** Corresponding time averaged tilt angles θ of phenyl rings. Single data points are averaged over $\mathrm{d}z = 2$ Å.

as already seen in mass and electron density curves for the total system (Fig. 8.3 and Fig. 8.4). The same is true for the OTSeq system: the density stays strictly at 0 Å^{-3} for z-values below about 16 Å, beyond this height, it jumps to the first peak. For DTSeq the situation changes. The DTSeq silane layer has an average height of 12-13 Å, but the density curve starts to rise already at about 9 Å, and increases monotonically up to the first peak at around 16 Å. This means that some rings penetrate the DTSeq substrate, forming a mixed interface; a behavior that could also be read out from the mass and electron density curves for the entire system.

Figure 8.7b shows the averaged tilt angle θ of the phenyl rings as a function of the height z. According to its definition, the mean value of the angle – if rings take no preferred direction – should be 90°, and indeed, it levels at about 90° inside the film. This is the case for all three systems. Only the curve for the DTSeq systems shows a peak towards 120° at about 10 Å. This corresponds to a tilt of 30°, compared to the initial position. This angle agrees with the silane's orientation. The comparison of tilt and density curve for PS on DTSeq shows, that only a few rings share the angle of the SAM, and these molecules are inside the SAM, respectively in very close contact.

8.2.5 Mean Square Displacement

If slip plays a role in the simulated systems the mobility at the solid/liquid interface should differ from the mobility inside the bulk polymer. To get a first impression of the kinetics in the systems, the mean square displacement (MSD) is used, which is defined as

$$MSD(\tau) \equiv \left\langle (x(t_0+\tau) - x(t_0))^2 \right\rangle_{t_0} . \tag{8.2}$$

More practically, it describes the displacement of an atom from an initial position $x(t_0)$ during the time frame dt:

$$MSD(\tau = i \cdot dt) = \sum_{i_0=0}^{N-i-1} \frac{1}{N-i} \left(x(i_0 + i) - x(i_0)\right)^2 , \tag{8.3}$$

where N is the total number of time steps during a simulation with duration T. For later times the statistics for the MSD gets poorer and because of an increasing diffusion in z-direction with time that induces artifacts, Figure 8.8 depicts only MSDs in lateral direction for $T \leq 0.25$ ns. Besides the displacement of the entire polymer film's center of mass (first column), the polymer chain's MSD with respect to the films MSD is computed layer by layer. The bottom layer is named L1, it is chosen as a thin layer inside and close to the substrate, with an extension of up to 15 Å above the respective surface. Depending on the system, the following intermediate layer L2 has a thickness between 11-12 Å. Layer L3 describes the rest of the film (see Fig. 8.8). A chain is classified to a certain layer with reference to the z-position of its center of mass at the given time-step. A single data point is always the result of an averaging over all respective chains, in a layer. The MSD of the polymer film's center of mass is not equal to the sum of the MSDs of the polymer chains of all three layers.

Figure 8.8 shows the MSD at 350 K for the DTSeq, OTSeq as well as for the SiOeq system. For the time frame considered, the polymer film shows the highest MSD in lateral direction on the DTSeq substrate, followed by the OTSeq system, whereas the MSD in SiOeq is clearly the lowest. A closer look reveals that on DTSeq also the displacement of the chains in L1 is the highest. In this layer, the chain's mobility on the OTSeq substrate is comparable to SiOeq. In total, the displacement in L1 is higher than in L2, where all MSDs of all three systems are comparable, only the MSD on SiOeq is slightly above that on silane systems. In L3, the overall MSD increases again, but no difference between the system is visible anymore, meaning that the PS film on SiOeq and OTSeq is able the reach the high MSD-values as on DTSeq at the free interface, which is not the case close to the substrate.

Ignoring the very first picoseconds, the MSD seems to follow a normal diffusive behavior: For times greater than 0.1 ns a simple fit of a straight line delivers the diffusion constant D

$$MSD = 2\delta D\tau, \tag{8.4}$$

where δ is the number of involved dimensions. To get a reasonable slope, the actual fit is done with a polynomial of first degree, where the y-intercept is allowed to be slightly different than 0 [Mic2010]. Figure 8.9 shows the fits and the values of D for the summed up lateral diffusion (x+y) in the three presented systems at 350 K. The diffusion constant of the film's MSD is the highest on the DTSeq substrate followed by OTSeq, and SiOeq at last. The layer by layer analysis of the polymer chains inside the film reveals a similar

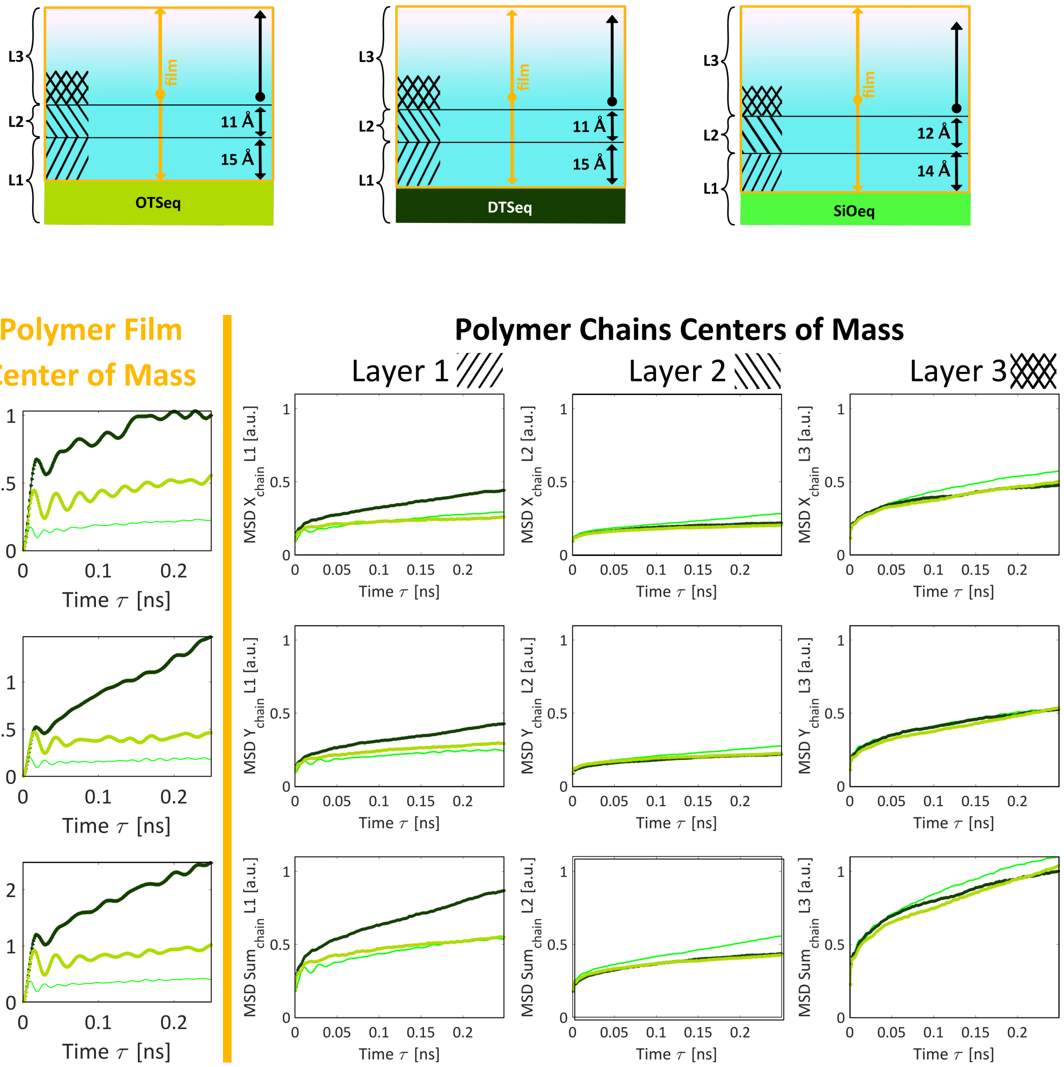

Figure 8.8: Mean square displacement of the polystyrene in the DTSeq (dark green), OTSeq (yellow green) and SiOeq (green) system, at 350 K. The first row depicts displacements in x-direction, the second in y-direction and the third the sum of x and y. The first column shows the displacement of the entire film (film, marked yellow), the second column only the displacements of polymer chains in a layer L1 close to the substrate, the third column in an intermediate layer L2, and the fourth column depicts the displacement in L3, which is the rest of the film above L2 (see Fig. 8.8).

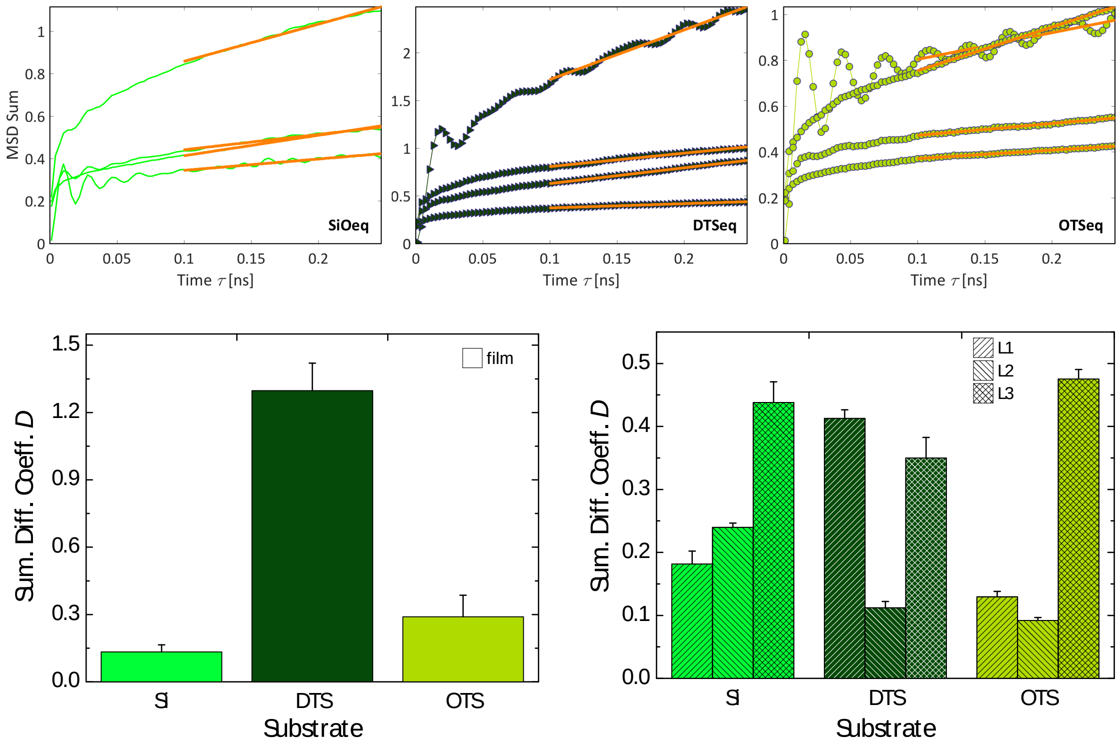

Figure 8.9: Fit values for the diffusion coefficient D of the summed up lateral (x+y) MSD of the polystyrene film's center of mass (film) and layer by layer (L1: close to the substrate, L2: intermediate, L3: rest of polymer film) on DTSeq (triangles, dark green), OTSeq (circles, yellow green), and SiOeq (stars, green), at 350 K.

picture to what the raw data indicates: For the layer next to the interface L1, D is the highest on the DTSeq substrate. In this system, values are comparable with the level of L3, no matter on which surface. For Layer 2, the diffusion constants of DTSeq and OTSeq are on the same level and lower than in L1, only the diffusion constant on SiOeq is higher in L2 than in L1. Judging from these readings, the diffusion in L1 on DTSeq is increased up to the level of the free interface (L3), whereas OTSeq and SiOeq stay in L1 and L2 on a lower level. Probably, the advantage at the solid/liquid interface leaves its footprint on the diffusion of the entire film, too – making DTSeq the system with the highest mobility at 350 K.

8.3 Comparing DTSeq and OTSeq by Temperature

The analysis presented before can be applied to all simulated temperatures. Simulations were performed between 600 K and 350 K in steps of 50 K. The highest temperatures are above the melting point of polystyrene and above the thermal stability of a silane SAM, in the experimental system. Therefore, the results of the simulations at 600 K and 550 K

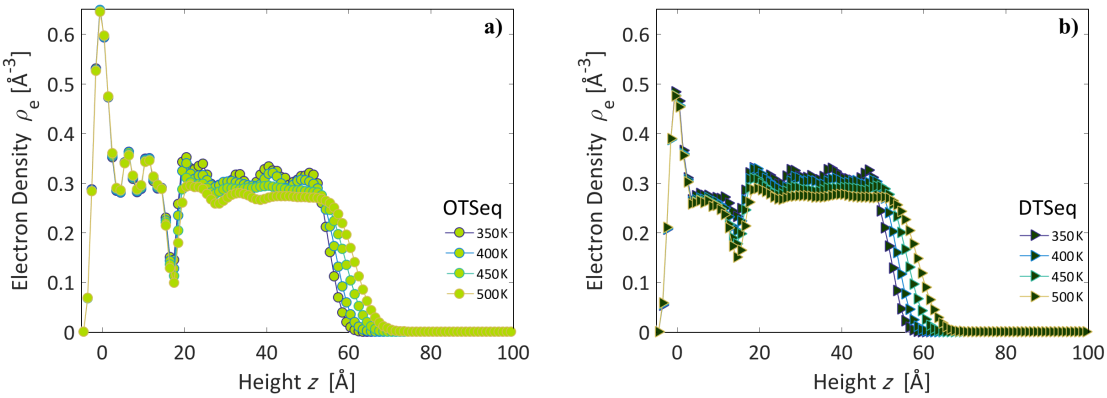

Figure 8.10: Electron density profiles of the **a)** OTSeq (circles) and **b)** DTSeq (triangles) systems, at temperatures from 350 to 500 K (blue to yellow). Data is smoothed by a moving average smoothing with a range of 3 (see Eq. 8.1).

are not directly comparable to experiments, and will not be discussed in the following. The data for 600 K and 550 K can be found in the Appendix. They were used to pave the way for lower temperatures. Dynamics are enhanced at high temperatures, which reduces computing time. The end state of a system at one temperature can be used as the initial state for the next colder one.

Figure 8.10a shows electron densities and depletion zone fits in the same manner as already known from Section 8.2.2, this time for all studied temperatures. Obviously, ρ_e of the polymer film increases with decreasing temperature and the film height shrinks. The direct dependency of the polymer's density on the temperature is a common behavior, and not influenced by the substrate. The OTSeq substrate itself stays rigid throughout the temperature range, whereas the DTSeq substrate shows a trend to reduce its electron density and increase its height with increasing heat (see also Fig. 8.11). As a direct consequence, the tilt angle of the chains inside the DTSeq-SAM decreases with temperature. This could be an effect of the chain's enhanced mobility around their upright position, letting the whole layer appear thicker on average.

8.3.1 Depletion Zone

To compensate the above mentioned temperature induced changes of the polymer films volume and density the interfacial depletion zone (dip) is analyzed with respect to the bulk electron density of the polymer film. A closer look at the fits to the depletion zone (see Fig. 8.12) reveals, that the dip on OTSeq maintains its position (z-position of the minimum), width (full width at half maximum, FWHM) and depth (difference between bulk polymer density and dip minimum), which is not the case on DTSeq. With decreasing temperature the dip on DTSeq gets shallower, broader and the position of

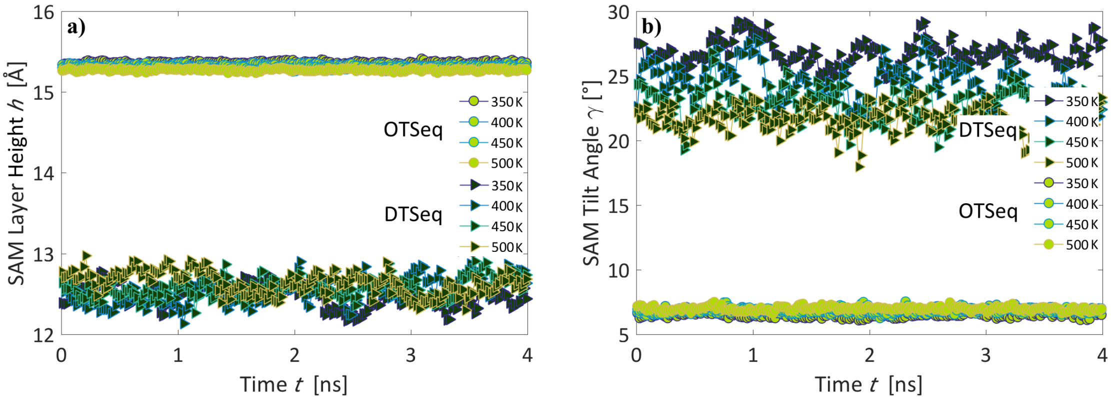

Figure 8.11: a) Averaged SAM layer height h and **b)** mean tilt angle γ of DTSeq (triangles) and OTSeq (circles) as a function of time, at temperatures from 350 K to 500 K (blue to yellow). Every data point represents a spatial mean value averaged over 10 ps (For better visibility, only every second data point is drawn).

the minimum shifts towards lower values. In other words, the interface between polymer and silane is only sharp and 'OTSeq-like' for high temperatures. On one hand, this is because of the decreasing DTSeq-SAM height at low temperatures, but on the other hand, the polymer chains approach closer to the substrate and penetrate the SAM more and more (see Fig. 8.13a and Fig. 8.13b), as already seen in the snapshots of Figure 8.3 at 350 K. At great heat, probably the silanes shake more, giving the polymer chains less chance to slip into the defects of the SAM, so the interface is sharper.

The overall dimensions of the depletion zone are in the same range as measured by XRR [Gut2013]. For the lowest temperature simulated (350 K), the width of the dip is about 2 Å on OTSeq and about 8 Å on DTSeq, see Figure 8.12c. Gutfreund et. al. [Gut2013] reported a layer width of 6.3–6.9 Å on OTS and 4.2–4.8 Å on DTS. Although a direct comparison by number is not meaningful, it is worth mentioning that in the present simulations DTS, shows the wider depletion zone.

8.3.2 Side Groups of Polystyrene

Since polystyrene exhibits the largest slip length of all polymers studied (see PVP and PMMA in Chap. 7) together with a distinctive temperature dependence, it is reasonable to characterize the role of the side group, the phenyl group. Figure 8.13 displays the behavior of the phenyl rings at different temperatures. Their densities follow the same trend as the entire polystyrene film: with increasing temperature the density decreases and the film height increases. On OTSeq, the solid-liquid interface stays constant, whereas on DTSeq it roughens with decreasing temperature. The interface between DTSeq and PS film is not as sharp as the interface between OTSeq and PS. A small, but significant number of side groups appear at z-heights of the SAM. Rings at this height

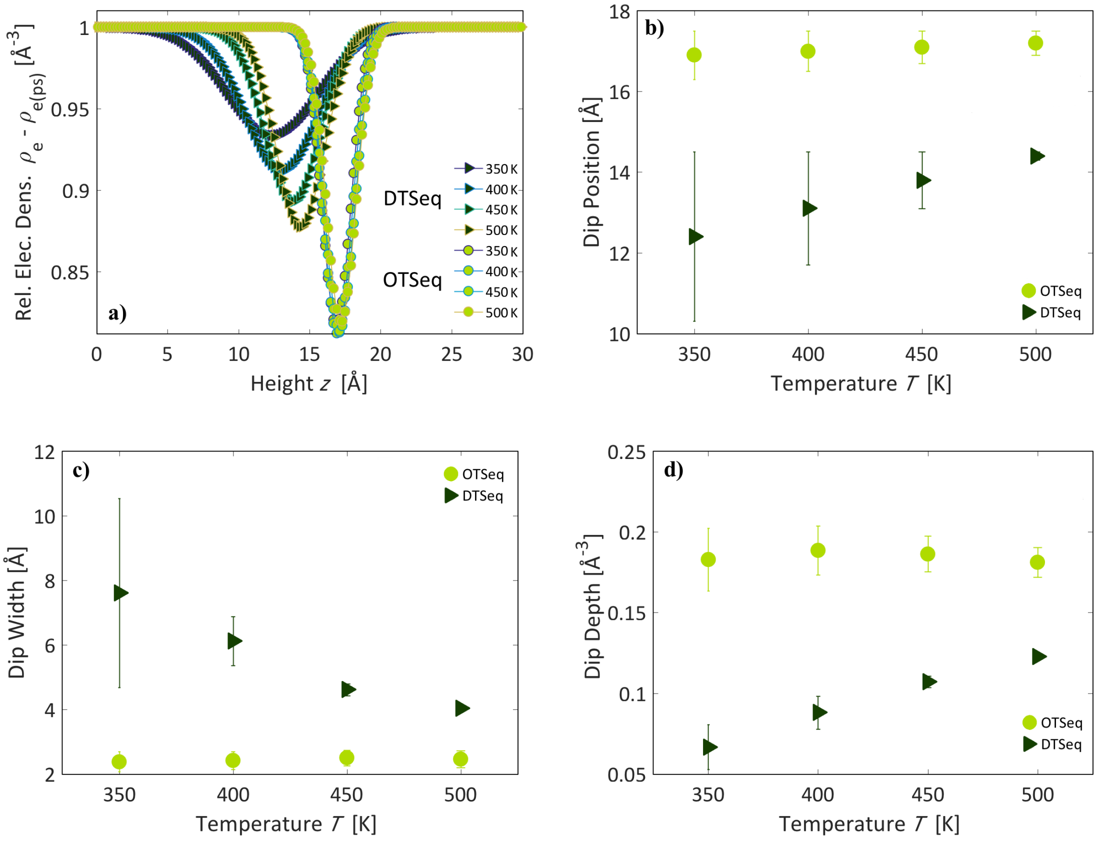

Figure 8.12: Fits of the of the interfacial electron density depletion zone (dip) between polymer and substrate (DTSeq: triangles; OTSeq: circles), normalized to the mean electron density of the polystyrene film, at temperatures from 350 K to 500 K (blue to yellow); Absolute position (z-position of the minimum) of the dip as function of temperature; Width (full width at half maximum) of the interfacial electron density depletion zone between substrate and polymer film as function of temperature; Electron density drop relative to bulk polymer as function of temperature.

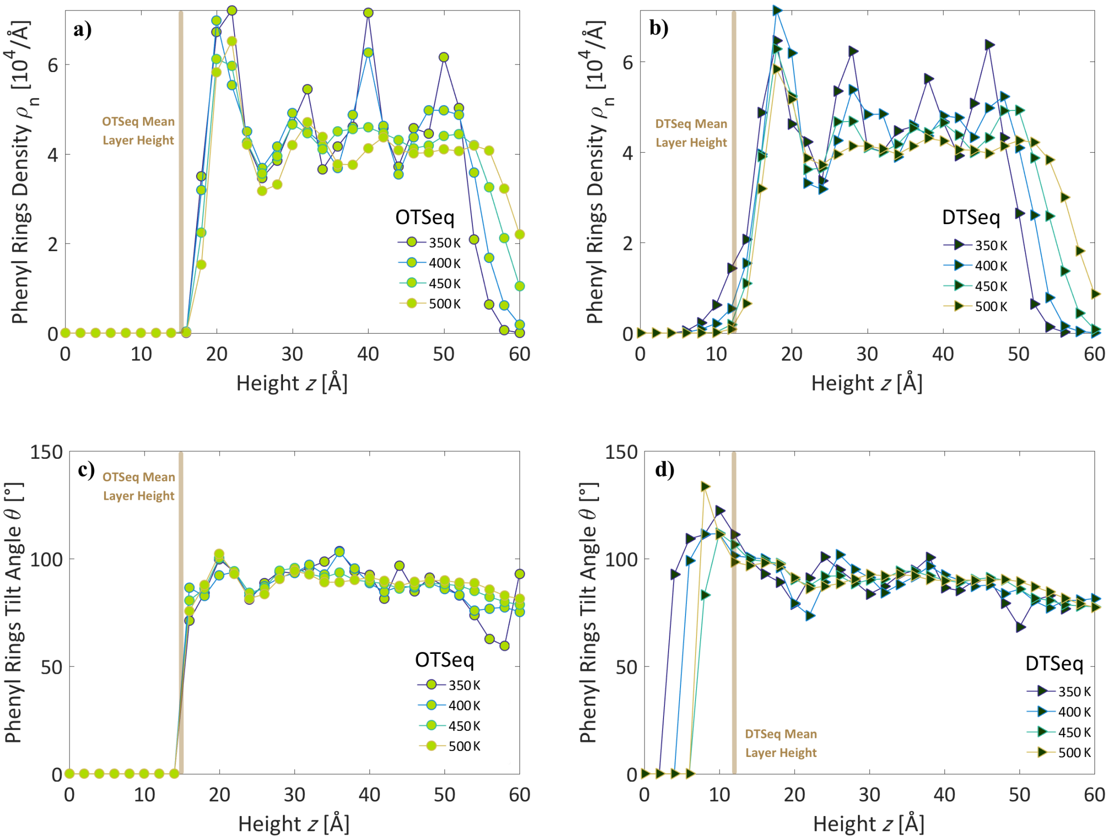

Figure 8.13: Time averaged mass density ρ_n of phenyl rings on **a)** DTSeq (triangles) and **b)** OTSeq (circles), at temperatures from 350 K to 500 K (blue to yellow). **c)** and **d)** Corresponding time averaged tilt angles θ of phenyl rings. Single data points are averaged over $dz = 2$ Å.

follow the orientation of the silanes, taking tilt values up to 130°, as seen in Figure 8.13d. For the rest of the polymer melt, outside the the DTSeq layer, this influence vanishes and the tilt angle goes back to neutral 90°. Phenyl rings in the OTSeq system show no exceptional behavior at all, see Figure 8.13c. For both systems the density inside the bulk polymer fluctuates with a wave-length of 8 Å (see also mass density of the entire film in Fig. 8.3). The amplitude of these fluctuations decreases with increasing temperature. Yet, the meaning of this observation was not further studied.

8.3.3 Mobility and Mean Square Displacement

Figure 8.14 focuses on the temperature dependency of the diffusion coefficient D of the lateral MSD, for temperatures below 550 K, since a presentation of the raw data for the

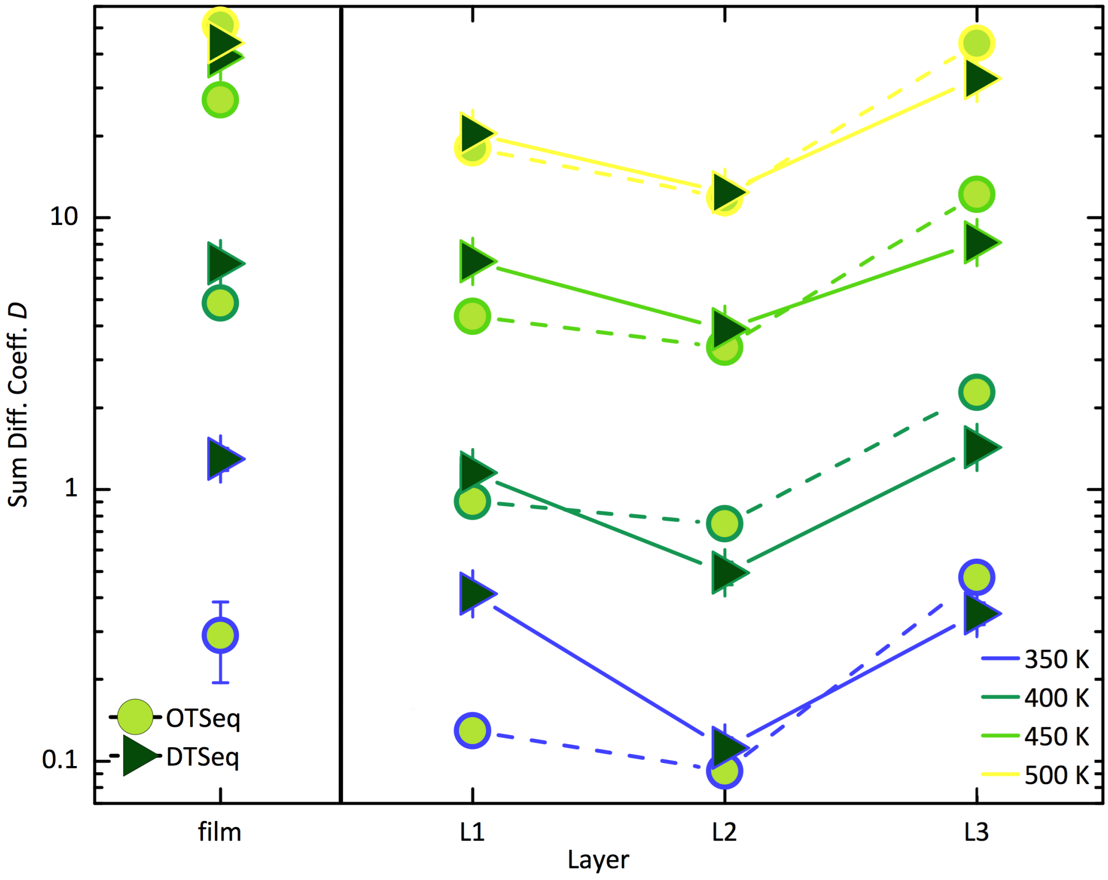

Figure 8.14: Fit values for diffusion coefficient D of the summed up lateral (x+y) MSD of the polystyrene film's center of mass (film) and of the polymer chains layer by layer (L1: close to the substrate, L2: intermediate, L3: rest of polymer film) on DTSeq (triangles, solid line) and OTSeq (circles, dashed line). Colors represent temperatures from 350 K to 500 K (blue to yellow), lines are drawn to guide the eye.

studied MSDs (as shown in Figure 8.8) would go beyond the scope of this thesis. MSD data on SiOeq, DTSeq, and OTSeq for all temperatures simulated, can be found in the Appendix.

In general, the diffusion is strongly dependent on temperature and D grows over a wide scale. For a given temperature, the diffusion coefficient of the polymer film's center of mass is larger on DTSeq than on OTSeq. This is the case for all temperatures shown, from 350 K to 500 K.

The overall temperature dependency of the chain's diffusion coefficient in L1–L3 is in line with the behavior of the entire film: with increasing temperature the diffusion coefficient increases by orders of magnitude. Chains in L3 show the highest diffusion throughout the whole temperature range, followed by L1, whereas those in L2 stay behind. Figure 8.15 emphasizes this, by depicting the D in L1 relative to D in L3. The temperature dependency of D dominates the influences of the substrates. Nevertheless, at lower temperatures, D for polymer chains in L3 is larger on OTSeq than on DTSeq, whereas for L1, the opposite is true. Meaning, the mobility of the polymer chains at the solid/liquid interface, expressed by D in L1, is enhanced on DTSeq compared to OTSeq. In L2, no significant difference is visible between both systems.

In the present case of normal diffusion, the film's diffusion constant is connected to the slip length b [Boc1994, Che2015]. Namely, at a given viscosity η, a higher diffusion coefficient D implies a higher slip length b. Adapting this approach to the studied systems with a free interface, a preliminary connection between D and b can be given

$$D = \frac{k_\mathrm{B}T}{A} \times \frac{h}{3\eta} \times \left(1 + 3\frac{b}{h}\right), \tag{8.5}$$

where A is the area of contact and h the film height. Yet, A and η are not easy to compute and will be part of a future project.

8.4 Discussion

The molecular dynamic simulations presented in this chapter were designed to give insight into the structures and dynamics of a polystyrene melt on a silanized substrate, with special respect to the conformation of the polystyrene chains and their side groups.

With prior knowledge from experimental analysis and detailed MD simulations of the silane SAM, the present simulations implemented the DTS and OTS surface by just using two different grafting densities of DTS-chains and neglecting any supporting silicon substrate. Nevertheless, the known experimental properties of the silane SAMs in terms of roughness, order and tilt angle of its molecules are nicely reproduced; this is a further indication that even under experimental circumstances the difference between OTS and DTS-SAMs arise mainly from their different grafting density.

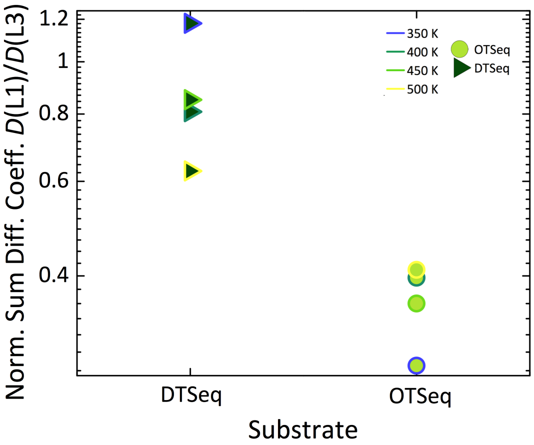

Figure 8.15: Fit values for diffusion coefficient D of the polymer chains in L1 normalized to diffusion coefficient D in L3 (L1: close to the substrate, L3: next to air interface) on DTSeq (triangles) and OTSeq (circles). Colors represent temperatures from 350 K to 500 K (blue to yellow).

Electron density profiles of the simulated polystyrene film on the OTS-like and DTS-like substrates show a similar shape as seen in the former XRR studies [Gut2013] and in Section 7.4, with a characteristic electron depletion zone in the sub-nanometer range between the respective silane and the polystyrene bulk. The reason for this dip in electron density is a reduced mass density of the polystyrene at the interface. Particularly distinctive is this gap on the OTS-like substrate. Additionally, the layer is that dense that the polystyrene has no chance to penetrate. For the lower density substrate, DTSeq, the interface is rougher, the depletion zone is less pronounced and the parts of polystyrene mix with the silane, especially at sites of low silane density. As a direct consequence, a few side groups of the polystyrene that are in direct contact with the silane adapt their tilt angle, but this is not true for the rest of the polymer film. An influence of the substrate to the ordering of the phenyl rings at the entire interface is not visible in the simulations. Notably, on OTSeq the phenyl rings have no special tilt in the vicinity of the substrate, so they are not ordered and upright standing.

Judging from the MSD data, the mobility of the polystyrene is enhanced in the DTSeq system, especially in the very first liquid layer, compared to OTSeq, for temperatures comparable to experimental situations. Knowing, that for a given viscosity the diffusion coefficient is connected to the slip length, the higher diffusion coefficient of the film on DTSeq at low temperatures indicates an enhanced slip in this system compared to OTSeq. Also the slip at the interface (L1) should be higher on the DTSeq substrate. Yet, a measure of the slip length can not be given until the corresponding computations to yield the viscosity or the contact area are completed. However, already this qualitative observation of an overall enhanced mobility in the DTSeq system are in agreement with the experimental situation. Moreover, the diffusion of the chains on DTSeq differs from OTSeq especially at the solid/liquid interface (L1)

The reason of the enhanced mobility remains unclear, especially keeping in mind that polystyrene penetrates the DTSeq substrate occasionally. It should be pointed out, that the polymer is not trapped in the SAM, it can slip into and out of sites of low silane density. It could be possible that, due to this behavior the polymer is sporadically anchored at the solid/liquid interface and so parts of the polymer act as a crust on which the rest of the polymer moves onwards. A scenario similar to the image of apparent slip, where the very last molecular layer at the interface has no velocity, but the liquid's flow profile leaves the impression of a slip length.

8.5 Outlook

The presented analysis focused on the structural data and order effects. A basic impression of the dynamics of the system was only given by MSD data. Yet, the simulations are designed to enable the computation of the friction coefficient via the Green-Kubo-Approach and combine the data with the viscosity to calculate the slip length. The computing and evaluation for this data are on the way.

Although a stacking of the phenyl rings is not obvious in the present data, it cannot be ruled out completely since the relative orientation between neighboring rings is not analyzed yet. Additionally, the quite short chains of 10 monomer units could be too short to enable the phenyl rings to order, since side effects are too prominent (low ratio of phenyl rings at the ends of the chain to those surrounded by phenyl rings). For this reason simulations for polystyrene with 20 monomer units are planned.

Having now the basic setup for simulating our polymers and substrates, it is possible to modify the simulations in numerous ways: It is easy to implement isotactic, instead of atactic polystyrene to accompany the experimental study presented in Chapter 9; Simulations are running.

Beyond that, there is the possibility of simulating polystyrene on a mixed DTS-OTS-like substrate, or exchanging the polymer with PVP or PMMA.

9 Isotactic Polystyrene

Experiments on differently structured hydrophobic substrates, like OTS and DTS prepared on silicon and quartz, as well as the Teflon® surfaces of PTFE AF, clearly demonstrate that the substrate plays a key role to enable strong slip. Yet, the polymer itself is another player. The study on PVP and PMMA (see Chap. 7) made clear, that changing the nature of the polymer slightly (e.g. in case of PVP, where in comparison to PS only one C in the phenyl ring is replaced by one N-atom) dramatically changes the slip length. So far, all polymers used for this work are atactic, which means that their side groups are randomly distributed along the chain. If the very strong slippage of polystyrene on DTS really depends on an ordering/stacking effect of the phenyl rings (π-π-stacking [Nak2014, Gut2013, Cla2001, Gau2000, Sug1997, Chi1996]), per-order of their tactility should have an impact on slip.

In isotactic polystyrene (iPS), all side groups point in the same direction with respect to the backbone of the chain. A recent dewetting study of isotactic (90% isotactic content) and atactic polystyrene of a molecular weight higher than 400 kg/mol (iPS: $M_\mathrm{w} = 400\,\mathrm{kg/mol}$, $PDI = 2.8$; aPS: $M_\mathrm{w} = 542\,\mathrm{kg/mol}$, $PDI = 1.04$) on polydimethylsiloxane and at temperatures above 180 °C, suggest a transient cooperative motion in a crystallizable polymer melt that greatly enhances the viscosity [Cha2016].

The experiments presented in the following should test the hypothesis if a blend of isotactic/atactic polystyrene slips differently as its atactic companion, when prepared under the very same conditions. Since crystallization is very likely in blends with isotactic proportions [Oka1994, Wen1990, War1977], only small amounts of isotactic content are used. The blend is mixed from two, by molecular weight (M_w) and polydispersity (PDI), comparable grades of atactic and isotactic polystyrene. To keep experiments within usual conditions and prevent crystallization as much as possible, blends in the range of the critical molecular weight of entanglements M_c are used (see Sec. 4.1), and temperatures are held just above 100 °C. This chapter gives a brief introduction into the project and shows first data. The complete analysis and further results will be part of Kirstin Kochems' bachelor thesis, that was supervised in the context of this work.

9.1 Experimental Details

9.1.1 Polymers

Isotactic polystyrene is rare on the market and thus very expansive. Most of the commercially available isotactic polystyrenes feature very high molecular weights of several hundreds of kilogram per mole. Since this thesis focuses on slip of polymeric melts below the critical molecular weight, those polymers are not suitable. Therefore, the choice felt on iPS (99% isotactic content) with a number averaged molecular weight (M_n, see Section 4.1) of 31.0 kg/mol and a *PDI* of 3.48 (Polymer Source Inc., Montreal, Canada).

The broad molecular weight distribution indicates that the polymer grade contains chains below and above polystyrene's M_c. Hence, experiments and slip lengths are not directly comparable to dewetting experiments presented so far. To get a suitable atactic reference system, a broad atactic polymer standard with a similar molecular weight distribution (psb45k, $M_n = 20\,\mathrm{kg/mol}$, $PDI = 2.35$) was used (PSS Polymer Standards Service GmbH, Mainz, Germany), termed PSb in the following. All iPS experiments presented in the following were always accompanied by PSb experiments under the same experimental conditions and serve as a reference.

9.1.2 Polymer Solutions

A precondition for the preparation of polymer films by spin coating is to dissolve the polymer powder in a good solvent. Although the manufacturer lists tetrahydrofuran (THF) and chloroform as solvents for iPS, it was not possible to dissolve the polymer completely in any of the two. Even an extended shaking or heating of the solution was not successful, the solution remained somewhat milky (THF solution was less milky than the chloroform solution), which is a sign for undissolved polymer. The remaining residues in the solution were filtered using a PTFE syringe filter with a pore size of 0.45 µm.

To analyze which parts of iPS are solved in THF, gel permeation chromatography (GPC) [Moo1964, Lat1956] was used (see Fig. 9.1)[1]. According to this measurement, the dissolved polymer exhibits $M_\mathrm{n} = 37.025\,\mathrm{kg/mol}$ and $M_\mathrm{w} = 124.14\,\mathrm{kg/mol}$, which results in a $PDI = 3.35$, which is slightly lower than the value given by the manufacturer and is assigned to the filtering. Figure 9.1 displays the molar mass distribution of PSb according to the manufacturer's data sheet [PSS2013] in comparison to iPS after filtration.

Though the distributions do not match perfectly, PSb covers a wide range of the iPS' GPC profile, with the result that slip length deviations due to entanglements [Fet2006a, Bäu2009a] should be minimized. Therefore, a presumed decisive effect of ordering side groups should be visible.

---

[1] GPC measurements were done with the help of Blandine Boßmann at the group of Prof. Dr. Gerhard Wenz, Saarland University.

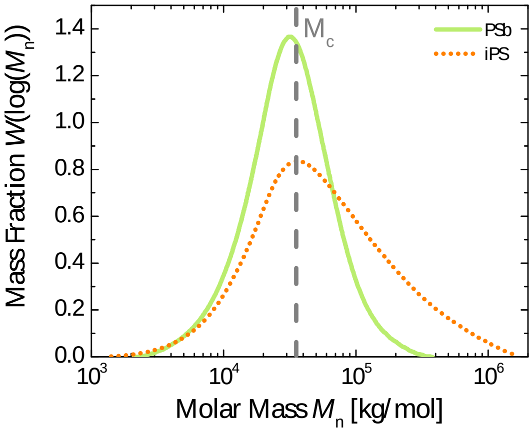

Figure 9.1: Molar mass distribution of PSb (solid green) (data taken from manufacturer's data sheet [PSS2013]) and iPS (dotted orange) dissolved in THF, measured by gel permeation chromatography (GPC), after filtering. Dashed gray line marks the critical molecular weight of PS.

9.1.3 Film Preparation

The process of dewetting a film of pure iPS stops at a relatively early state, probably because of crystallization. To prevent this, the iPS solution (28 mg/ml) was mixed with PSb solution (26 mg/ml) in a low ratio of 5% iPS (5iPS) and a higher ratio of 25% iPS (25iPS) to PSb.

Spin coating films from a THF solution results in a sinusodial-like fluctuating film thickness. The phenomenon is known and often seen for very good solvents with high vapor pressure [Jac2015]. To improve the smoothness of the films, THF was exchanged by toluene. To do so, the prepared THF solution was doubled up with toluene and annealed to 55 °C for 12 h. After that time, the volume of the solution had reduced to its initial value. Due to the different boiling points of THF (66 °C) and toluene (111 °C), it can be assumed that the remaining liquid is mostly toluene.

Spin coating the prepared solutions at 3700 min^{-1} onto freshly cleaved mica sheets, results in homogeneous films with thicknesses of about 115(5) nm. Afterwards, the films were transfered via floating onto ultra-pure water to the final OTS, respectively DTS substrates.

9.1.4 Experimental Realization

Experiments were carried out at 120 °C, without any pre-anealing. At this temperature crystallization is not excluded, but should be very slow [Boo1968]. Rapid crystallization is seen at temperatures between 180-200 °C [Wyp2016]. To monitor changes of the liquid's state, dewetting experiments in this study were done while scanning the film by AFM (Bruker Dimension Icon, see Section 3.3) *in situ*. Crystallization should lead to a larger E-modul of the film and increase the roughness. Both parameters can be very well captured in PeakForce QNM® mode (see Sec. 3.3). The data presented in the following originates exclusively from experiments with 5iPS and 25iPS where the film did not change these AFM-monitored properties during the dewetting process. For that reason, crystallization is assumed to be improbable.

9.2 First Results

9.2.1 Low Ratios of Isotactic Content: PSb and 5iPS

Figure 9.2 depicts rim profiles of PSb and of 5iPS on DTS and OTS growing in time. The pictures are taken *in situ*, meaning that the sample was kept at 120 °C using a heatable AFM stage and tip. Scanning was carried out with low forces and feedback loop parameters that ensure the tip does not influence the liquid film.

At early stages, the rim profile of PSb on DTS (see Fig. 9.2a) shows a clear monotonic decay into the undisturbed film. With time, the asymmetry of the profile decreases, and the decay enters a transition between monotonic and oscillatory shape. The rim was monitored until a time of 289 min (relative to the time when the sample was put on the preheated stage), which corresponds to a hole radius of about 22 µm (see Fig. 9.3a). Former experiments, as seen in Chapter 6 and Chapter 7, were stopped at a radius of 12 µm. PSb on DTS reaches this value after 100 min.

5iPS on DTS reaches 12 µm after 100 min, as well. Its speed of dewetting is roughly comparable to PSb, over the entire range of the experiment. Figure 9.3 shows that the hole in 5iPS has reached a radius of 20 µm after 226 min. Overall, the time evolution of the rim is similar to pure PSb films on DTS. The profile – depicted in Figure 9.2 bottom left – starts clearly asymmetric in the beginning, but changes to a more symmetric shape, in the end.

From the start on, PSb on OTS shows a less pronounced monotonic – almost oscillatory – profile as on DTS, indicating a lower slip length (see Fig. 9.2 top right). This observation is in line with the behavior of polystyrene on silanes, already discussed in previous chapters. With time, the rim evolves a recognizable oscillatory shape. At the end of the experiment, after 826 min the rim's decay exhibits a shallow, but clear dip. The hole has reached a radius of almost 20 µm, at that time. The reference width of 12 µm is reached after 390 min. With that, the dewetting process of PSb is clearly slower on OTS than on DTS.

5iPS reached a radius of 12 µm after 340 min. For comparable times, the rim profile is similar to PSb on OTS, with a slight tendency towards a steeper decay at the wet side. The hole was monitored until a radius of 18 µm and 598 min. At this stage, the rim's

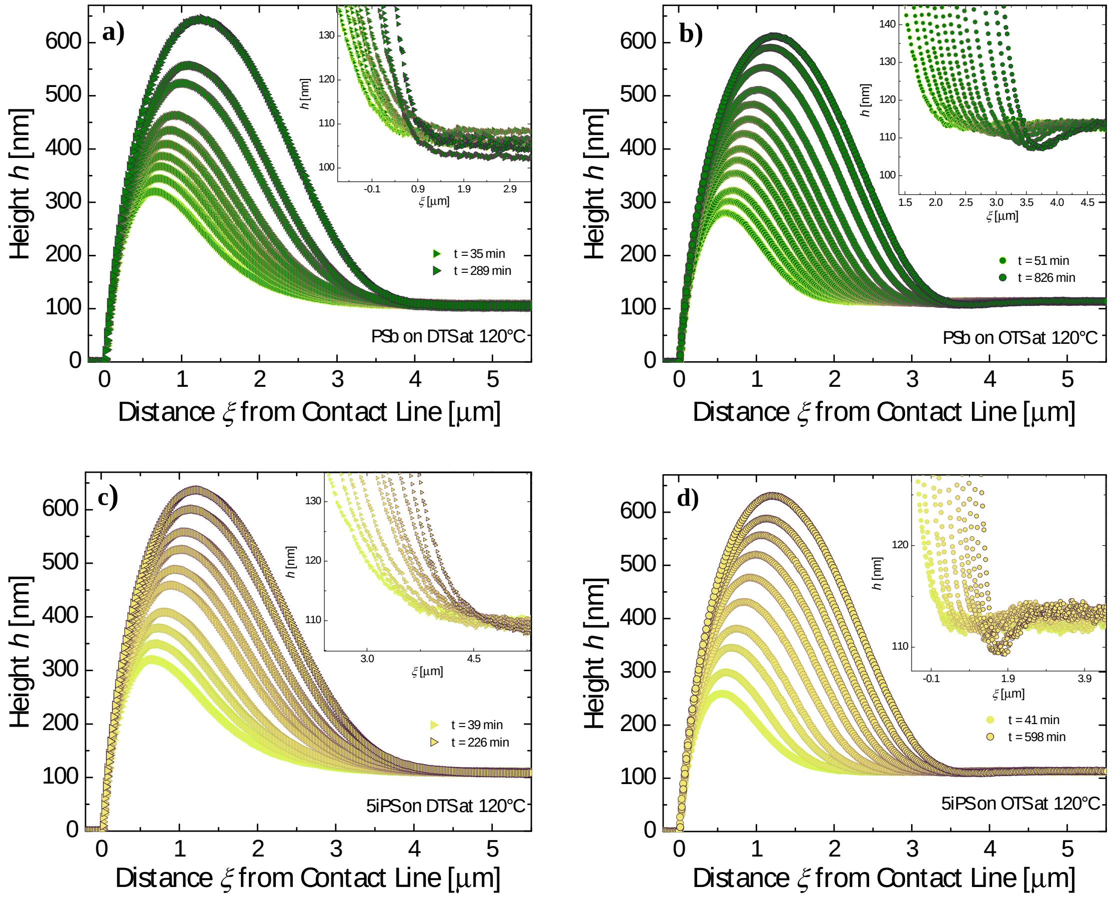

Figure 9.2: Time evolution of rim profiles in dewetting PSb (upper row) and 5iPS (lower row) films on DTS (left column, triangles) and OTS (right column, circles), captured by AFM. Colors from bright do dark indicate the progress in time. The insets depict a zoom to the rim's decay into the undisturbed film. The three-phase contact-line is shifted to 0.

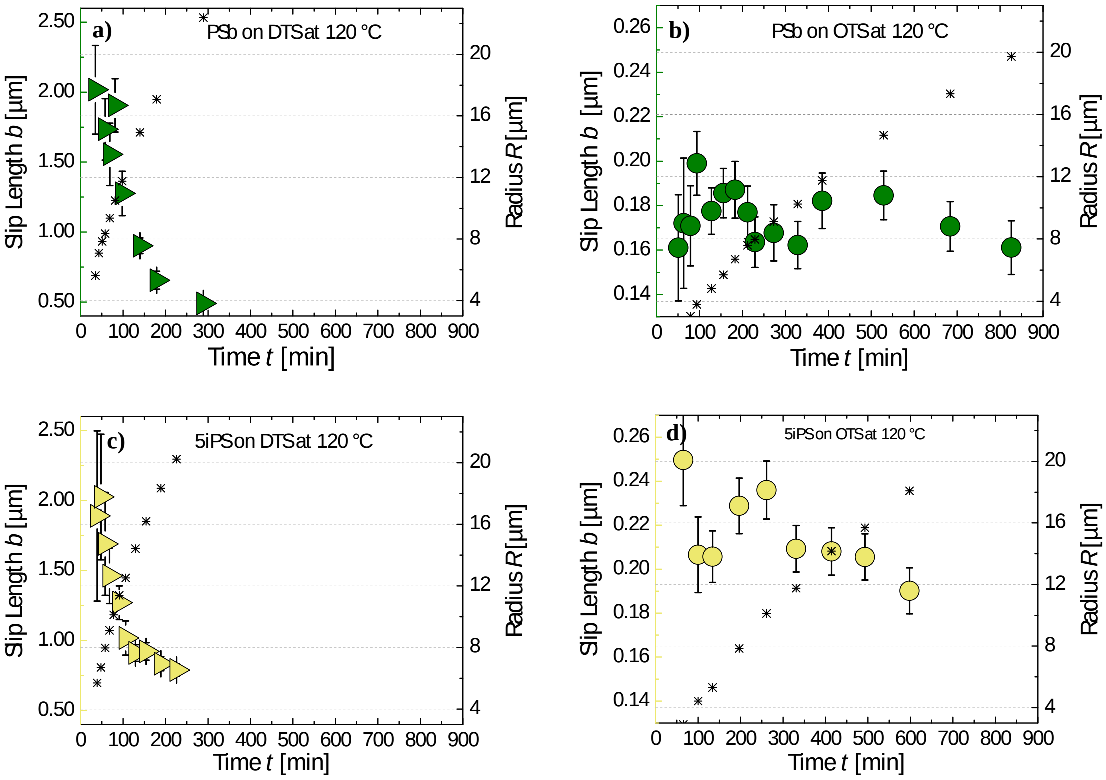

Figure 9.3: Slip lengths b and hole radius R as a function of time t. Slip lengths are determined by rim profile analysis and corresponds to the AFM pictures given in Figure 9.2: PSb (upper row, green) and 5iPS (lower row, yellow) films on DTS (left column, triangles) and OTS (right column, circles). The corresponding hole radii (black stars) were measured optically while scanning the rim with the help of the AFM's integrated optics. The time 0 denotes the instant when the sample was put on the preheated stage.

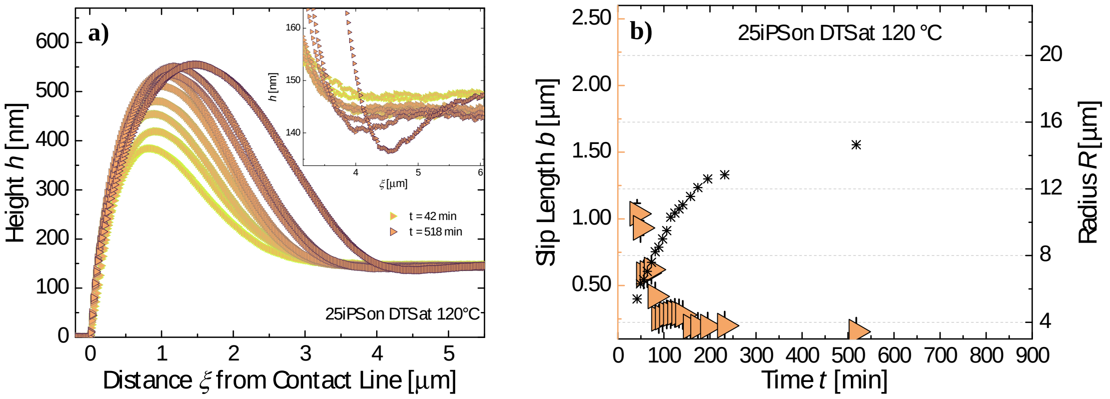

Figure 9.4: a) Time evolution of rim profiles in dewetting 25iPS films on DTS, captured by AFM. Colors from bright do dark indicate the progress in time. The three-phase contact-line is shifted to 0. The insets depicts a zoom to the rim's decay into the undisturbed film. **b)** Corresponding hole radius R (black stars) and lip length b (triangles) as a function of time t. Slip length is determined by rim profile analysis, hole radii were measured optically while scanning the rim with the help of the AFM's integrated optics. The time 0 denotes the instant when the sample was put on the preheated stage.

shape is clearly oscillatory, featuring a pronounced dip that indicates a low slip length, as at the beginning of the experiment.

Besides the already described kinetics of the hole growth, Figure 9.3 depicts also the slip length as a function of time, determined by analyzing each rim profile. For details of the analysis see Section 2.4.2. If the rim exhibits a shape that is not clearly monotonic or oscillatory (for example in the late stage of PSb on DTS), both models were tested and the best fit is used. Usually the oscillatory model gives the best results – even for profiles without a dip – up to the stage at which the shape is clearly monotonic and asymmetric over a wide distance ξ, as for example the early stages of PSb on DTS.

The slip length decreases for all observed systems with time. On DTS, PSb and 5iPS films start with slip lengths in the range of 2-2.5 µm which soon drop below 1 µm, after 130 min. In contrast to that, the slip lengths on OTS stay constant, even though on a roughly ten times lower scale. Slip lengths are in the range of 0.16-0.2 µm for 5iPS, and 0.19-0.25 µm for PSb.

9.2.2 Higher Ratios of Isotactic Content: 25iPS

A striking difference in slip length between PSb and 5iPS was not visible. Experiments with 25iPS represent the upper limit, above which crystallization wins the game. For that reason, Figure 9.4 shows only results up until a radius of 15 µm. The hole cannot reach values of 20 µm, since the speed of dewetting decreases dramatically after 200 s. Also, the rim profile stops its monotonic growth and starts to broaden instead of growing in height and width simultaneously (see rim profile for 518 min). Therefore, values for long times and big radii have to be considered with caution.

Nevertheless, in the reference range between 0-12 µm, the experiment reveals a familiar dewetting speed, the rim profile grows monotonically and the roughness and elasticity show no hints for crystallization (data not shown). Slip length starts at about 1 µm and drops down to 0.25 µm after 90 min. It stays at this value until the hole has a radius of 12 µm, after 200 min.

9.2.3 Synopsis

Figure 9.5 depicts the same data as Figure 9.3, but as a function of the hole radius. The figure focuses on the direct comparison of PSb, 5iPS and 25iPS in the same scale, and over a radius from 2 to 13 µm. So values at about 12 µm can be compared with results presented in previous chapters, since the accumulated volume in the rim matches. On DTS, PSb and 5iPS share – within the error – the same values over the depicted hole widths, whereas on OTS, slip lengths of PSb stay consistently slightly below the ones of 5iPS.

In contrast to that 25iPS on DTS starts with only 1 µm clearly below the level of PSb and 5iPS. In the course of the experiments, the slip lengths decrease very quickly to the level of PSb and 5iPS films on OTS, and stay at about 0.25 µm until the end of the depicted range.

On OTS, the error of each measurement and the scatter of the data points are smaller than on DTS, which is not due to the observed system, but to the method of analysis. Oscillatory profiles can be fitted more accurately than monotonic profiles. For example, choosing the range of the fit can be a problem, since the decay to the undisturbed film height is continuously and thus the choice of the reference hight contains errors. Moreover, in some cases, the decay is not a clear superposition of two dissociable exponential functions, with the result that the damping coefficients are indistinguishable (see Eq. 2.17).

9.3 Discussion

The initial aim of this study was to test the hypothesis if ordered phenyl rings play a major role for the slip boundary condition. For this purpose isotactic polystyrene was mixed with atactic polystyrene to see if the pre-ordered phenyl rings of the isotactic polystyrene influence slippage. The experimental realization of this idea was not easy, since pure isotactic polystyrene crystallizes, making the usual dewetting experiments impossible. Eventually, amounts of 5%-25% of iPS turned out to be experimentally controllable and crystallization is, within the considered time frame, not noticeable. Polymer films with higher amounts of isotactic content, as for example 50%, stop their dewetting very early,

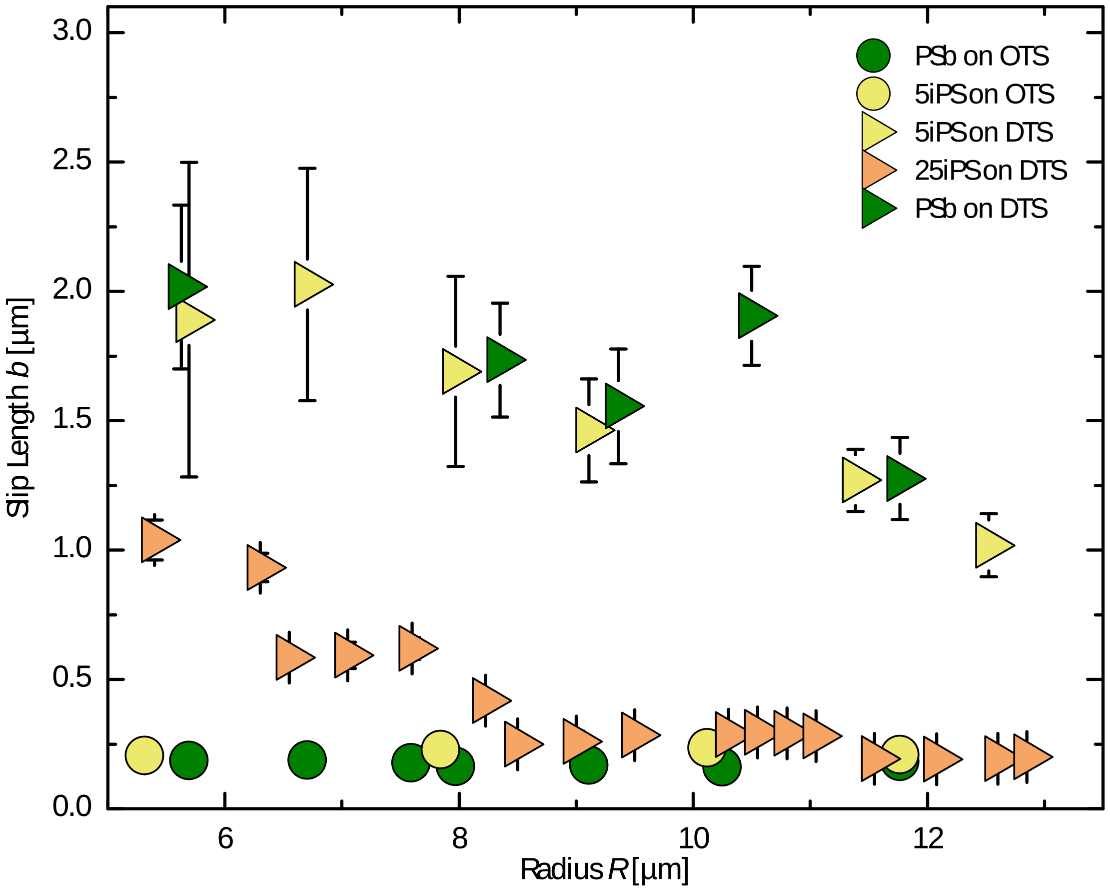

Figure 9.5: Slip length as a function of radius for PSb (green), 5iPS (yellow) and 25iPS (orange) on OTS (circles) and DTS (triangles) at 120 °C.

probably because of crystallization. However, adding only low ratios of iPS to PSb has no visible effect on the slip length. Within the scatter of the measurement, PSb and 5iPS show comparable slip lengths on DTS and OTS. A distinctive difference between purely atactic polystyrene and partially isotactic is not visible, neither at the beginning nor at the reference radius. However, the scatter from one snapshot of the rim to the next one, and the uncertainty of the individual measurement could hide a small systematic difference. Yet, 25iPS on DTS differs remarkably, showing roughly less than 50% of the slip length of PSb and 5iPS.

The overall range and relative difference of slip length values is in good agreement with known results of monodisperse polystyrene below M_c (see Chap. 6 and Chap. 7) and slightly above [Fet2006a], as well as recently published data for bi-disperse melts [Sab2015]. However, a direct comparison is not appropriate, since PSb, 5iPS and 25iPS are highly polydisperse.

The decrease in slip lengths on DTS with time is unusual: In experiments with monodisperse polystyrene, the rim maintained a self-similar shape [Bäu2012a] and the slip length stayed constant. For long times, this could be an effect of the polydispersity, meaning that with time short and long chains within the liquid reptate differently, with the result of a decreasing slip length. On OTS, the effect could be hidden since the slip values are already from the very beginning at a lower level than the final DTS values.

The fact that adding some iPS to a PS melt does not increase the slip length is not a falsification of the initial hypothesis, since we cannot exclude that iPS simply demixes from the atactic PS. However, if π-π-stacking played a prominent role, demixing would very likely not take place. In this respect, the experiments with iPS weaken the π-π-stacking hypothesis significantly.

9.4 Outlook

The presented data give a first impression into an ongoing research project embedded into Kirstin Kochem's bachelor's thesis. A detailed presentation and discussion of the experimental difficulties of this work, including the controlled production of iPS solutions and films, as well as controlling/preventing crystallization, will be part of future publications.

Supplementary experiments to validate the presented results are on the way. Besides the shown 5iPS and 25iPS, experiments with intermediate and higher isotactic amount, like 10iPS, 50iPS and 100iPS will be included in future work. With higher isotactic content, crystallization effects come into play, that hinder the dewetting process. To manage that, also different temperatures will be tested. Intermediate ratios between 5iPS and 25iPS could possibly clarify whether there is a monotonic decay in slip length with isotactic content or whether a certain content ratio leads to enhanced slip. This would also help to distinguish ordering effects on a long range (crystallization) from ordering on a short range, like π-π-stacking

Initially, the study was designed to investigate the influence of side group arrangement. Due to the lack of monodisperse isotactic polystyrene, the study was performed with defined polydisperse grades. Some of the observed effects could be a result of this. Therefore future experiments should be divided into two threads:

1. The decline of the slip length with time could be related to the polydispersity. For that reason, comparing *in-situ* captured slip length of PSb with monodisperse, bi-disperse, tri-disperse etc. polymer blends in the same range of molecular weight could shine light on this effect.
2. As soon as available, the project should be repeated with monodisperse isotactic polystyrene below M_c.

10 Summary and Outlook

10.1 Summary

This thesis aimed at the development of a molecular notion to illustrate and explain strong slip in the case of unentangled polymers moving over low-energy surfaces, giving rise for nearly plug flow boundary condition. In the context of this study self-assembled monolayers of silanes as well as Teflon-like surfaces were used as low-energy substrate.

Starting from known results for the slip of thin films of unentangled polystyrene (PS) on dodecytrichlorosilane (DTS, 'short silane': 12 C-atoms in hydrocarbon backbone), octadecyltrichlorosilane (OTS, 'long silane': 18 C-atoms in hydrocarbon backbone) and Teflon® AF1600 (amorphous), which reveal an inexplicably large slip length in the case of DTS, that is an order of magnitude higher than the prepared film thickness, whereas on OTS, the slip length is significantly lower. In both cases, values decrease with increasing temperature. In general, the slip length on both structured substrates is orders of magnitude larger than on the amorphous AF1600 coating, although the latter exhibits the lowest surface energy, with no observable temperature dependence on AF1600. Gutfreund et al. [Gut2013] proposed that the polystyrene's side groups could be sensitive to the order of the underlying SAM, and adopt its ordering. It was speculated that on DTS the interfacial polystyrene phenyl rings are tilted by 30° and on OTS by less than 10° (see Fig. 2.8). Both angles would then correspond to the average tilt of the respective silane SAM.

Having this in mind, next to PS also thin unentangled PMMA and PVP films were studied. PMMA and PVP feature side-groups that are comparable in size to the phenyl rings of PS, yet PVP has an altered electron structure in the side group due to one nitrogen atom instead of a carbon atom, whereas PMMA has no ring-like structured side group. The influence of these side groups on slippage was studied on the basis of dewetting experiments. As described above, the substrate has a major influence on slippage. For this reason, dewetting experiments were also performed for polystyrene on SAMs grown on quartz and on amorphous silicon and should test whether the slip length is influenced by crystalline or on an amorphous arrangement of the bonding sites of the silanes. Accompanying MD simulations of the silane SAMs and polystyrene films on SAMs were designed to reveal a possible molecular structure formation inside the SAMs, polystyrene films, and at the interface between both. Additionally to the structural data, the shown simulations provide information on the mobility of the polymer film and the chains within.

The OTS- and DTS-SAMs that build the basis for the presented and discussed PS, PMMA and PVP slip experiments are specific, in-house produced coatings on top of commercial silicon and quartz wafers. Before use in dewetting experiments their surfaces are well characterized in terms of wettability, roughness and homogeneity. To understand the composition of these substrates, X-ray reflectometry (XRR) measurements are combined with findings resulting from all-atom MD simulations of the SAMs. Judging from these results, OTS is highly ordered and very densely packed (about 4–5 chains per nm^2), which means that the individual silane chains stand upright inside the SAM. However, the DTS-SAMs are slightly rougher and more loosely packed (about 3–4 chains per nm^2), which implies a greater freedom for the individual silane chain, expressed through an averaged tilt angle of about 30° across the SAM. Both results – for OTS- and DTS-SAMs – are in very good agreement with previous experimental observations for SAMs prepared following the very same recipe [Gut2013].

According to XRR, SAMs prepared on crystalline quartz (DTSQ, OTSQ) resemble those on amorphous standard silicon (DTS, OTS). AFM measurements on a micron-scale imply that quartz SAMs are slightly rougher, which is in line with a higher water contact angle hysteresis ($\Delta\theta(\text{OTS, DTS}) < 10^\circ$ vs. $\Delta\theta(\text{OTSQ, DTSQ}) > 14^\circ$). The identified small differences have no striking impact on slippage of PS on top of these surfaces. At 110 °C, PS shows slip lengths of more than 1 µm on DTSQ and DTS, and about 100 µm on OTSQ and OTS. The mean value over several measurements tends to slightly smaller values for OTSQ and DTSQ, as their respective standard silicon counterpart. Yet, this difference is by fare not as obvious as the difference between the two silane types, no matter on which supporting substrate the SAM was grown. A look at the chain densities of quartz and silicon supported SAMs reveals that the most dense SAM (OTSQ) provokes the smallest slip lengths and vice versa (DTS), other surface characteristics like roughness and surface energy have a less dramatic impact on slip. This was already seen by comparing Teflon® AF to fluoridated silane of similar surface energy [McG2014].

Not only the substrate has an important influence, but also the liquid, respectively the polymer itself is crucial. As seen in the case of PVP dewetting at comparable conditions as polystyrene, just a very small variation of the side group's composition has a big impact on the slip behavior. Non-entangled PVP on DTS does not show the huge slip length of PS, and the difference between DTS and OTS is smaller. As compared to PS, only a minor temperature dependence is observable. As compared to PVP, PMMA has no ring-like side group and slip lengths on DTS and OTS are even smaller and no temperature dependence is visible. Remarkably, slip lengths of PVP, PMMA, and PS determined on silane substrates are always above those on the amorphous Teflon-like surfaces. The latter are in the sub-100 nanometer range, and are in accordance with MD simulations [Bar1999].

Except for the system of PS and DTS, where slip lengths of $b > 1$ µm are recorded, slip lengths of all other studied polymers on silane substrates are comparable and cover an intermediate range from about 100 nm to less than 1 µm. Consequently, it can be assumed that the large slip lengths on the silane surfaces are connected to their structured assembly. A closer view reveals that a polymer with a ring-like side group (PS, PVP) slips stronger than a polymer without.

The results of these experiments directed the attention to a possible stacking of phenyl rings due to π-π-interactions (see e.g. [Nak2014]), that – in our case – may lead to an interfacial layer with a slip boundary condition. Considering these findings the following notion is possible: The stacking could be influenced by the tilt angle of self-assembled molecules of the underlying silane substrate. A variation of the side group's electronic structure therefore should affect the stacking and the slip boundary condition. Side groups with no phenyl-like design can order individually with respect to the substrate, but not relative to neighbors (no stacking). On an amorphous substrate, no order is induced at the polymer interface and thus slip is not enhanced.

With this notion in mind, XRR measurements have been initiated to especially reveal possible differences in the characteristics of the electron density directly at the silane/polymer interface. However, the XRR readings of PMMA on DTS are very similar to data of PS films on DTS, and in both cases, an interfacial layer between polymer and SAM has to be assumed to model the data precisely. Hence, identifying the width of the layer with a distinctive tilt angle of phenyl rings, as in the study of Gutfreund et al. is very likely not the only possible interpretation for the reduced interfacial electron density. (Moreover, possible differences between XRR data of the PS and the PMMA on DTS might also be camouflaged by the roughness of the DTS layer.)

To clarify the molecular picture, all-atom MD simulations were designed, with which it should be possible to 'see' the composition and arrangements in the PS/SAM system. Although the SAMs in these simulations are only built of DTS molecules with two different chain densities (OTSeq, DTSeq), they emulate the characteristics of actual DTS and OTS nicely. This is especially visible in the comparison of the electron density profiles with those of XRR measurements and simulations of accurate DTS and OTS, as well as in measures of the averaged tilt angle of the chains. The electron density profiles feature a distinct depletion zone between polymer film and SAM substrate. On OTSeq the zone is sharp, narrow and defined, whereas on DTSeq it is less prominent. The reason for this is that the DTSeq surface is pentetrable for the polystyrene, resulting in a mixed zone of SAM and polymer. In contrast to that, the OTSeq layer is that dense that the polystyrene is not able to penetrate. It even stays away from the SAM, resulting in an interfacial zone where – averaged over time – almost no atoms are present.

The phenyl rings in the simulations show no preferred tilt angle, except of those penetrating the DTSeq SAM. However, the formation of a distinctively ordered phenyl ring 'crust' on top of the SAMs was not observed. Yet, judging from the mean-square-displacement, the polystyrene film is in general more mobile on the DTSeq substrate than on the OTSeq substrate, for simulated temperatures below 550 K. Especially in the vicinity of the DTSeq SAM the mean square displacement of the individual polymer chains is significantly higher than in the case of OTSeq. According to Equation 8.5 the diffusion coefficient of the mean-square-displacement is linked to the slip length. Therefore, the MD-results qualitatively match experimental results for non-entangled PS on DTS and OTS.

To dwell on the role of the phenyl rings stacking experimentally, dewetting experiments with isotactic polystyrene were initiated. The experiments are difficult to handle, since too high ratios of isotactic PS lead to partly crystalline films. Therefore, the isotacic fraction had been gradually reduced. However, preliminary results show that a as soon as the isotactic fraction is low enough to suppress crystallization no significant impact on the slip length is observable.

To conclude, it was possible to characterize the extraordinary, nearly full slip condition of dewetting PS films on DTS in great detail. Any change of parameters in that system (character of the side groups, length of silane chains or the use of other low-energy surfaces) led to smaller slip lengths. It was shown that slippage in the systems studied, strongly depends on the order of the substrate and the 'structure' within the liquid polymer film. The arrangement of the polymer film is sensitive to the order of the adjacent substrate. MD simulations were set up and customized, and were able to mimic the experimentally observed structural and dynamical characteristics. However, an obvious molecular picture that explains all observed data could not be extracted. Yet, for the PS/DTS system on the simulations, an extraordinary enhanced polymer chain mobility directly at the solid/liquid interfaces was detected. This result nicely corroborates preliminary experiments that reveal a reduction in glass transition temperature of thin PS films on DTS. These observations will be a good starting point for future experiments and simulations.

10.2 Outlook

Data from the MD simulations of PS on silanes bear a great potential to deliver more detailed information of the interfacial layer, e.g. revealing the relative arrangements of the phenyl rings along the individual polystyrene chains. It is possible to extract values for the slip length from the simulated systems and compare them to experiments. Furthermore, the existing code now enables the setup of similar simulations easily, as for example isotactic polystyrene, polystyrene with longer chain length or other polymers like PVP or PMMA.

Grazing incidence X-ray measurements [Muk2010] could refine the picture of the interfacial layer between PS and DTS/OTS. Such experiments are prepared, and – if the results are promising – PVP and PMMA should be analyzed with this method, too.

Polystyrene flowing on a SAM that is built of DTS molecules, but has a grafting density of chains comparable to the studied OTS-SAMs, would probably show an OTS-like slip length.

Although a direct evidence for a stacking of the phenyl-rings was not found, and this effect is – judging from the presented simulation data – unlikely, the actual reason for strong slip without entanglements remains unclear. Yet, it has to be the aim of future studies whether a stacking itself is possible in general and if there is a preferred tilt angle of the phenyl groups that improves the stacking.

The MD results concerning the interpenetration of polystyrene and DTS could be a new starting point: Possibly, the penetrating chains act temporarily as a second brush-like surface on which the rest of the film slips stronger. This – somehow autophobic effect – could be a characteristic of the respective polymer, with PS building the top of the line.

Appendix

Supplementary Results of MD Simulations for all Temperatures and Systems

Electron Densities

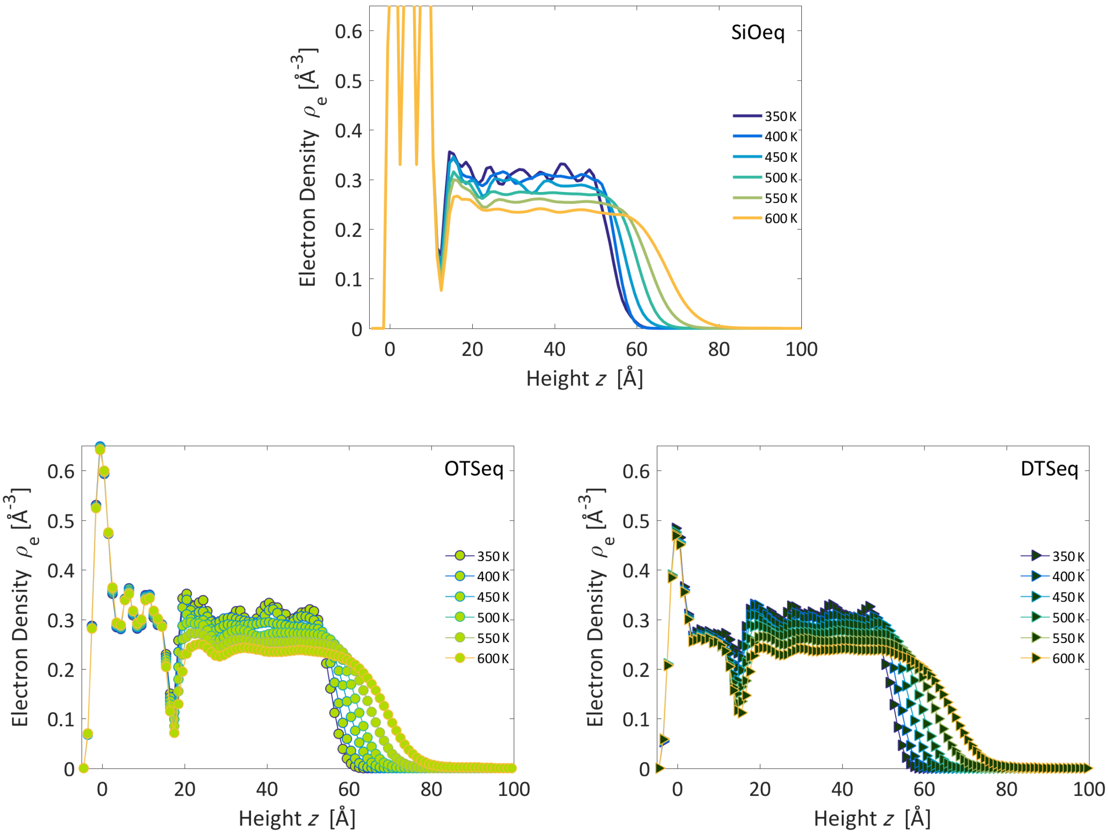

Figure A1: Electron density profile of the SiOeq (solid lines), OTSeq (circles), and DTSeq (triangles) systems, at temperatures from 350 to 600 K (blue to yellow). Data is smoothed by a moving average smoothing with a range of 3 (see Eq. 8.1).

Solid/liquid Interface

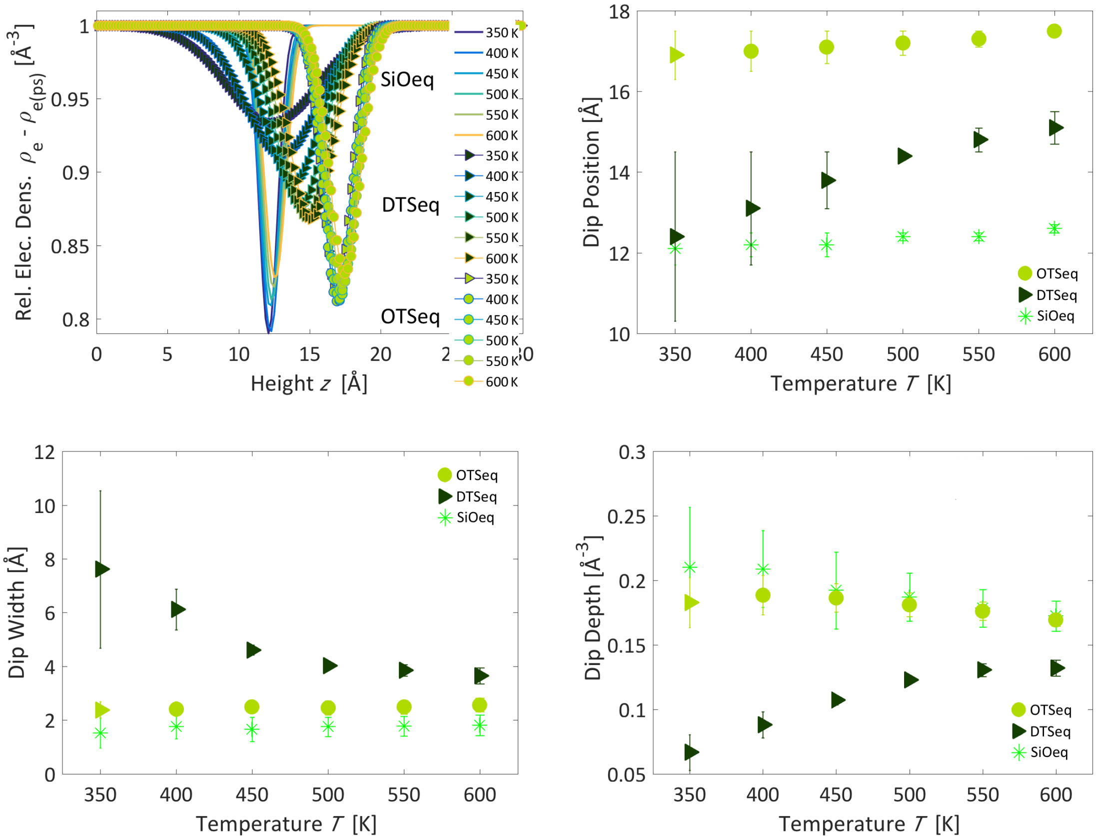

Figure A2: Fits of the dip zone between polymer and substrate (DTSeq: triangles; OTSeq: circles; SiOeq: stars and solid lines), normalized to the mean electron density of the polystyrene film, at temperatures from 350 K to 600 K (blue to yellow); Absolute position (z-position of the minimum) of the dip as function of temperature; Width (full width at half maximum) of the interfacial electron density depletion zone between substrate and polymer film as function of temperature; Electron density drop relative to bulk polymer as function of temperature.

SAM Height & SAM Tilt Angle

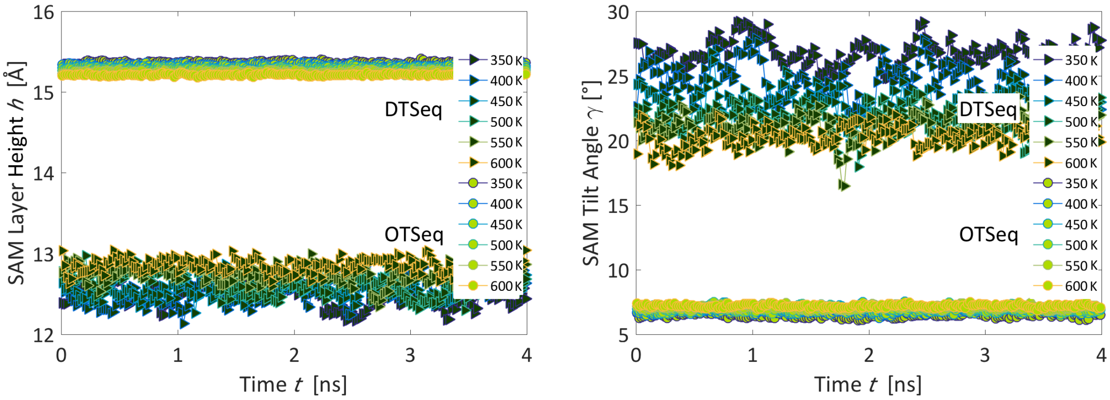

Figure A3: Averaged SAM layer height h and mean tilt angle γ of DTSeq (triangles) and OTSeq (circles) as a function of time, at temperatures from 350 K to 600 K (blue to yellow). Every data point represents a spatial mean value averaged over 10 ps (For better visibility, only every second data point is drawn).

Phenyl Ring Density & Tilt Angle

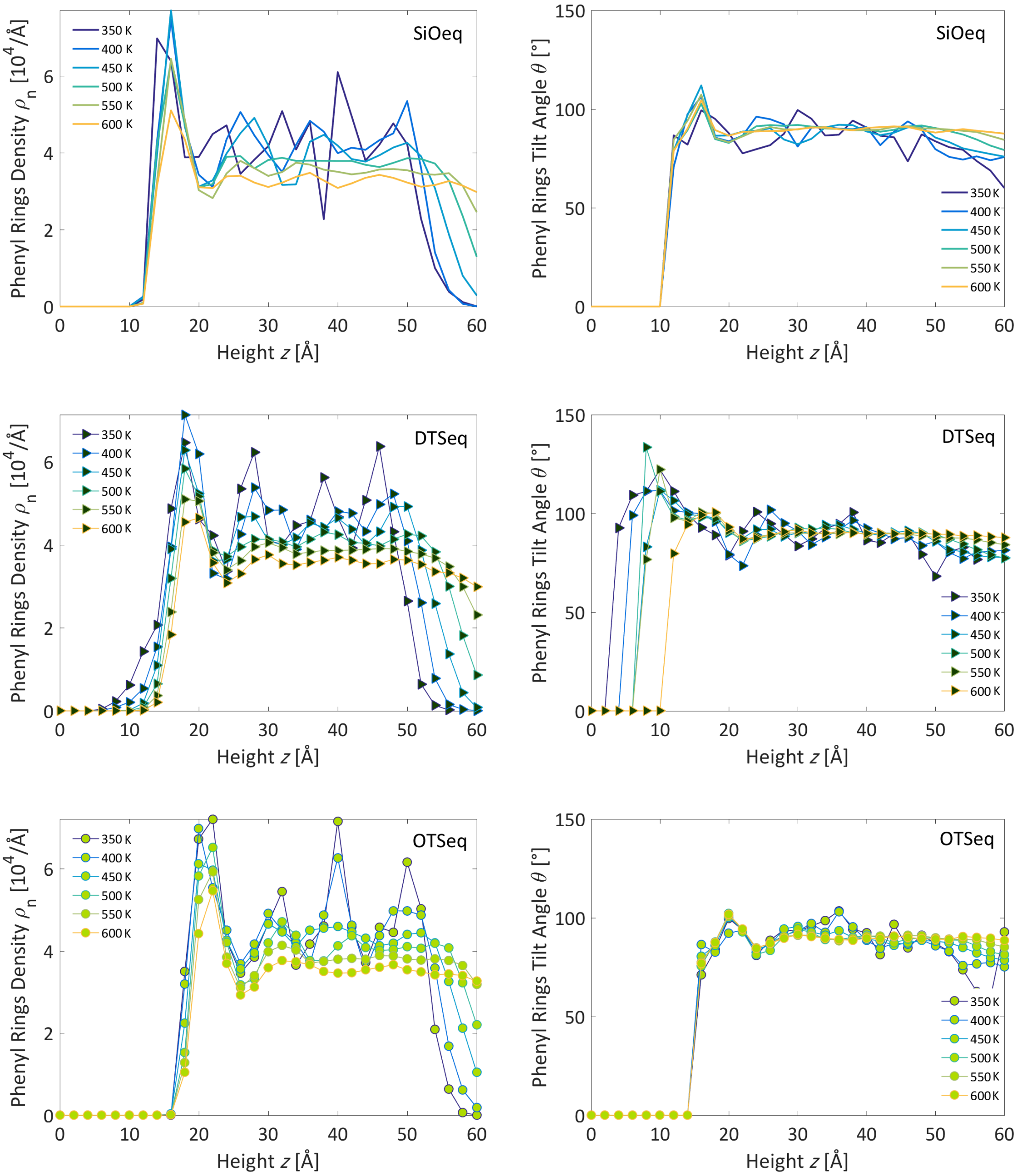

Figure A4: Time averaged mass density ρ_n of phenyl rings on SiOeq (solid lines), DTSeq (triangles), and OTSeq (circles), at temperatures from 350 K to 600 K (blue to yellow); Corresponding time averaged tilt angles θ of phenyl rings. Single data points are averaged over $\mathrm{d}z = 2\,\text{Å}$.

Mean Square Displacement

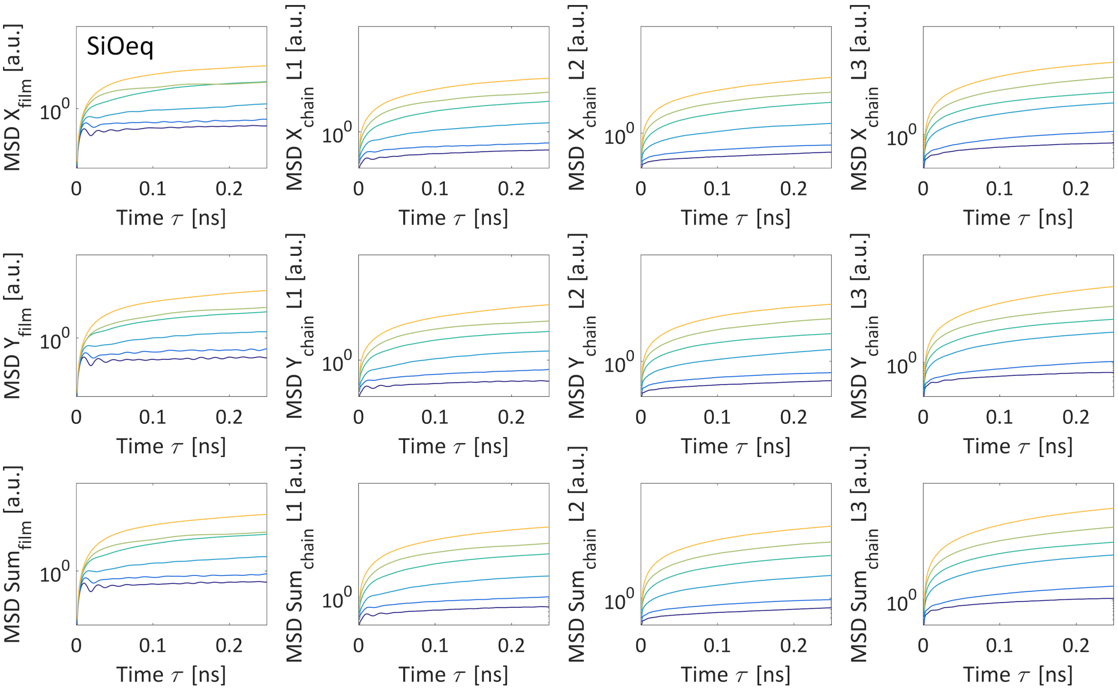

Figure A5: Mean square displacement of the polystyrene in the SiOeq system at 350 K, 400 K, 450 K, 500 K, 550 K, 600 K (blue to yellow). The first row depicts displacements in x-direction, the second in y-direction and the third the sum of x and y. The first column shows the displacement of the entire film (film), the second column only the displacements of polymer chains in a layer L1 close to the substrate, the third column in an intermediate layer L2, and the fourth column depicts the displacement in L3, which is the rest of the film above L2 (see Fig. 8.8). Please note the semi-logarithmic scale.

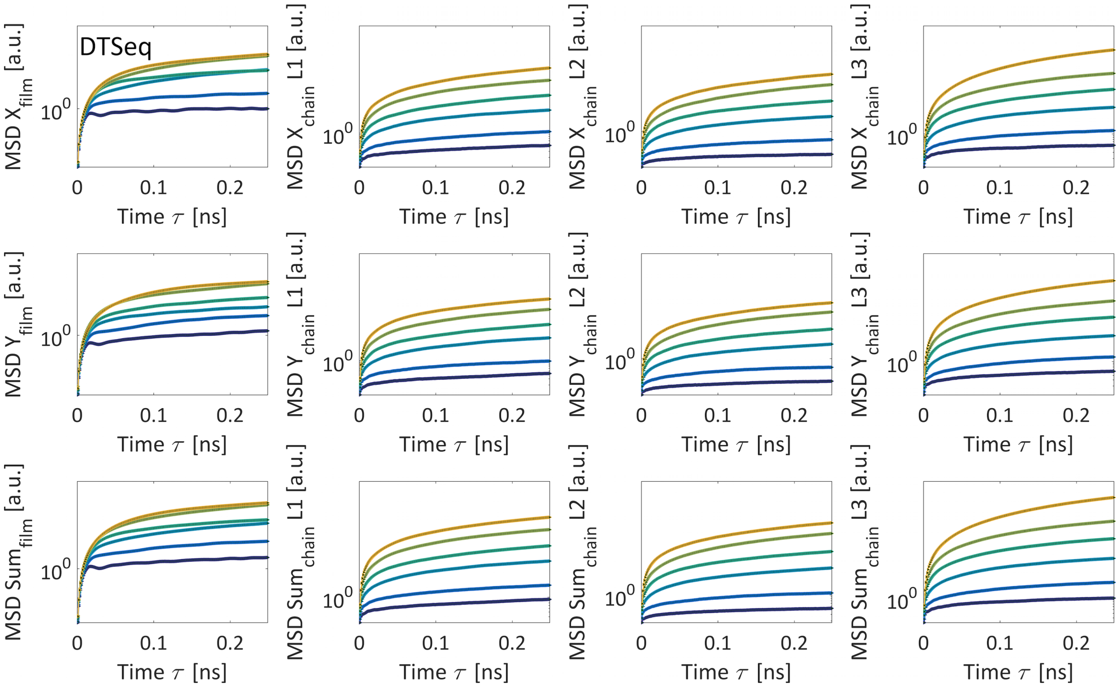

Figure A6: Mean square displacement of the polystyrene in the DTSeq system at 350 K, 400 K, 450 K, 500 K, 550 K, 600 K (blue to yellow). The first row depicts displacements in x-direction, the second in y-direction and the third the sum of x and y. The first column shows the displacement of the entire film (film), the second column only the displacements of polymer chains in a layer L1 close to the substrate, the third column in an intermediate layer L2, and the fourth column depicts the displacement in L3, which is the rest of the film above L2 (see Fig. 8.8). Please note the semi-logarithmic scale.

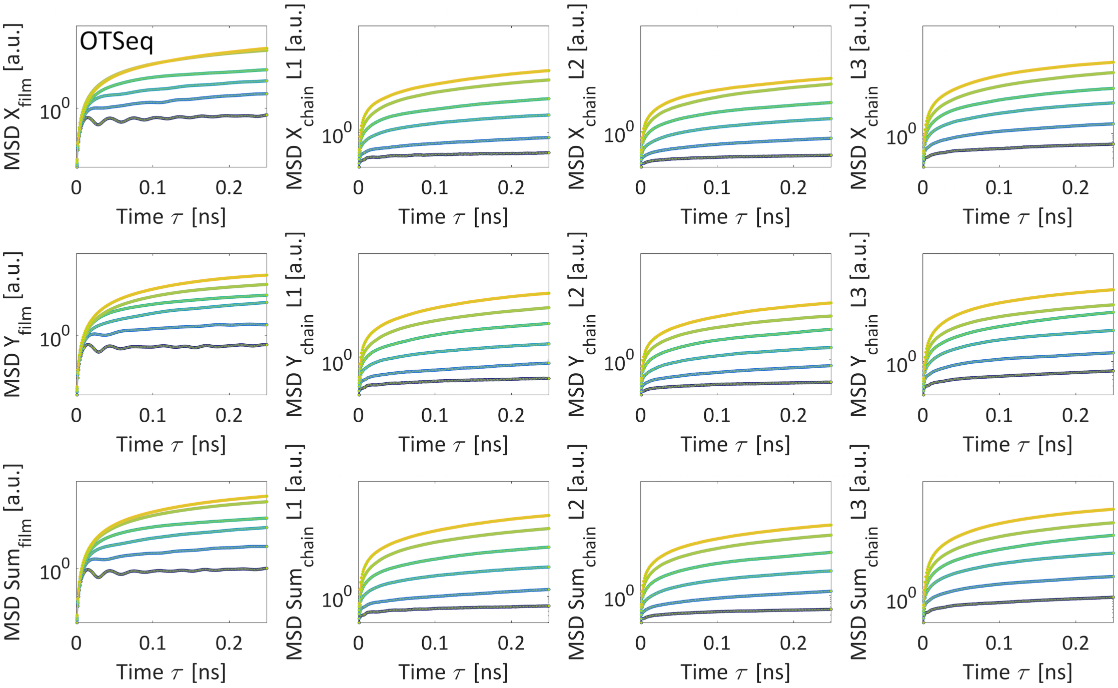

Figure A7: Mean square displacement of the polystyrene in the OTSeq system at 350 K, 400 K, 450 K, 500 K, 550 K, 600 K (blue to yellow). The first row depicts displacements in x-direction, the second in y-direction and the third the sum of x and y. The first column shows the displacement of the entire film (film), the second column only the displacements of polymer chains in a layer L1 close to the substrate, the third column in an intermediate layer L2, and the fourth column depicts the displacement in L3, which is the rest of the film above L2 (see Fig. 8.8). Please note the semi-logarithmic scale.

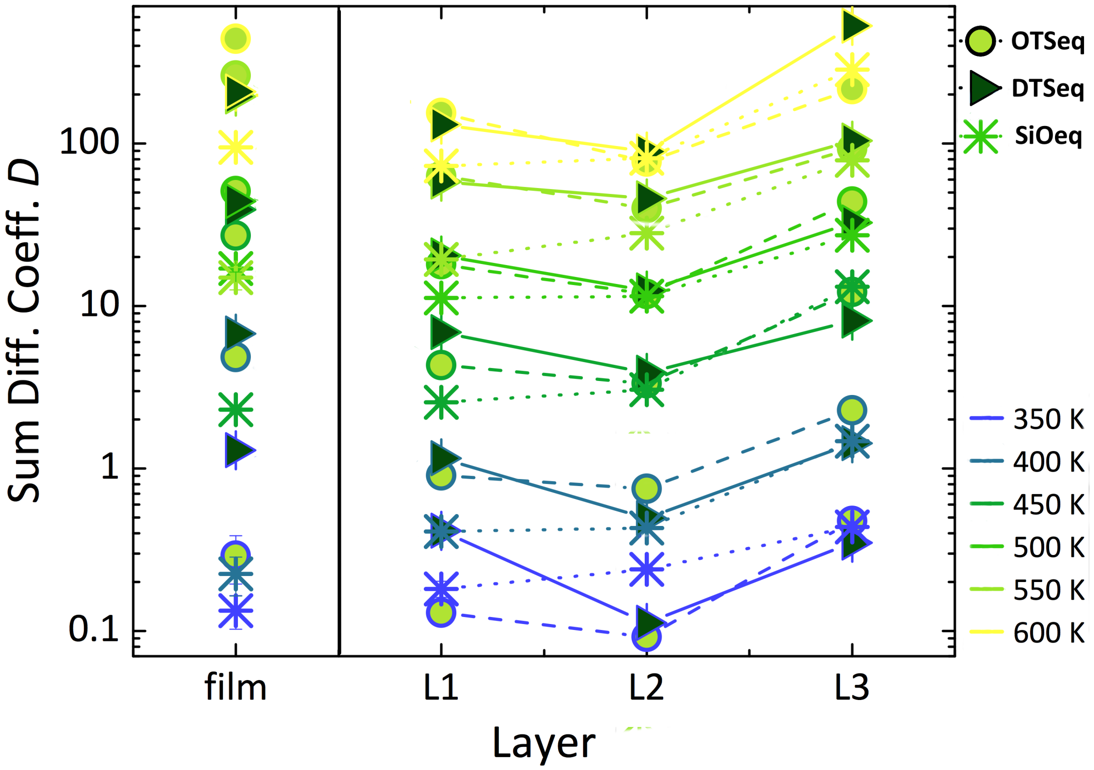

Figure A8: Fit values for diffusion coefficient D of the summed up lateral (x+y) MSD of the polystyrene film's center of mass (film) and the polymer chains layer by layer (L1: close to the substrate, L2: intermediate, L3: rest of polymer film) on DTSeq (triangles, solid line), OTSeq (circles, dashed line), and SiOeq (stars, dotted line). Colors represent temperatures from 350 K to 600 K (blue to yellow), lines are drawn to guide the eye.

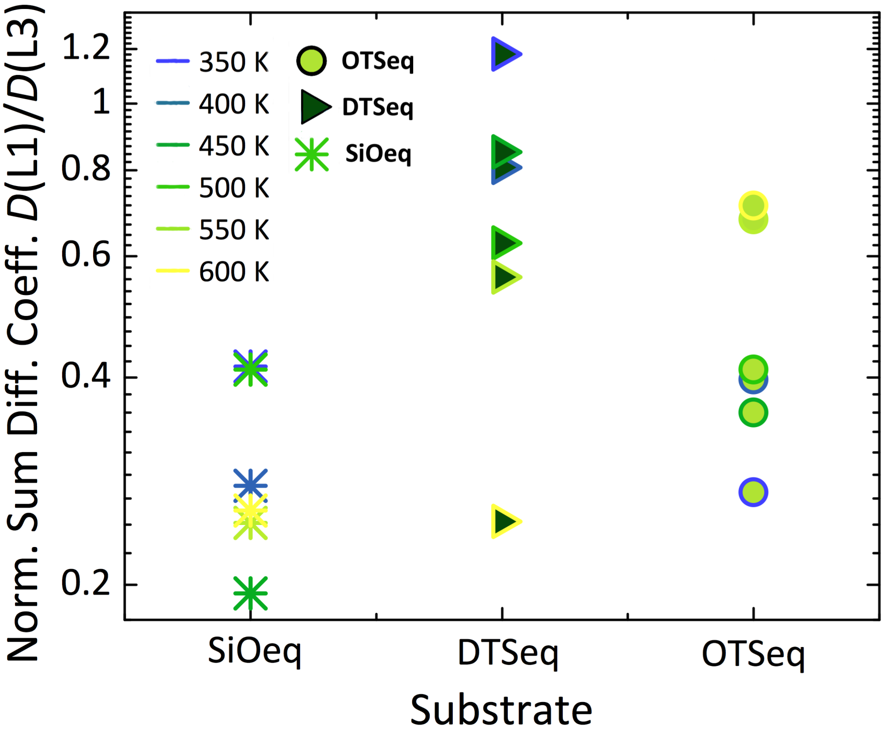

Figure A9: Fit values for diffusion coefficient D of the polymer chains in L1 normalized to diffusion coefficient D in L3 (L1: close to the substrate, L3: next to air interface) on DTSeq (triangles), OTSeq (circles), and SiOeq (stars). Colors represent temperatures from 350 K to 400 K (blue to yellow).

Bibliography

[Ack2013] N. Ackermann, *Charakterisierung hydrophobisierter Oberflächen*, Staatsexamensarbeit (2013) 1–46.

[Bac2013] S. Backes, *Fluidik dünner Polymerfilme*, Master's Thesis (2013) 1–91.

[Bar1999] J.-L. Barrat and L. Bocquet, *Large slip effect at a nonwetting fluid-solid interface*, Physical Review Letters **82** (1999) 4671–4674.

[Bar2000] D. J. Barlow, A.-M. Muslim, J. R. P. Webster, J. Penfold, C. M. Hollinshead, and M. J. Lawrence, *Molecular modelling of surfactant monolayers under constraints derived from neutron reflectance measurements*, Physical Chemistry Chemical Physics **2** (2000) 5208–5213.

[Bäu2008] O. Bäumchen, K. Jacobs, and R. Fetzer, *Probing slippage and flow dynamics of thin dewetting polymer films*, Proceedings of the 1st conference on microfluidics - microfluidics - bologna, 2008.

[Bäu2009a] O. Bäumchen, R. Fetzer, and K. Jacobs, *Reduced interfacial entanglement density affects the boundary conditions of polymer flow.*, Physical Review Letters **103** (2009) 247801–247801.

[Bäu2009b] O. Bäumchen, R. Fetzer, A. Münch, B. Wagner, and K. Jacobs, *Comprehensive Analysis of Dewetting Profiles to Quantify Hydrodynamic Slip*, Iutam symposium on advances in micro- and nanofluidics, 2009, pp. 51–65.

[Bäu2010a] O. Bäumchen, *Fluidics of Thin Polymer Films - Boundary Conditions and Interfacial Phenomena*, Dissertation, 2010.

[Bäu2010b] O. Bäumchen and K. Jacobs, *Can liquids slide? Linking stability and dynamics of thin liquid films to microscopic material properties*, Soft Matter **6** (2010) 6028.

[Bäu2010c] O. Bäumchen and K. Jacobs, *Slip effects in polymer thin films*, Journal of Physics: Condensed matter **22** (2010) 033102.

[Bäu2012a] O. Bäumchen, R. Fetzer, M. Klos, M. Lessel, L. Marquant, H. Hähl, and K. Jacobs, *Slippage and nanorheology of thin liquid polymer films*, Journal of Physics: Condensed matter **24** (2012) 325102.

[Bäu2012b] O. Bäumchen, J. D. McGraw, J. A. Forrest, and K. Dalnoki-Veress, *Reduced Glass Transition Temperatures in Thin Polymer Films: Surface Effect or Artifact?*, Physical Review Letters **109** (2012) 055701.

[Bäu2014] O. Bäumchen, L. Marquant, R. Blossey, A. Münch, B. Wagner, and K. Jacobs, *Influence of Slip on the Rayleigh-Plateau Rim Instability in Dewetting Viscous Films*, Physical Review Letters **113** (2014) 014501.

[Bel2008] M. Bellion, L. Santen, H. Mantz, H. Hähl, A. Quinn, A. Nagel, C. Gilow, C. Weitenberg, Y. Schmitt, and K. Jacobs, *Protein adsorption on tailored substrates: long-range forces and conformational changes*, Journal of Physics: Condensed matter **20** (2008) 404226.

[Bie1995] K. Bierbaum, M. Grunze, A. A. Baski, L. F. Chi, and W. Schrepp, *Growth of self-assembled n-alkyltrichlorosilane films on Si (100) investigated by atomic force microscopy*, Langmuir **11** (1995) 2143–2150.

[Bin1982] G. Binnig, H. Rohrer, C. Gerber, and E. Weibel, *Surface Studies by Scanning Tunneling Microscopy*, Physical Review Letters **49** (1982) 57–61.

[Bin1986] G. Binnig, C. F. Quate, and C. Gerber, *Atomic force microscope*, Physical Review Letters **56** (1986) 930–933.

[Bit2012] A. Bitler, R. Dover, and Y. Shai, *Fractal properties of macrophage membrane studied by AFM*, Micron **43** (2012) 1239–1245.

[Boc1994] L. Bocquet and J.-L. Barrat, *Hydrodynamic boundary conditions, correlation functions, and Kubo relations for confined fluids*, Physical Review E **49** (1994) 3079–3092.

[Boc2007] L. Bocquet and J.-L. Barrat, *Flow boundary conditions from nano- to micro-scales*, Soft Matter **3** (2007) 685–693.

[Boc2013] L. Bocquet and J.-L. Barrat, *On the Green-Kubo relationship for the liquid-solid friction coefficient*, The Journal of Chemical Physics **139** (2013) 044704.

[Boo1968] J. Boon, G. Challa, and D. W. Van Krevelen, *Crystallization kinetics of isotactic polystyrene. I. Spherulitic growth rate*, Journal of Polymer Science Part A-2: Polymer Physics **6** (1968) 1791–1801.

[Bou2008] C. I. Bouzigues, L. Bocquet, E. Charlaix, C. Cottin-Bizonne, B. Cross, L. Joly, A. Steinberger, C. Ybert, and P. Tabeling, *Using surface force apparatus, diffusion and velocimetry to measure slip lengths*, Philosophical Transactions of the Royal Society A: Mathematical, Physical and Engineering Sciences **366** (2008) 1455–1468.

[Bri1990] C. J. Brinker, A. J. Hurd, G. C. Frye, and K. J. Ward, *Sol-gel thin film formation*, Journal of Non-Crystalline Solids **121** (1990) 294–302.

[Bri2001] K. A. Briggman, J. C. Stephenson, W. E. Wallace, and L. J. Richter, *Absolute Molecular Orientational Distribution of the Polystyrene Surface*, The Journal of Physical Chemistry B **105** (2001) 2785–2791.

[Bro1992] F. Brochard and P. G. de Gennes, *Shear-dependent slippage at a polymer/solid interface*, Langmuir **8** (1992) 3033–3037.

[Brz1994] J. B. Brzoska, I. Ben Azouz, and F. Rondelez, *Silanization of Solid Substrates: A Step Toward Reproducibility*, Langmuir **10** (1994) 4367–4373.

[But2005] H.-J. Butt, B. Cappella, and M. Kappl, *Force measurements with the atomic force microscope: Technique, interpretation and applications*, Surface Science Reports **59** (2005) 1–152.

[Bro1994] F. Brochard-Wyart, P. G. de Gennes, and H. Hervet, *Wetting and slippage of polymer melts on semi-ideal surfaces*, Langmuir **10** (1994) 1566–1572.

[Bro1997] F. Brochard-Wyart, G. Debregeas, R. Fondecave, and P. Martin, *Dewetting of supported viscoelastic polymer films: Birth of rims*, Macromolecules **30** (1997) 1211–1213.

[Car2007] R. W. Carpick, J. D. Batteas, and M. Boer, *Scanning Probe Studies of Nanoscale Adhesion Between Solids in the Presence of Liquids and Monolayer Films*, Springer handbook of nanotechnology, 2007, pp. 951–980.

[Cas1944] A. B. D. Cassie and S. Baxter, *Wettability of porous surfaces*, Transactions of the Faraday Society **40** (1944) 546.

[Cas2015] J. M. Castillo, M. Klos, K. Jacobs, M. Horsch, and H. Hasse, *Characterization of alkylsilane self-assembled monolayers by molecular simulation*, Langmuir **31** (2015) 2630–2638.

[Cot2002] C. Cottin-Bizonne, S. Jurine, and J. Baudry, *Nanorheology: an investigation of the boundary condition at hydrophobic and hydrophilic interfaces*, The European Physical Journal E (2002).

[Cot2003] C. Cottin-Bizonne, J.-L. Barrat, L. Bocquet, and E. Charlaix, *Low-friction flows of liquid at nanopatterned interfaces*, Nature Materials **2** (2003) 238–240.

[Cot2004] C. Cottin-Bizonne, C. Barentin, E. Charlaix, L. Bocquet, and J.-L. Barrat, *Dynamics of simple liquids at heterogeneous surfaces: Molecular-dynamics simulations and hydrodynamic description*, The European Physical Journal E **15** (2004) 427–438.

[Cha2004] M. Chandross, E. B. Webb, M. J. Stevens, G. S. Grest, and S. H. Garofalini, *Systematic study of the effect of disorder on nanotribology of self-assembled monolayers*, Physical Review Letters **93** (2004).

[Cha2016] S. Chandran and G. Reiter, *Transient Cooperative Processes in Dewetting Polymer Melts*, Physical Review Letters **116** (2016).

[Che2012] Y. Chen, C. Zhang, M. Shi, and G. P. Peterson, *Slip boundary for fluid flow at rough solid surfaces*, Applied Physics Letters **100** (2012).

[Che2015] S. Chen, H. Wang, T. Qian, and P. Sheng, *Determining hydrodynamic boundary conditions from equilibrium fluctuations*, Physical Review E **92** (2015).

[Che2016] A. Chennevière, F. Cousin, F. Boué, E. Drockenmuller, K. R. Shull, L. Léger, and F. Restagno, *Direct Molecular Evidence of the Origin of Slip of Polymer Melts on Grafted Brushes*, Macromolecules **49** (2016) 2348–2353.

[Chi1996] C. Chipot, R. Jaffe, B. Maigret, D. A. Pearlman, and P. A. Kollman, *Benzene Dimer: A Good Model for π-π Interactions in Proteins? A Comparison between the Benzene and the Toluene Dimers in the Gas Phase and in an Aqueous Solution*, Journal of the American Chemical Society **118** (1996) 11217–11224.

[Chi2010] M. Chinappi and C. M. Casciola, *Intrinsic slip on hydrophobic self-assembled monolayer coatings*, Physics of Fluids **22** (2010) 042003.

[Cho2004] J.-H. Cho, B. M. Law, and F. Rieutord, *Dipole-Dependent Slip of Newtonian Liquids at Smooth Solid Hydrophobic Surfaces*, Physical Review Letters **92** (2004) 166102.

[Cla2001] T. C. Clancy, J. H. Jang, A. Dhinojwala, and W. L. Mattice, *Orientation of Phenyl Rings and Methylene Bisectors at the Free Surface of Atactic Polystyrene*, The Journal of Physical Chemistry B **105** (2001) 11493–11497.

[Cre1991] C. Creton, E. J. Kramer, and G. Hadziioannou, *Critical molecular weight for block copolymer reinforcement of interfaces in a two-phase polymer blend*, Macromolecules **24** (1991) 1846–1853.

[Cue2013] A. Cuenca and H. Bodiguel, *Submicron Flow of Polymer Solutions: Slippage Reduction due to Confinement*, Physical Review Letters **110** (2013) 108304–5.

[Dai2008] J. Daillant and A. Gibaud, *X-ray and Neutron Reflectivity* (J. Daillant and A. Gibaud, Hrsg.), Principles and Applications, Band 770, Springer, Berlin, Heidelberg, 2008.

[Dam2003] P. Damman, N. Baudelet, and G. Reiter, *Dewetting near the glass transition: Transition from a capillary force dominated to a dissipation dominated regime*, Physical Review Letters **91** (2003).

[deGen1971] P. G. de Gennes, *Reptation of a polymer chain in the presence of fixed obstacles*, The Journal of Chemical Physics **55** (1971) 572.

[deGen1985] P. G. de Gennes, *Wetting: statics and dynamics*, Reviews of Modern Physics **57** (1985) 827–863.

[deGen2002] P. G. de Gennes, *On fluid/wall slippage*, Langmuir **18** (2002) 3413–3414.

[Die1988] S. Dietrich, *Wetting Phenomena*, Phase transitions and critical phenomena, 1988.

[Din2006] J. N. Ding, P. L. Wong, and J. C. Yang, *Friction and fracture properties of polysilicon coated with self-assembled monolayers*, Wear **260** (2006) 209–214.

[Dos2005] D. A. Doshi, E. B. Watkins, J. N. Israelachvili, and J. Majewski, *Reduced water density at hydrophobic surfaces: effect of dissolved gases.*, Proceedings Of The National Academy Of Sciences Of The United States Of America **102** (2005) 9458–9462.

[Dal2000] K. Dalnoki-Veress, J. A. Forrest, P. G. de Gennes, and J. R. Dutcher, *Glass transition reductions in thin freely-standing polymer films : A scaling analysis of chain confinement effects*, Journal de Physique IV (Proceedings) **10** (2000) Pr7–221–Pr7–226.

[Ewe2012] B. W. Ewers and J. D. Batteas, *Molecular Dynamics Simulations of Alkylsilane Monolayers on Silica Nanoasperities: Impact of Surface Curvature on Monolayer Structure and Pathways for Energy Dissipation in Tribological Contacts*, The Journal of Physical Chemistry C **116** (2012) 25165–25177.

[Fel1993] N. F. Fell and P. W. Bohn, *Mass transport phenomena in thin films of poly (2-vinylpyridine) studied via optical guided wave techniques*, Analytical Chemistry **65** (1993) 3382–3388.

[Fet2005] R. Fetzer, K. Jacobs, A. Münch, B. Wagner, and T. P. Witelski, *New Slip Regimes and the Shape of Dewetting Thin Liquid Films*, Physical Review Letters **95** (2005) 127801.

[Fet2006a] R. Fetzer, *Einfluss von Grenzflächen auf die Fluidik dünner Polymerfilme*, Dissertation, 2006.

[Fet2006b] R. Fetzer, M. Rauscher, A. Münch, B. Wagner, and K. Jacobs, *Slip-controlled thin-film dynamics*, Europhysics Letters **75** (2006) 638–644.

[Fet2007a] R. Fetzer and K. Jacobs, *Slippage of Newtonian Liquids: Influence on the Dynamics of Dewetting Thin Films*, Langmuir **23** (2007) 11617–11622.

[Fet2007b] R. Fetzer, B. Wagner, M. Rauscher, and K. Jacobs, *Quantifying hydrodynamic slip: A comprehensive analysis of dewetting profiles*, Langmuir **23** (2007) 10559–10566.

[Fla2007] E. E. Flater, W. R. Ashurst, and R. W. Carpick, *Nanotribology of Octadecyltrichlorosilane Monolayers and Silicon: Self-Mated versus Unmated Interfaces and Local Packing Density Effects*, Langmuir **23** (2007) 9242–9252.

[Gau2000] K. S. Gautam, A. D. Schwab, A. Dhinojwala, and D. Zhang, *Molecular structure of polystyrene at air/polymer and solid/polymer interfaces*, Physical Review Letters **85** (2000) 3854–3857.

[Gay1999] C. Gay, *New concepts for the slippage of an entangled polymer melt at a grafted solid interface*, The European Physical Journal B **7** (1999) 251–262.

[Goo1960] R. J. Good and L. A. Girifalco, *A theory for estimation of surface and interfacial energies. III. Estimation of surface energies of solids from contact angle data*, The Journal of Physical Chemistry **64** (1960) 561–565.

[Gru2007] M. Grunze, *Preparation and Characterization of Self-Assembled Organic Films on Solid Substrates*, Physica Scripta **T49** (2007) 711–717.

[Gut2013] P. Gutfreund, O. Bäumchen, R. Fetzer, D. van der Grinten, M. Maccarini, K. Jacobs, H. Zabel, and M. Wolff, *Solid surface structure affects liquid order at the polystyrene–self-assembled-monolayer interface*, Physical Review E **87** (2013) 012306.

[Hae2015] S. Haefner, M. Benzaquen, O. Bäumchen, T. Salez, R. Peters, J. D. McGraw, K. Jacobs, E. Raphaël, and K. Dalnoki-Veress, *Influence of slip on the Plateau-Rayleigh instability on a fibre*, Nature Communications **6** (2015).

[Häh2012] H. Hähl, F. Evers, S. Grandthyll, M. Paulus, C. Sternemann, P. Loskill, M. Lessel, A. K. Hüsecken, T. Brenner, M. Tolan, and K. Jacobs, *Subsurface Influence on the Structure of Protein Adsorbates as Revealed by in Situ X-ray Reflectivity*, Langmuir **28** (2012) 7747–7756.

[Han2008] M. Hancer, *The effect of humidity on the stability of octadecyltrichlorosilane for the self-assembled monolayer coating applications*, Progress in Organic Coatings **63** (2008) 395–398.

[Hei2007] S. Heidenreich, P. Ilg, and S. Hess, *Boundary conditions for fluids with internal orientational degrees of freedom: Apparent velocity slip associated with the molecular alignment*, Physical Review E **75** (2007) 066302.

[Hel2002] R. Helmy and A. Y. Fadeev, *Self-assembled monolayers supported on TiO2: comparison of C18H37SiX3 (X= H, Cl, OCH3), C18H37Si (CH3) 2Cl, and C18H37PO (OH) 2*, Langmuir **18** (2002) 8924–8928.

[Her1998] S. Herminghaus, K. Jacobs, K. R. Mecke, J. Bischof, A. Fery, M. Ibn-Elhaj, and S. Schlagowski, *Spinodal Dewetting in Liquid Crystal and Liquid Metal Films*, Science **282** (1998) 916–919.

[Her2000] S. Herminghaus, A. Fery, S. Schlagowski, K. Jacobs, R. Seemann, H. Gau, W. Mönch, and T. Pompe, *Liquid microstructures at solid interfaces*, Journal of Physics: Condensed matter **12** (2000) A57–74.

[Her2001] S. Herminghaus, K. Jacobs, and R. Seemann, *The glass transition of thin polymer films: some questions, and a possible answer*, The European Physical Journal E **5** (2001) 531–538.

[Hil2010] A. Hildebrandt, A. Dehof, A. Rurainski, A. Bertsch, M. Schumann, N. C. Toussaint, A. Moll, D. Stöckel, S. Nickels, S. C. Mueller, H.-P. Lenhof, and O. Kohlbacher, *BALL - biochemical algorithms library 1.3*, BMC Bioinformatics **11** (2010) 531.

[Ho2011] T. A. Ho, D. Argyris, D. V. Papavassiliou, A. Striolo, L. L. Lee, and D. R. Cole, *Interfacial water on crystalline silica: a comparative molecular dynamics simulation study*, Molecular Simulation **37** (2011) 172–195.

[Hoc1988] R. W. Hockney and J. W. Eastwood, *Computer experiments using particle models*, IOP Publishing Ltd, 1988.

[Hoo1985] W. G. Hoover, *Canonical dynamics: Equilibrium phase-space distributions*, Physical Review A **31** (1985) 1695–1697.

[Hua2008] D. M. Huang, C. Sendner, D. Horinek, R. R. Netz, and L. Bocquet, *Water Slippage versus Contact Angle: A Quasiuniversal Relationship*, Physical Review Letters **101** (2008) 226101.

[Hub2005] G. Huber, H. Mantz, and R. Spolenak, *Evidence for capillarity contributions to gecko adhesion from single spatula nanomechanical measurements*, Proceedings Of The National Academy Of Sciences Of The United States Of America **102** (2005) 16293–16296.

[Hud2011] D. Hudzinskyy and A. V. Lyulin, *Confinement and shear effects for atactic polystyrene film structure and mechanics*, Modelling and Simulation in Materials Science and Engineering **19** (2011) 074007.

[Hum1996] W. Humphrey, A. Dalke, and K. Schulten, *VMD: Visual molecular dynamics*, Journal of Molecular Graphics **14** (1996) 33–38.

[Isr1997] J. N. Israelachvili, *Intermolecular and Surface Forces Academic*, Second Edition, Academic Press, 1997.

[Jac1998a] K. Jacobs, S. Herminghaus, and K. R. Mecke, *Thin Liquid Polymer Films Rupture via Defects*, Langmuir **14** (1998) 965–969.

[Jac1998b] K. Jacobs, R. Seemann, G. Schatz, and S. Herminghaus, *Growth of Holes in Liquid Films with Partial Slippage*, Langmuir **14** (1998) 4961–4963.

[Jac2008] K. Jacobs, R. Seemann, and S. Herminghaus, *Stability and Dewetting of Thin Liquid Films*, Thin liquid films, 2008, pp. 243–265.

[Jac2015] K. Jacobs, Personal Communication (2015).

[Jol2006] L. Joly, C. Ybert, and L. Bocquet, *Probing the Nanohydrodynamics at Liquid-Solid Interfaces Using Thermal Motion*, Physical Review Letters **96** (2006) 046101.

[Jor1990] W. L. Jorgensen and D. L. Severance, *Aromatic-aromatic interactions: free energy profiles for the benzene dimer in water, chloroform, and liquid benzene*, Journal of the American Chemical Society **112** (1990) 4768–4774.

[Jor1996] W. L. Jorgensen and D. S. Maxwell, *Development and testing of the OPLS all-atom force field on conformational energetics and properties of organic liquids*, Journal of the American Chemical Society **118** (1996) 11225–11236.

[Jos2006] P. Joseph, C. Cottin-Bizonne, J. M. Benoît, C. Ybert, C. Journet, P. Tabeling, and L. Bocquet, *Slippage of Water Past Superhydrophobic Carbon Nanotube Forests in Microchannels*, Physical Review Letters **97** (2006) 156104.

[Ked1994] J. L. Keddie, R. Jones, and R. A. Cory, *Size-dependent depression of the glass transition temperature in polymer films*, Europhysics Letters **27** (1994) 59–64.

[Kry2005] C. Krywka, M. Paulus, C. Sternemann, M. Volmer, A. Remhof, G. Nowak, A. Nefedov, B. Pöter, M. Spiegel, and M. Tolan, *The new diffractometer for surface X-ray diffraction at beamline BL9 of DELTA*, Journal of Synchrotron Radiation **13** (2005) 8–13.

[Kul2005] S. A. Kulkarni, S. A. Mirji, A. B. Mandale, and R. P. Gupta, *Growth kinetics and thermodynamic stability of octadecyltrichlorosilane self-assembled monolayer on Si (100) substrate*, Materials Letters **59** (2005) 3890–3895.

[Kun2007] C. Kunert and J. Harting, *Roughness Induced Boundary Slip in Microchannel Flows*, Physical Review Letters **99** (2007) 176001.

[Lan1991] L. D. Landau and E. M. Lifschitz, *Hydrodynamik, Band VI Lehrbuch der theoretischen Physik*, Akademie Verlag, Berlin, 1991.

[Lat1956] G. H. Lathe and C. R. J. Ruthven, *The separation of substances and estimation of their relative molecular sizes by the use of columns of starch in water*, Biochemical Journal **62** (1956) 665–674.

[Lau2007] E. Lauga, M. Brenner, and H. Stone, *Microfluidics: The No-Slip Boundary Condition*, Springer handbook of experimental fluid mechanics, 2007, pp. 1219–1240.

[Lee2016] H. Lee, W. Lee, Y. S. Han, E. Kim, and D. Y. Ryu, *Autophobic dewetting of polystyrenes on the substrates grafted with chemically identical polymers*, Polymer Journal **48** (2016) 503–507.

[Lég2003] L. Léger, *Friction mechanisms and interfacial slip at fluid–solid interfaces*, Journal of Physics: Condensed matter **15** (2003) S19–S29.

[Les2015] M. Lessel, O. Bäumchen, M. Klos, H. Hähl, R. Fetzer, M. Paulus, R. Seemann, and K. Jacobs, *Self-assembled silane monolayers: an efficient step-by-step recipe for high-quality, low energy surfaces*, Surface and Interface Analysis **47** (2015) 557–564.

[Loh2015] D. Lohse and X. Zhang, *Surface nanobubbles and nanodroplets*, Reviews of Modern Physics **87** (2015) 981–1035.

[Los2012a] P. Loskill, H. Hähl, T. Faidt, S. Grandthyll, F. Müller, and K. Jacobs, *Is adhesion superficial? Silicon wafers as a model system to study van der Waals interactions*, Advances in Colloid and Interface Science **179** (2012) 107–113.

[Los2012b] P. Loskill, H. Hähl, and N. Thewes, *Influence of the Subsurface Composition of a Material on the Adhesion of Staphylococci*, Langmuir **28** (2012) 7242–7248.

[Los2014] P. Loskill, P. M. Pereira, P. Jung, M. Bischoff, M. Herrmann, M. G. Pinho, and K. Jacobs, *Reduction of the Peptidoglycan Crosslinking Causes a Decrease in Stiffness of the Staphylococcus aureus Cell Envelope*, Biophysical journal **107** (2014) 1082–1089.

[Lun2012] N. J. Lund, X. P. Zhang, K. Mahelona, and S. C. Hendy, *Calculation of effective slip on rough chemically heterogeneous surfaces using a homogenization approach*, Physical Review E **86** (2012).

[Lyu2011] A. V. Lyulin, D. Hudzinskyy, E. Janiaud, and A. Chateauminois, *Journal of Non-Crystalline Solids*, Journal of Non-Crystalline Solids **357** (2011) 567–574.

[Maa2013] A. Maali and B. Bhushan, *Nanobubbles and their role in slip and drag*, Journal of Physics: Condensed matter **25** (2013) 184003.

[Mac2005] L. G. MacDowell and M. Müller, *Observation of autophobic dewetting on polymer brushes from computer simulation*, Journal of Physics: Condensed matter **17** (2005) S3523–S3528.

[Mac2007] M. Maccarini, R. Steitz, M. Himmelhaus, J. Fick, S. Tatur, M. Wolff, M. Grunze, J. Janecek, and R. R. Netz, *Density depletion at solid-liquid interfaces: A neutron reflectivity study*, Langmuir **23** (2007) 598–608.

[Mar2007] J. E. Mark, *Physical Properties of Polymers Handbook* (J. E. Mark, Hrsg.), Springer, New York, NY, 2007.

[Mas2002] J.-L. Masson and P. F. Green, *Hole Formation in Thin Polymer Films: A Two-Stage Process*, Physical Review Letters **88** (2002) 205504.

[Mat2000] J. Mattsson, J. A. Forrest, and L. Börjesson, *Quantifying glass transition behavior in ultrathin free-standing polymer films*, Physical Review E **62** (2000) 5187–5200.

[McG2011] J. D. McGraw, N. M. Jago, and K. Dalnoki-Veress, *Capillary levelling as a probe of thin film polymer rheology*, Soft Matter **7** (2011) 7832–7838.

[McG2014] J. D. McGraw, O. Bäumchen, M. Klos, S. Haefner, M. Lessel, S. Backes, and K. Jacobs, *Nanofluidics of thin polymer films: Linking the slip boundary condition at solid–liquid interfaces to macroscopic pattern formation and microscopic interfacial properties*, Advances in Colloid and Interface Science **210** (2014) 13–20.

[McG2015] J. D. McGraw and K. Jacobs, *Controlling Wetting Properties of Polymers*, Encyclopedia of polymeric nanomaterials, 2015, pp. 460–469.

[McG2016] J. D. McGraw, T. S. Chan, S. Maurer, T. Salez, M. Benzaquen, E. Raphaël, M. Brinkmann, and K. Jacobs, *Slip-mediated dewetting of polymer microdroplets*, Proceedings Of The National Academy Of Sciences Of The United States Of America **113** (2016) 1168–1173.

[McG] J. D. McGraw, M. Klos, A. Bridet, H. Hähl, M. Paulus, J. M. Castillo, M. Horsch, and K. Jacobs, *Influence of bidisperse self-assembled monolayer structure on the slip boundary condition of thin polymer films*, in preparation.

[Mez2006] M. Mezger, *High-resolution in situ x-ray study of the hydrophobic gap at the water–octadecyl-trichlorosilane interface*, Proceedings Of The National Academy Of Sciences Of The United States Of America **103** (2006) 18401–18404.

[Mez2010] M. Mezger, F. Sedlmeier, D. Horinek, H. Reichert, D. Pontoni, and H. Dosch, *On the Origin of the Hydrophobic Water Gap: An X-ray Reflectivity and MD Simulation Study*, Journal of the American Chemical Society **132** (2010) 6735–6741.

[Mic2010] X. Michalet, *Mean square displacement analysis of single-particle trajectories with localization error: Brownian motion in an isotropic medium*, Physical Review E **82** (2010) 041914.

[Mig1993] K. B. Migler, H. Hervet, and L. Léger, *Slip transition of a polymer melt under shear stress*, Physical Review Letters **70** (1993) 287–290.

[Mit1993] V. S. Mitlin, *Dewetting of Solid Surface: Analogy with Spinodal Decomposition*, Journal of Colloid and Interface Science **156** (1993) 491–497.

[Mol2006] A. Moll, A. Hildebrandt, H.-P. Lenhof, and O. Kohlbacher, *BALLView: a tool for research and education in molecular modeling.*, Bioinformatics **22** (2006) 365–366.

[Moo1964] J. C. Moore, *Gel permeation chromatography. I. A new method for molecular weight distribution of high polymers*, Journal of Polymer Science Part A: Polymer Chemistry **2** (1964) 835–843.

[Muk2010] M. K. Mukhopadhyay, L. B. Lurio, Z. Jiang, X. Jiao, M. Sprung, C. DeCaro, and S. K. Sinha, *Measurement of the interior structure of thin polymer films using grazing incidence diffuse x-ray scattering*, Physical Review E **82** (2010) 011804.

[Mül2009] M. Müller, C. Pastorino, and J. Servantie, *Hydrodynamic boundary condition of polymer melts at simple and complex surfaces*, Computer Physics Communications **180** (2009) 600–604.

[Mün2005] A. Münch, *Dewetting rates of thin liquid films*, Journal of Physics: Condensed matter **17** (2005) S309–S318.

[Nak2003] T. Nakano and T. Yade, *Synthesis, Structure, and Photophysical and Electrochemical Properties of a π-Stacked Polymer*, Journal of the American Chemical Society **125** (2003) 15474–15484.

[Nak2014] T. Nakano (Hrsg.), *π-Stacked Polymers and Molecules*, Theory, Synthesis, and Properties, Springer Japan, Tokyo, 2014.

[Nav1823] C.-L. Navier, *Mémoire sur les lois du mouvement des fluides*, Mémoires de l'Académie Royale des Sciences de l' . . . (1823).

[Net2005] C. Neto, D. R. Evans, and E. Bonaccurso, *Boundary slip in Newtonian liquids: a review of experimental studies*, Reports on Progress in Physics **68** (2005) 2859–2897.

[Nia2008] A. Niavarani and N. V. Priezjev, *Rheological study of polymer flow past rough surfaces with slip boundary conditions*, The Journal of Chemical Physics **129** (2008) 144902.

[Nos1984] S. Nosé, *A unified formulation of the constant temperature molecular dynamics methods*, The Journal of Chemical Physics **81** (1984) 511.

[Ohk2014] C.-W. Ohk, M. Koo, B.-J. Lee, S.-E. Lee, H.-S. Jang, and Y.-C. Park, *Slip behavior in polymethylmethacrylate films in dependence of self-assembled monolayer wettability*, Polymer **55** (2014) 6935–6939.

[Oka1994] T. Okada, H. Saito, and T. Inoue, *Kinetic studies of crystallization in mixtures of isotactic polystyrene and atactic polystyrene*, Polymer **35** (1994) 5699–5705.

[Oro1997] A. Oron, S. H. Davis, and S. G. Bankoff, *Long-scale evolution of thin liquid films*, Reviews of Modern Physics **69** (1997) 931–980.

[Pan2014] Y. Pan, B. Bhushan, and X. Zhao, *The study of surface wetting, nanobubbles and boundary slip with an applied voltage: A review*, Beilstein Journal of Nanotechnology **5** (2014) 1042–1065.

[Par1954] L. G. Parratt, *Surface Studies of Solids by Total Reflection of X-Rays*, Physical Review **95** (1954) 359–369.

[Pas2006] C. Pastorino, K. Binder, T. Kreer, and M. Müller, *Static and dynamic properties of the interface between a polymer brush and a melt of identical chains*, The Journal of Chemical Physics **124** (2006) 064902.

[Pas2008] C. Pastorino, K. Binder, and M. Müller, *Coarse-Grained Description of a Brush - Melt Interface in Equilibrium and under Flow*, Macromolecules **42** (2008) 401–410.

[Pau2005] M. Paulus, R. Fendt, C. Sternemann, C. Gutt, H. Hövel, M. Volmer, M. Tolan, and K. Wille, *An internet-based synchrotron experiment for students measuring the X-ray magnetic circular dichroism of a PtFe alloy*, Journal of Synchrotron Radiation **12** (2005) 246–250.

[Pau2008] M. Paulus, D. Lietz, C. Sternemann, K. Shokuie, F. Evers, M. Tolan, C. Czeslik, and R. Winter, *An access to buried interfaces: the X-ray reflectivity set-up of BL9 at DELTA*, Journal of Synchrotron Radiation **15** (2008) 600–605.

[Pet2002] R. D. Peters, P. F. Nealey, J. N. Crain, and F. J. Himpsel, *A Near Edge X-ray Absorption Fine Structure Spectroscopy Investigation of the Structure of Self-Assembled Films of Octadecyltrichlorosilane - Langmuir (ACS Publications)*, Langmuir **18** (2002) 1250–1256.

[Pit2000] R. Pit, H. Hervet, and L. Léger, *Direct experimental evidence of slip in hexadecane: solid interfaces*, Physical Review Letters **85** (2000) 980–983.

[Pit2010] B. Pittenger, N. Erina, and C. Su, *Quantitative mechanical property mapping at the nanoscale with PeakForce QNM*, Application Note Veeco Instruments Inc (2010).

[Ple2011] G. Pletikapić, A. Berquand, T. M. Radić, and V. Svetličić, *Quantitative Nanomechanical Mapping of Marine Diatom in Seawater Using Peak Force Tapping Atomic Force Microscopy*, Journal of Phycology **48** (2011) 174–185.

[Pli1995] S. Plimpton, *Fast Parallel Algorithms for Short-Range Molecular Dynamics*, Journal of Computational Physics **117** (1995) 1–19.

[Poc2002] A. V. Pocius, M. K. Chaudhury, and D. A. Dillard, *Surfaces, Chemistry and Applications*, Elsevier Science, 2002.

[Pri2004] N. V. Priezjev and S. M. Troian, *Molecular origin and dynamic behavior of slip in sheared polymer films*, Physical Review Letters **92** (2004) 018302.

[Pri2005] N. V. Priezjev, A. A. Darhuber, and S. M. Troian, *Slip behavior in liquid films on surfaces of patterned wettability: Comparison between continuum and molecular dynamics simulations*, Physical Review E **71** (2005) 041608.

[Pri2006] N. V. Priezjev and S. M. Troian, *Influence of periodic wall roughness on the slip behaviour at liquid/solid interfaces: molecular-scale simulations versus continuum predictions*, Journal of Fluid Mechanics **554** (2006) 25–46.

[Pri2010] N. V. Priezjev, *Relationship between induced fluid structure and boundary slip in nanoscale polymer films*, Physical Review E **82** (2010).

[PSS2013] PSS Polymer Standards Service GmbH, *Certificate of Analysis*, `http://www.pss-polymer.com/uploads/tx_pss/pdf/product/psbr47k.pdf`, 2013.

[Pui2003] J. Puibasset and R. J. M. Pellenq, *Grand canonical Monte Carlo simulation study of water structure on hydrophilic mesoporous and plane silica substrates*, Journal of Chemical Physics **119** (2003) 9226–9232.

[Rau2008] M. Rauscher, R. Blossey, A. Münch, and B. Wagner, *Spinodal Dewetting of Thin Films with Large Interfacial Slip: Implications from the Dispersion Relation*, Langmuir **24** (2008) 12290–12294.

[Rav1985] G. Ravishanker and D. L. Beveridge, *Potential of mean force for the stacking of phenyl rings in aqueous solution*, Journal of the American Chemical Society **107** (1985) 2565–2566.

[Rei1992] G. Reiter, *Dewetting of thin polymer films*, Physical Review Letters **68** (1992) 75–78.

[Rei2000a] G. Reiter and R. Khanna, *Kinetics of autophobic dewetting of polymer films*, Langmuir **16** (2000) 6351–6357.

[Rei2000b] G. Reiter and R. Khanna, *Real-Time Determination of the Slippage Length in Autophobic Polymer Dewetting*, Physical Review Letters **85** (2000) 2753–2756.

[Rei2009] G. Reiter, S. Al Akhrass, M. Hamieh, P. Damman, S. Gabriele, T. Vilmin, and E. Raphaël, *Dewetting as an investigative tool for studying properties of thin polymer films*, The European Physical Journal Special Topics **166** (2009) 165–172.

[Ric1998] A. G. Richter, M. K. Durbin, C. J. Yu, and P. Dutta, *In situ time-resolved X-ray reflectivity study of self-assembly from solution*, Langmuir **14** (1998) 5980–5983.

[RouJr1953] P. E. Rouse Jr, *A Theory of the Linear Viscoelastic Properties of Dilute Solutions of Coiling Polymers*, Journal of Chemical Physics **21** (1953) 1272–1280.

[Rub2003] M. Rubinstein and R. H. Colby, *Polymer Physics*, Band 53, Oxford University Press, 2003.

[Ruc1974] E. Ruckenstein and R. K. Jain, *Spontaneous rupture of thin liquid films*, Journal of the Chemical Society, Faraday Transactions 2: Molecular and Chemical Physics **70** (1974) 132–147.

[Sab2015] S. M. Sabzevari, J. D. McGraw, K. Jacobs, and P. Wood-Adams, *Sacrificial mica substrates influence the slip boundary condition of dewetting polymer films*, Polymer **78** (2015) 202–207.

[Sag1980] J. Sagiv, *Organized monolayers by adsorption. 1. Formation and structure of oleophobic mixed monolayers on solid surfaces*, Journal of the American Chemical Society **102** (1980) 92–98.

[Sch2005] T. Schmatko, H. Hervet, and L. Léger, *Friction and slip at simple fluid-solid interfaces: the roles of the molecular shape and the solid-liquid interaction*, Physical Review Letters **94** (2005) 244501.

[Sch2006] T. Schmatko, H. Hervet, and L. Léger, *Effect of nanometric-scale roughness on slip at the wall of simple fluids*, Langmuir **22** (2006) 6843–6850.

[See2001] R. Seemann, S. Herminghaus, and K. Jacobs, *Dewetting patterns and molecular forces: A reconciliation*, Physical Review Letters **86** (2001) 5534–5537.

[See2005] R. Seemann, S. Herminghaus, C. Neto, S. Schlagowski, D. Podzimek, R. Konrad, H. Mantz, and K. Jacobs, *Dynamics and structure formation in thin polymer melt films*, Journal of Physics: Condensed matter **17** (2005) S267–S290.

[Seo2007] Y. Seo and W. Jhe, *Atomic force microscopy and spectroscopy*, Reports on Progress in Physics **71** (2007) 016101–016124.

[Ser2008] J. Servantie and M. Müller, *Temperature Dependence of the Slip Length in Polymer Melts at Attractive Surfaces*, Physical Review Letters **101** (2008) 026101–4.

[Sig2016a] Sigma-Aldrich, *Product Specification: Poly[4,5-difluoro-2,2-bis(trifluoromethyl)-1,3-dioxole-co-tetrafluoroethylene]*, `http://www.sigmaaldrich.com/Graphics/COfAInfo/SigmaSAPQM/SPEC/46/469629/469629-BULK_______ALDRICH__.pdf`, 2016.

[Sig2016b] Sigma-Aldrich, *Product Specification: Trichlor(octadecyl)silane*, `http://www.sigmaaldrich.com/Graphics/COfAInfo/SigmaSAPQM/SPEC/10/104817/104817-BULK_______ALDRICH__.pdf`, 2016.

[Sig2016c] Sigma-Aldrich, *Product Specification: Trichlorododecylsilane*, `http://www.sigmaaldrich.com/catalog/product/aldrich/44230?lang=de&region=DE&cm_sp=Insite-_-prodRecCold_xviews-_-prodRecCold10-3`, 2016.

[Sri1998] U. Srinivasan, M. R. Houston, R. T. Howe, and R. Maboudian, *Alkyltrichlorosilane-based self-assembled monolayer films for stiction reduction in silicon micromachines*, Journal of Microelectromechanical Systems **7** (1998) 252–260.

[Ste2003] R. Steitz, T. Gutberlet, T. Hauss, B. Klösgen, R. Krastev, S. Schemmel, A. C. Simonsen, and G. H. Findenegg, *Nanobubbles and Their Precursor Layer at the Interface of Water Against a Hydrophobic Substrate*, Langmuir **19** (2003) 2409–2418.

[Ste2007] A. Steinberger, C. Cottin-Bizonne, P. Kleimann, and E. Charlaix, *High friction on a bubble mattress*, Nature Materials **6** (2007) 665–668.

[Ste2012] H.-G. Steinrück, M. Klimczak, S. Gerth, and A. Beerlink, *X-ray Reflectivity Study of the Growth of Octadecyltrichlorosilane SAMs on Amorphous and Crystalline Silicon Dioxide*, photon-science.desy.de (2012).

[Ste2014] H.-G. Steinrück, A. Magerl, M. Deutsch, and B. M. Ocko, *Pseudorotational Epitaxy of Self-Assembled Octadecyltrichlorosilane Monolayers on Sapphire (0001)*, Physical Review Letters **113** (2014) 156101.

[Ste2015] H.-G. Steinrück, J. Will, A. Magerl, and B. M. Ocko, *Structure of n-Alkyltrichlorosilane Monolayers on Si(100)/SiO2*, Langmuir **31** (2015) 11774–11780.

[Sug1997] T. Sugimori, H. Masuda, N. Ohata, K. Koiwai, A. Odani, and O. Yamauchi, *Structural Dependence of Aromatic Ring Stacking and Related Weak Interactions in Ternary Amino Acid-Copper(II) Complexes and Its Biological Implication*, Inorganic Chemistry **36** (1997) 576–583.

[Sun2002] G. Sun, E. Bonaccurso, V. Franz, and H.-J. Butt, *Confined liquid: Simultaneous observation of a molecularly layered structure and hydrodynamic slip*, The Journal of Chemical Physics **117** (2002) 10311–5.

[Tch2005] M. A. Tchesnokov, J. Molenaar, J. J. M. Slot, and R. Stepanyan, *A molecular model for cohesive slip at polymer melt/solid interfaces*, The Journal of Chemical Physics **122** (2005) 214711–13.

[Tid1990] I. M. Tidswell, B. M. Ocko, P. S. Pershan, S. R. Wasserman, G. M. Whitesides, and J. D. Axe, *X-ray specular reflection studies of silicon coated by organic monolayers (alkylsiloxanes)*, Physical Review B **41** (1990) 1111–1128.

[Tol1999] M. Tolan, *X-Ray Scattering from Soft-Matter Thin Films*, Materials Science and Basic Research, Band 148, Springer Verlag, Berlin, Heidelberg, 1999.

[Tol2008] M. Tolan, T. Weis, C. Westphal, and K. Wille, *DELTA: Synchrotron light in nordrhein-westfalen*, Synchrotron Radiation News **16** (2008) 9–11.

[Tre2013] N. Tretyakov and M. Müller, *Correlation between surface topography and slippage: a Molecular Dynamics study*, Soft Matter **9** (2013) 3613–3623.

[Trt2012] P. Trtik, J. Kaufmann, and U. Volz, *On the use of peak-force tapping atomic force microscopy for quantification of the local elastic modulus in hardened cement paste*, Cement and Concrete Research **42** (2012) 215–221.

[TUD2016] TU Dortmund, *Dortmund Electron Accelerator*, `http://www.delta.tu-dortmund.de/cms/de/Beschleuniger/index.html`, 2016.

[Ver1967] L. Verlet, *Computer "Experiments" on Classical Fluids. I. Thermodynamical Properties of Lennard-Jones Molecules*, Physical Review **159** (1967) 98–103.

[Ver1968] L. Verlet, *Computer "Experiments" on Classical Fluids. II. Equilibrium Correlation Functions*, Physical Review **165** (1968) 201–214.

[Vin2011] O. I. Vinogradova and A. V. Belyaev, *Wetting, roughness and flow boundary conditions*, Journal of Physics: Condensed matter **23** (2011) 184104–16.

[Vri1966] A. Vrij, *Possible mechanism for the spontaneous rupture of thin, free liquid films*, Discussions of the Faraday Society **42** (1966) 23–33.

[Wan2003] Y. Wang and M. Lieberman, *Growth of Ultrasmooth Octadecyltrichlorosilane Self-Assembled Monolayers on SiO 2*, Langmuir **19** (2003) 1159–1167.

[Wan2009] G. M. Wang, R. Prabhakar, and E. M. Sevick, *Hydrodynamic Mobility of an Optically Trapped Colloidal Particle near Fluid-Fluid Interfaces*, Physical Review Letters **103** (2009) 248303–4.

[Wan2011] G. M. Wang, R. Prabhakar, Y. X. Gao, and E. M. Sevick, *Micro-rheology near fluid interfaces*, Journal of Optics **13** (2011) 044009.

[War1977] F. P. Warner, W. J. MacKnight, and R. S. Stein, *A small-angle x-ray scattering study of blends of isotactic and atactic polystyrene*, Journal of Polymer Science: Polymer Physics Edition **15** (1977) 2113–2126.

[Wen1936] R. Wenzel, *Resistance of solid surfaces to wetting by water*, Industrial & Engineering Chemistry **28** (1936) 988–994.

[Wen1990] W. Wenig, H. W. Fiedel, and A. Scholl, *Crystallization Kinetics of Isotactic Polypropylene Blended with Atactic Polystyrene*, Colloid and Polymer Science **268** (1990) 528–535.

[Wil1955] M. L. Williams, R. F. Landel, and J. D. Ferry, *The Temperature Dependence of Relaxation Mechanisms in Amorphous Polymers and Other Glass-forming Liquids*, Journal of the American Chemical Society **77** (1955) 3701–3707.

[Wyp2016] G. Wypych, Handbook of polymers, 2016, pp. ii–569.

[Xue2009] L. Xue and Y. Han, *Autophobic Dewetting of a Poly(methyl methacrylate) Thin Film on a Silicon Wafer Treated in Good Solvent Vapor*, Langmuir **25** (2009) 5135–5140.

[Yam2006] H. Yamamoto, T. Watanabe, K. Nishiyama, K. Tatsumura, and I. Ohdomari, *Structural investigation of organosilane self-assembled monolayers by atomic scale simulation*, Journal de Physique IV (Proceedings) **132** (2006) 189–193.

[Yam2008] H. Yamamoto, T. Watanabe, and I. Ohdomari, *A molecular simulation study of an organosilane self-assembled monolayer/SiO2 substrate interface*, The Journal of Chemical Physics **128** (2008) 164710.

[Ybe2007] C. Ybert, C. Barentin, C. Cottin-Bizonne, P. Joseph, and L. Bocquet, *Achieving large slip with superhydrophobic surfaces: Scaling laws for generic geometries*, Physics of Fluids **19** (2007) 123601.

[You1805] T. Young, *JSTOR: Philosophical Transactions of the Royal Society of London, Vol. 95 (1805), pp. 65-87*, Philosophical Transactions of the Royal Society A: Mathematical, Physical and Engineering Sciences **95** (1805) 65–87.

[Zha1995] Y. Zhan, L. Xing, and W. L. Mattice, *Simulations of Self-Assembled Monolayers with the Same Surface Density but Different Grafting Patterns*, Langmuir **11** (1995) 2103–2108.

[Zha2001] L. Zhang, K. Wesley, and S. Jiang, *Molecular Simulation Study of Alkyl Monolayers on Si(111)*, Langmuir **17** (2001) 6275–6281.

[Zha2011] D. Zhao, Y. Jin, M. Wang, and M. Song, *Experimental study and molecular dynamics simulation of wall slip in a micro-extrusion flowing process*, Proceedings of the Institution of Mechanical Engineers Part C-Journal of Mechanical Engineering Science **225** (2011) 1175–1190.

[Zhu1987] L. T. Zhuravlev, *Concentration of hydroxyl groups on the surface of amorphous silicas*, Langmuir **3** (1987) 316–318.

[Zhu2002] Y. Zhu and S. Granick, *Limits of the hydrodynamic no-slip boundary condition*, Physical Review Letters **88** (2002) 106102.

[Zim1956] B. H. Zimm, *Dynamics of Polymer Molecules in Dilute Solution: Viscoelasticity, Flow Birefringence and Dielectric Loss*, Journal of Chemical Physics **24** (1956) 269–278.

Danke ...

... möchte ich abschließend sehr vielen Menschen sagen, die diese Arbeit und den damit verbundenen Abschnitt meines Lebens möglich gemacht, mich unterstützt und begleitet haben.

Mein ganz besonderer Dank gilt Prof. Dr. Karin Jacobs, die mir die Möglichkeit geboten hat, in ihrer Gruppe zu promovieren. Dabei hat sie stets großes Vertrauen in mich gesetzt, auch dann, wenn ich selbst dazu zu zögerlich war. Ich möchte mich für die außergewöhnlich engagierte Betreuung und der damit einhergehenden Arbeitsweise und dem Arbeitsklima in der Gruppe bedanken.

Ein großes Danke an Prof. Dr. Martin Müser für die Übernahme einer der Begutachtungen.

Im Laufe meiner Promotion konnte ich mit vielen Kooperationspartnern zusammenarbeiten. So möchte ich mich bei Dr. Michael Paulus und Dr. Christian Sternemann, aus der Gruppe von Prof. Dr. Metin Tolan der TU Dortmund, für die Zusammenarbeit bei Messwochen an DELTA bedanken und in der Folge beim Datenauswerten und Nachmessen von Proben. Für die Zusammenarbeit bei den WLI-Messungen möchte ich Dr.-Ing. Michael Hans, vom Lehrstuhl für Funktionswerkstoffe, Materialwissenschaft und Werkstofftechnik bei Prof. Dr. Frank Mücklich, danken. Vielen Dank an Blandine Boßmann, vom Arbeitskreis Prof. Dr. Wenz, für die GPC-Messungen. Dankbar bin ich für die Kooperation mit Dr. Juan Manuel Castillo Sánchez, vom Lehrstuhl für Thermodynamik der TU Kaiserslautern, der die Simulationen der Substrate umgesetzt hat.

Ein großer Teil dieser Arbeit entstammt der Zusammenarbeit mit Dr. Laurent Joly, vom Institut Lumière der Universität Lyon. Obwohl die Kooperation erst im Laufe des letzten Jahres entstanden ist, war es uns möglich, ein System von Simulationen aufzusetzen, die die Experimente dieser Arbeit nachahmen. Wir konnten erste vielversprechende Daten sammeln und stehen wahrscheinlich erst am Anfang des Weges. Ich möchte mich Bedanken für seine große Geduld, einem Experimentalphysiker MD-Simulationen verständlich zu machen, und dafür, dass dieser Kontakt genau im richtigen Moment zustande kam.

Das außergewöhnliche Arbeitsklima der AG Jacobs wird getragen durch die Mitglieder, aktive wie ehemalige. Ich möchte Dr. Joshua McGraw danken, der als Post-Doc neue Impulse setzte, speziell für die vielen Gedanken, Anregungen, Diskussion und Erklärungen und dafür, dass wir immer noch in Kontakt sind. Dr. Matthias Lessel und Dr. Hendrik Hähl haben mich von Beginn meiner Diplomarbeit begleitet, mir stets bei den großen und kleinen, wissenschaftlichen und nicht so wissenschaftlichen Schwierigkeiten geholfen

und sind mir dabei zum Freund geworden. Dr. Oliver Bäumchen möchte ich Danke sagen für das stets offene Ohr, wenn wissenschaftlich 'Not am Mann' war, auch lange nachdem er die Gruppe verlassen hatte.

Ich möchte mich bei allen bedanken deren Bachelor-, Master- oder Staatsexamensarbeit ich betreuen durfte und deren Ergebnisse auch in diese Arbeit einflossen: Sebastian Backes, Nadine Ackermann, Kirstin Kochems und Sascha Thieltges. Es ist nicht selbstverständlich solche angenehme Betreuungsverhältnisse zu haben.

Vielen Dank an Dr. Nicolas Thewes, der parallel zu mir den Weg der Promotion gegangen ist und dabei vom ersten Tag Büro und Hotelzimmer mit mir geteilt hat. Danke an Christian Spengler, der als virtueller Banknachbar bei jedem Thema zur Stelle war. Danke für den Zusammenhalt und die Zusammenarbeit in der Gruppe an Thomas Faidt, Samuel Grandthyll, Dr. Frank Müller und Dr. Christian Zeitz. Ein ganz besonderer Dank für die nicht selbstverständlichen administrativen und technischen Dinge an Judith Rech und Monika Schuck.

Die Korrekturleser, Dr. Joshua McGraw, Dr. Laurent Joly und Nadine Ackermann, haben viel Zeit und Arbeit in Sprache und Inhalt dieser Dissertation gesteckt und somit erheblich zum Gelingen beigetragen.

Abschließend möchte mich bei meinen Freunden und meiner Familie bedanken, die nie den Glauben an mich verloren haben und immer mehr Zuversicht hatten, als ich selbst. Besonderen Dank an meine Eltern Anette und Michael, die mir alles ermöglichten und darüber hinaus immer den Rücken freihielten. Nadine, vielen Dank, dass du immer für mich da warst und bist, und mir den 'Graul' nimmst. Danke, dass es euch gibt.

Mischa

Eidesstattliche Erklärung

Hiermit versichere ich an Eides statt, dass ich die vorliegende Arbeit selbstständig und ohne Benutzung anderer als der angegebenen Hilfsmittel angefertigt habe. Die aus anderen Quellen oder indirekt übernommenen Daten und Konzepte sind unter Angabe der Quelle gekennzeichnet. Die Arbeit wurde bisher weder im In- noch im Ausland in gleicher oder ähnlicher Form in einem Verfahren zur Erlangung eines akademischen Grades vorgelegt.

Saarbrücken, den 10.10.2016 Mischa Klos